Ruby under pressure

K. Syassen [a]

[a] Max-Planck-Institut für Festkörperforschung, Stuttgart, Germany

PLEASE SCROLL DOWN FOR ARTICLE

Taylor & Francis
Taylor & Francis Group

Ruby under pressure

K. Syassen*

Max-Planck-Institut für Festkörperforschung, Stuttgart, Germany

The ruby luminescence method is widely used for pressure measurement in the diamond anvil cell and other optically transparent pressure cells. With this application in mind, we briefly review the ground-state physical properties of corundum (α-Al$_2$O$_3$) with some emphasis on its behavior under high pressure, survey the effects of temperature and stress on the R-line luminescence of ruby (Cr-doped corundum), and address the recent efforts towards an improved calibration of the R-line shift under hydrostatic pressures beyond the 50 GPa mark.

Keywords: corundum; ruby; luminescence; high pressure; ruby pressure scale

1. Introduction

Since its birth in 1959 [1,2], the diamond anvil cell (DAC) has had an impressive impact on high-pressure research [3–8]. The now widespread application of the DAC is in part due to the availability of the ruby luminescence method for *in situ* pressure measurement and stress characterization [9–15]. The conceptual and technical simplicity of this optical pressure sensing method continues to attract an increasing number of users to laboratory-based high-pressure research with the DAC, and pressure measurement by a ruby probe is still the most frequently used technique in high-pressure experiments at synchrotron light sources.

There exists a large number of reports on the ruby R-line luminescence with and without applied stress. The main intention of this overview is to provide a condensed guide through observations related to the properties of ruby and its use as a pressure sensor. The manuscript emerged from a collection of notes that were largely tutorial in character. Space limitations impose a somewhat cursory approach. Attempts, however, are made to cover most of the relevant literature or at least provide the access points to detailed studies of specific aspects.

The paper is organized in four parts. Relevant properties of corundum at ambient and high pressure are summarized in Section 2. A general survey of the optical luminescence of ruby and the effects of temperature and stress on the R-line emission is presented in Section 3. The calibration of the R-line shift of ruby under hydrostatic pressure conditions is addressed in Section 4 where the focus is on recently proposed revisions of the ruby pressure scale (RPS) in the megabar pressure range. Afterwords are collected in Section 5.

*Email: k.syassen@fkf.mpg.de

2. Properties of corundum

2.1. *Crystal structure*

Aluminum oxide, Al_2O_3, is generally referred to as alumina. Corundum is the mineralogical name of α-Al_2O_3, the thermodynamically stable modification at ambient conditions. Sapphire is often used synonymously with corundum in its pure single crystal form, but actually refers to weakly doped gem-quality varieties with colours other than red. Ruby is the Cr-containing red variety of corundum.

The crystal structure of α-Al_2O_3 [16] can be described as trigonal or hexagonal. The crystallographic details are given in the caption of Figure 1. The structure can be regarded as a close-packed stacking (sequence ABAB…) of oxygen layers with Al ions occupying two-thirds of the octahedral interstitials between quasi-hexagonal oxygen layers. Although six oxygens form a nearly octahedral group around the central metal ion, each Al ion has three nearest oxygens (1.856 Å) and three more oxygen ions at about 5% larger distance (1.969 Å), such that the honeycomb-like Al layers oriented perpendicular to the c-axis appear buckled. The displacement of Al along the hexagonal c-axis direction reduces the point symmetry to C_{3v}. In addition, when viewed along the c-axis (Figure 1b), the triangular arrangement of oxygen atoms above a metal atom is not exactly tilted by 60° with respect to the corresponding triangle in the lower oxygen layer. The loss of mirror symmetry reduces the actual point symmetry for Al to C_3. The oxygens are 4-fold coordinated by Al and have point symmetry C_2.

When corundum is doped with chromium, the Cr^{3+} ions substitute for the aluminum. In fact, the system $Al_2O_3 - Cr_2O_3$ forms a complete solid solution between the two oxide phases. The Cr^{3+} ion has a slightly larger ionic radius than Al^{3+} (0.064 versus 0.057 nm). Thus, doping of corundum by Cr results in a small expansion of the host lattice. Structure refinements of highly Cr-doped corundum [17,18] show the Cr^{3+} ions to be slightly displaced along the c-axis from the position occupied by the aluminum, but a 3-fold rotational symmetry about the c-axis is retained.

2.2. *Elastic properties and P(V) relation*

The compression behaviour under hydrostatic pressure is characterized by the bulk modulus

$$K(V) = -V \left(\frac{\partial P}{\partial V} \right)_X = -V \left(\frac{\partial^2 E}{\partial V^2} \right)_X \qquad (1)$$
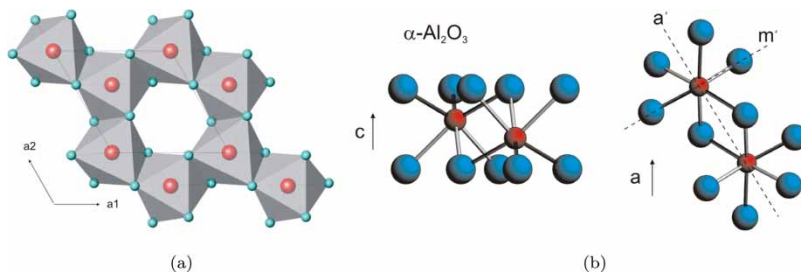
Figure 1. The coordination of the metal ions in the trigonal crystal structure of α-Al_2O_3. The space group is no. 167, D_{3d}^6, or R-3c [rhombohedral cell $a = 5.1285$ Å, $\alpha = 55.2872°$, $Z = 2$, Pearson hR10; hexagonal cell $a = 4.7589$ (10) Å, $c = 12.991$ (5) Å, $c/a = 2.7298$, $V = 254.79$, $Z = 6$, Al in Wyckoff 12c (0, 0, 0.352), O in 18e (0.306, 0, 0.25)]. (a) View of a polyhedral representation down the hexagonal c-axis. (b) View along a direction close to the hexagonal a-axis and along the hexagonal c-axis. The a', m', and c-axes form a suitable orthogonal system for discussions of uniaxial stress effects. The 'vertical' $\underline{m}$ plane which includes the m' direction and the c-axis is not strictly a mirror plane.

and its pressure derivative

$$K'(V) = \left(\frac{\partial K}{\partial P}\right)_X = -\frac{V}{K}\left(\frac{\partial K}{\partial V}\right)_X = -V\frac{(\partial^3 E/\partial V^3)_X}{(\partial^2 E/\partial V^2)_X} - 1. \tag{2}$$

Here E stands for the Helmholtz free energy or internal energy, depending on whether isothermal ($X = T$) or adiabatic ($X = S$) conditions are specified. The dimensionless $K'(V)$ is given by the ratio of third- to second-order derivatives of the energy with respect to volume. In the following, we denote ambient-pressure values by a zero subscript (V_0, K_0, K'_0).

Under hydrostatic pressure, the α-Al$_2$O$_3$ lattice deforms almost isotropically, according to powder [19–22] and single-crystal [23–25] X-ray diffraction experiments. Some of the results indicate a small rate of decrease in the c/a ratio with increasing pressure [20,24].

Ultrasonic measurements of elastic wave propagation [26–34] are the main source of experimental data on the elastic properties of Al$_2$O$_3$ (compilations of data can be found in [35,36]). For the trigonal-I structure of α-Al$_2$O$_2$ there are six independent elastic stiffness coefficients c_{ij}, one more (c_{14}) compared with hexagonal [37,38]. The relation between bulk modulus and elastic stiffness coefficients is

$$K_{\text{trig}} = \frac{c_{33}(c_{11} + c_{12}) - 2c_{13}^2}{c_{11} + c_{12} + 2c_{33} - 4c_{13}}. \tag{3}$$

From elastic stiffness data at 300 K (Table 1), Gieske and Barsch [26] derived an adiabatic value $K_0 = 254.2(3)$ GPa. More recently, Goto et al. [34] determined 253.7 (17) GPa. So, there is a very good agreement between these two measurements on single crystals, the average adiabatic value being $K_0 = 254$ GPa. This value is not affected by a possible uncertainty in the sign of c_{14} [40]. A conversion to isothermal conditions using $K_T = K_S/(1 + \beta\gamma T)$ reduces the value of K_0 by 1.5 GPa (at 296 K the volume thermal expansion coefficient is $\beta \sim 15.54 \cdot 10^{-6}$ K^{-1}, and the thermodynamic Grüneisen parameter is $\gamma = 1.277$ [34]). Thus, the rounded average room-temperature value of the zero-pressure isothermal bulk modulus from the two ultrasonic measurements is

$$K_0 = 253(2)\,\text{GPa} \tag{4}$$

which agrees with the 'best' value recommended by Richet et al. [21]. The error estimate of 2 GPa ($<1\%$) may be a little conservative. The results obtained from other elastic constant measurements (Table 2) lie slightly outside of the estimated uncertainties given above, but larger errors were assigned to those data. Goto et al. [34] have studied the variation of the bulk modulus and other thermodynamic parameters of α-Al$_2$O$_3$ over a wide range of temperature. Anderson's monograph [41] should be consulted for related background on combined temperature and pressure effects on elastic stiffness coefficients.

According to [26], $K'_0 = 4.32$, Reference [26] reports $K'_0 = 4.23$, and from [33] $K'_0 = 4.33/4.37$. Corrections for isothermal conditions are almost negligible. Hence, the average isothermal value at 300 K derived from ultrasonic measurements is taken as

$$K'_0 = 4.30(15). \tag{5}$$

The error attached to K'_0 is that estimated in [26], in which it is classified as conservative.

Table 1. Zero-pressure adiabatic stiffness coefficients c_{ij} (in GPa) and isothermal pressure derivatives ($T = 300$ K) of corundum after Gieske and Barsch [26].

	c_{11}	c_{33}	c_{44}	c_{12}	c_{13}	c_{14}	K_0
c	497.6	501.9	147.2	162.4	117.2	22.9	254.2 (3)
dc/dP	6.17	5.00	2.24	3.28	3.65	0.13	4.32 (15)

Table 2. Bulk modulus (adiabatic) and its pressure derivative for corundum at room temperature as derived from ultrasonic wave propagation experiments.

K_0 (GPa)	K_0'	Sample	First author [reference]
251 (3)		Single	Wachtmann [27]
248		Single	Mayer [28]
251		Single	Bernstein [29]
251	3.99	Poly	Schreiber [30]
			Tefft [31]
	4.23	Poly	Chung [32]
254.2 (3)	4.32(15)	Single	Gieske [26]
$(251)^\dagger$	4.33	Single	Hankey [33]
	4.37	Single	
253.7 (17)		Single	Goto [34]

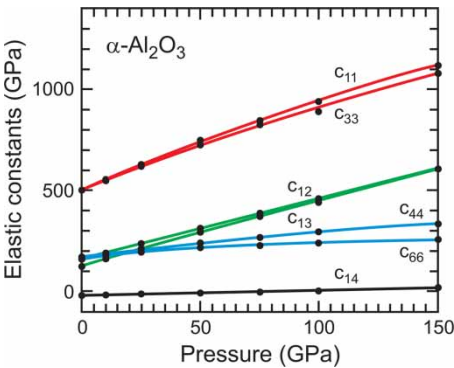$\dagger$Value adopted from [27].

Figure 2. Effect of pressure on the elastic elastic stiffness coefficients of trigonal α-Al$_2$O$_3$ as calculated by Duan et al. [39].

Several *first principles* density functional theory (DFT) calculations of the elastic properties of α-Al$_2$O$_2$ under pressure have been reported [39,42–47]. Figure 2 (redrawn after Duan et al. [39] and being fairly representative of other calculations) demonstrates the calculated effect of pressure (up to 150 GPa) on the elastic stiffness coefficients. The value of c_{14} stays close to zero and the other six constants (as in hexagonal, only five of them are independent because $c_{66} = (c_{11} - c_{12})/2$) come in groups of two. Calculations predict a decrease in the c/a ratio from 2.73 at ambient pressure to 2.685 at 87 GPa [42]. This rather small change of c/a is also reflected in the pressure dependence of the longitudinal moduli c_{11} and c_{33}; the difference between them remains small (Figure 2). More insights into the qualitative interpretation of the elastic stiffness coefficients of α-Al$_2$O$_3$ under pressure may be gained from the comparison to hexagonal crystals as discussed in [26].

Calculated pressure–volume data of Boettger [42] and Caracas and Cohen [43] are shown in Figure 3a. The results demonstrate a common observation in the context of total energy calculations within DFT: there is a quite significant difference in the $P(V)$ behaviour, depending on approximations for the exchange-correlation energy functional and potential (LDA, GGA, or tuned) and – usually to a lesser extent – on the method (all-electron or pseudopotential, choice of basis set(s), etc.). However, after normalization of the pressure and volume variable with respect to the calculated equilibrium values one finds a good consistency (Figure 3b). This is also reflected in the values of K_0' extracted from various DFT calculations: 4.30 (all-electron full potential [42]), 4.06 (pseudopotential, constant pressure variable cell, LDA [35]), 4.14 and 4.20 (pseudopotential
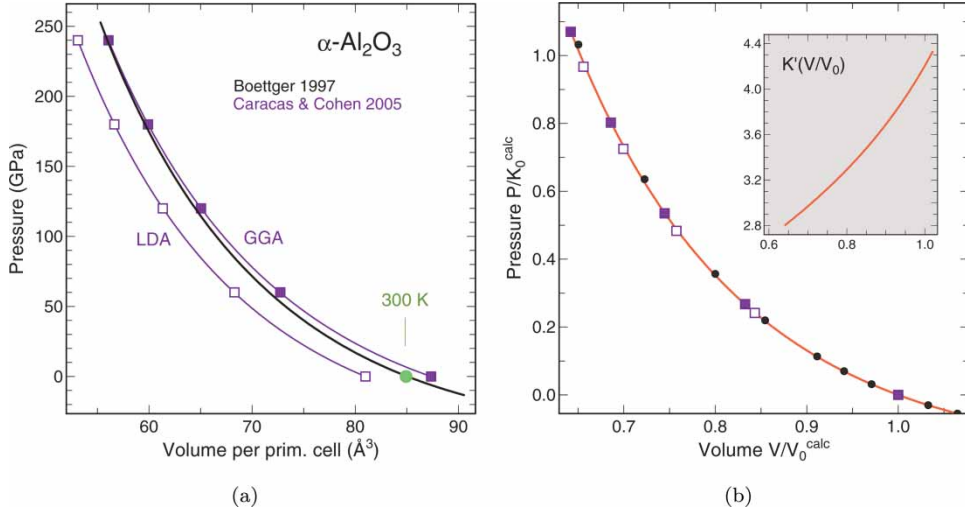
Figure 3. (a) Calculated pressure–volume data for Al_2O_3 after Boettger [42] and Caracas and Cohen [43]. (b) Each set of data in (a) is normalized with respect to the corresponding calculated values of V_0 and K_0. After applying this normalization, the DFT calculations yield almost identical results for the dependence of P/K_0 on V/V_0, nearly independent of approximations for exchange correlation. The inset of (b) indicates the predicted volume dependence of K'.

ABINIT, in LDA and GGA [43]) and 4.23 (pseudopotential ABINIT LDA [46]). The scatter of the calculated values may in part be a result of choosing different analytical expressions when fitting the $E(V)$ or $P(V)$ behaviour. The average value $K'_0 = 4.18(12)$ from DFT calculations for the static-lattice case (*i.e.* not corrected for partly compensating changes of zero-point and thermal pressure at 300 K) is in very good agreement with the 'best' value Equation (5) from acoustic measurements.

In DFT studies [42], it is found that the calculated static-lattice $P(V)$ relation of α-Al_2O_2 is better approximated by a Rydberg–Vinet expression [48] compared with a third-order Birch form [49,50]. In terms of the mean principal stretch or reduced length $x = (V/V_0)^{1/3}$, the Rydberg–Vinet relation is[†]

$$P(x) = 3K_0 \left(\frac{1}{x^2} - \frac{1}{x} \right) \exp\left[k\,(1 - x) \right], \quad k = \frac{3}{2}(K'_0 - 1). \tag{6}$$

The inset of Figure 3b shows the corresponding $K'(V)$ of α-Al_2O_2 which we may consider as the key piece of information provided by the EOS calculations performed within the DFT framework. The Rydberg–Vinet relation of α-Al_2O_3 using $K_0 = 253$ GPa and $K'_0 = 4.3$ is shown in Figure 4.

A Davis–Gordon form [51] of the EOS of α-Al_2O_2 is nearly equivalent to a Rydberg–Vinet form, as can be seen in Figure 4. (In general, the Rydberg–Vinet and Davis–Gordon forms are practically identical if $K'_0 \approx 4.0$ and if a volume change of less than $\sim$40% is considered.) The Davis–Gordon form corresponds to an expansion of pressure in terms of relative change in density $r = \Delta\rho/\rho_0$ with truncation after the second-order term:

$$P(r) = K_0 r \left[1 + \frac{K'_0 - 1}{2}\,r \right], \;\; r = \frac{\rho}{\rho_0} - 1. \tag{7a}$$

[†] The Vinet form is now also called Rydberg–Vinet relation; the analytical form was derived from a Rydberg interatomic potential [52] by Stacey et al. [53], with typos being pointed out in [54]. The limit $K'_0 \to 1$ of Rydberg–Vinet corresponds to a Biot finite-strain EOS (Lagrangian frame) or, equivalently, to the EOS of a monatomic 'harmonic solid' where nearest neighbors interact via a harmonic central force.
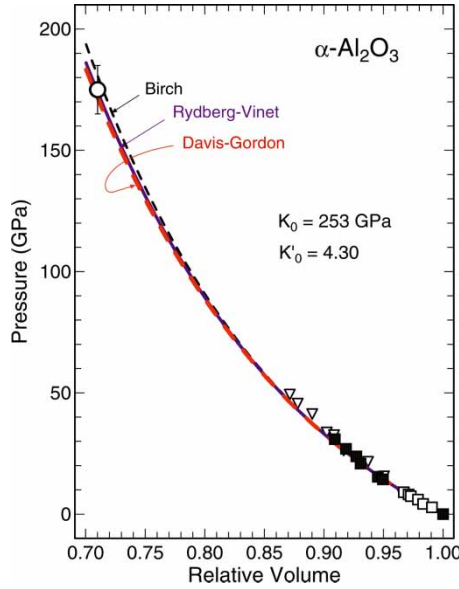
Figure 4. Pressure–volume relation of α-Al_2O_3. The PV curves correspond to Birch (thin dashed lines), Rydberg–Vinet (solid) and Davis–Gordon (thick dashed lines) relations with $K_0 = 253$ GPa and $K_0' = 4.30$ as derived from results of ultrasonic measurements (see text). Data points at low pressure represent results of X-ray diffraction studies [20,21,23–25]. The open circle refers to the data point at the maximum pressure (175 GPa, error > 10 GPa) reached by Jephcoat et al. [22] in synchrotron energy-dispersive diffraction.

Note that $r = (V_0 - V)/V$, *i.e.* the negative volume change is normalized to the volume of the strained state. A useful feature of Equation (7a) is that it is easily inverted, giving

$$r = \frac{1}{K_0' - 1}\left[\sqrt{1 + 2(K_0' - 1)\frac{P}{K_0}} - 1\right].\tag{7b}$$

According to the thermoelastic modeling of Al_2O_3 by Hama and Suito [55], various sets of dynamic compression data, *e.g.* [56,57] and citations in the latter reference, are consistent with the $P(V)$ behaviour shown in Figure 4; however, the reported data do not seem to provide a stringent test of the EOS relation. Also, the shock data may be affected by phase transitions [58].

Of the reported high-pressure X-ray diffraction data [19–25], those limited to maximum pressures of $\sim$10 GPa are consistent with the Rydberg–Vinet-type $P(V)$ relation shown in Figure 4 simply because such data are insensitive to K_0' and to the functional form of the EOS. The $P(V)$ data of Richet et al. [21], measured up to $\sim$50 GPa, show a deviation towards higher pressure which is also reflected in their value of $K_0' = 5.1(4)$. In view of the elastic constant measurements and results from DFT calculations, a value of $K_0' \approx 6$ as given in [25] would be difficult to accept.

Based on the data derived from ultrasonic measurements in combination with the results of *first principles* calculations, we assume that the 'best' values of K_0 and K_0' (Equations (4) and (5)), when inserted into Equation (6) or Equation (7a), provide a reasonably accurate description of the $P(V)$ relation of α-Al_2O_3. In view of discrepancies with some of the X-ray diffraction data, a high-resolution angle-dispersive diffraction experiment under hydrostatic pressure up to, say, 50–100 GPa would be worthwhile.

As for other elastic and thermodynamic properties of α-Al_2O_3, two good starting points, also in the introductory sense, would be [34] and the theoretical work of Catti et al. [59]. In the latter case, the macroscopic properties are modeled on the basis of interatomic pair potentials. Another modeling of thermoelastic properties is by Hama and Suito [55].

2.3. *Vibrational properties*

The rhombohedral (primitive) unit cell of corundum contains two Al_2O_3 formula units. Since the primitive cell has a center of symmetry, all vibrations that are Raman allowed are infrared-forbidden and vice versa. There are five E_g and two A_{1g} Raman-active modes. A short discussion of the Raman scattering of corundum at ambient pressure is presented in [60,61]. Table 3 lists the reported frequencies and the relative intensities observed for different polarizations (in the Porto notation; the full notation is $a(bc)d$ in (x, y, z) coordinates, a = direction of ingoing light, b = direction of polarization of incident light, c = direction of polarization of emitted light, d = direction of outgoing light). Figure 5a shows the corresponding Raman spectra [60]. The maximum phonon frequency in α-Al_2O_3 ($\sim$900 cm^{-1}) corresponds to a temperature of $\sim$1070 K; for comparison, the experimental acoustical Debye temperature is given as $\Theta_D = 1034$ K [34]. The phonon dispersion relations obtained by neutron inelastic scattering may be found in Schober et al. [63]. Figure 5b shows the calculated one-phonon density of states of Heid et al. [64].

Table 3. Raman-mode frequencies (in cm^{-1}) of corundum after [60] and pressure coefficients (in cm^{-1}/GPa) and mode Grüneisen parameters at zero pressure after [62]. Intensities are in relative units as given in [60].

ν	$d\nu/dP$	γ_0	(zz)	(xx)	(xy)	(xz)	Assignment
378	1.335	0.992	Faint	3	4	50	E_g ext.
418	1.703	1.148	>55	>58			A_{1g}
432	2.794	1.731		18	7	17	E_g ext.
451	–	–		Faint	16	Faint	E_g int.
578	2.760	1.283		33	33	21	E_g int.
645	3.481	1.485	>55	Faint			A_{1g} (zz)
751	4.218	1.517		>55	22	Faint	E_g int.
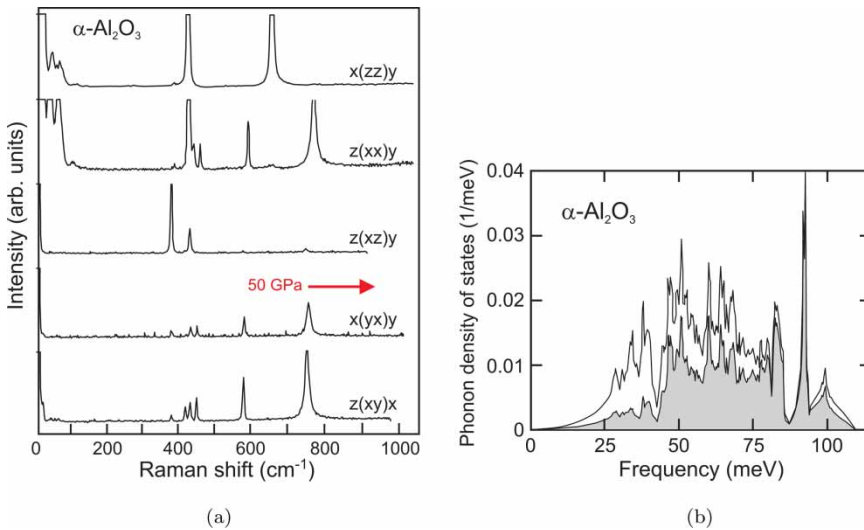
Figure 5. Vibrational properties of corundum. (a) Raman spectra at ambient conditions measured in 90° scattering geometry, reproduced from Porto and Krishnan [60]. The arrow indicates the expected shift of the highest-frequency Raman line at 50 GPa according to the pressure coefficient reported by Xu et al. [62], (Table 3). (b) Calculated one-phonon density of states of α-Al_2O_3 reproduced from Heid et al. [64]. An energy of 100 meV converts to 806.5 cm^{-1}. The shaded area refers to the partial density of states for oxygen.

The dependence of zone-center optical phonon frequencies on pressure up to 20 GPa is reported in [62] (earlier work up to 1 GPa in [61]). The linear pressure coefficients obtained are listed in Table 3. Also listed are the values of the mode Grüneisen parameter γ_0, defined as

$$\gamma_0 = -\left(\frac{\mathrm{d}\ln\omega(V)}{\mathrm{d}\ln V}\right)_0 = \frac{K_0}{\omega_0}\left(\frac{\mathrm{d}\omega}{\mathrm{d}P}\right)_0. \tag{8}$$

The minus sign implies that γ_0 is positive if the frequency change is positive under compression, *i.e.* for negative volume strain $\Delta V/V$.

The dependence of Raman-mode frequencies and line widths of α-Al$_2$O$_3$ on temperature is reported in [65]. For the IR active modes and refractive index dispersion in the IR, see [66] and subsequent publications citing that work.

2.4. *Optical properties*

The 'optical' window of sapphire extends from 6.5 μm (0.2 eV) in the mid-IR to 140 nm (8.8 eV) in the vacuum UV. At these wavelengths a pure 2 mm thick crystal should still have about 10% transmission (Figures 6a and 6b). For the optical absorption of specially processed high-purity sapphire in the visible and UV, see [67] and references therein. The UV absorption and luminescence excitation spectra of sapphire with low Cr content are reported by Loh [68]. The transparency in the UV is affected by defects and doping which tend to reduce the useful transparency range.

The fundamental band gap of sapphire at ambient conditions (8.8 eV) is a direct one; its value is predicted to increase under hydrostatic pressure [42,69]. A crossover from direct to indirect at ∼150 GPa has been predicted. The direct gap is calculated to decrease under uniaxial compression along the *c*-axis [42].

The refractive index of sapphire in the visible spectral range (540 nm) is 1.771 for the ordinary ray (propagation along the *c*-axis) and 1.763 for the extraordinary ray. An analytical expression for the refractive index dispersion covering the range 270 nm to 5.6 μm is given in the AIP handbook [70, Chapter 6.40]. Doping with Cr has an small effect on the refractive index [71]. In accordance with the predicted increase in the fundamental band gap, the refractive index decreases with increasing pressure [72]. The effect of stress on the F-center cathodoluminescence in the UV is discussed in [73] and in references cited therein. Optical properties of sapphire at photon energies above the fundamental gap are addressed in [44,74].

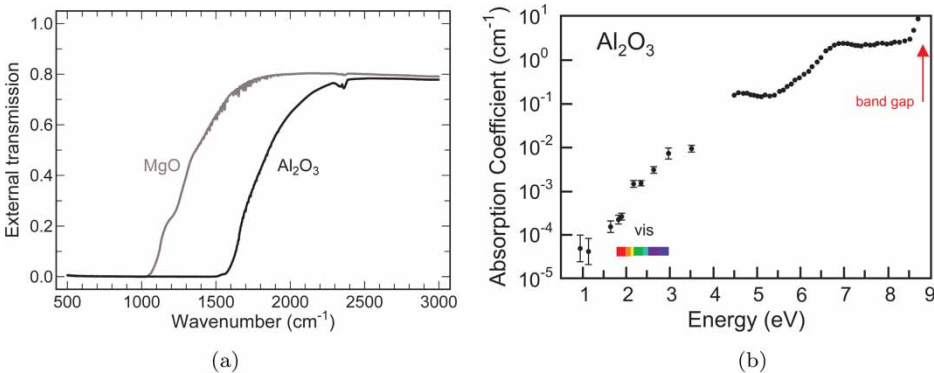Figure 6.   (a) Mid-infrared transmission edge of Al$_2$O$_3$ compared with that of MgO. Data are not corrected for reflection effects. The sample thickness is 2 mm. The edge corresponds to the ceasing of second-order phonon absorption. For moissanite (6H-SiC), see Liu et al. [75]. (b) Absorption coefficient of specially processed high-purity Al$_2$O$_3$ in the visible and UV spectral range, after [67].
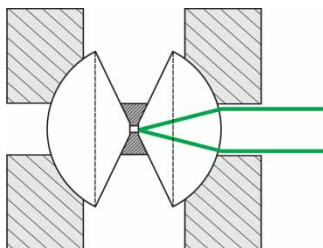
Figure 7. Truncated sapphire balls can serve a double purpose, as anvils and as the equivalent of a 'solid immersion lens' for efficient light collection.

Because of its unique combination of mechanical and optical properties, sapphire is widely used as an optical window in shock wave experiments. Hence, several reports deal with the absorption and emission of sapphire under shock loading in the elastic regime and beyond the Hugoniot elastic limit as determined in [76]. For related works, see, *e.g.* [77,78] and references cited therein. Studies of the refractive index under dynamic compression are reported in [79,80].

The extended UV transparency range (Figure 6b) can be a reason to use sapphire anvils instead of diamond in static high-pressure experiments. Another reason could be that larger samples can be investigated. In this respect, SiC (the moissanite 6H variant) would be a competing window material [75,81], provided that transmission in the deep UV spectral range is not of interest and impurity-induced IR transmission is sufficiently weak. Sapphire can be a useful anvil material in pressure Raman studies of graphitic materials, fullerenes, carbon nanotubes and organic substances, where the frequency region of interest (D mode, etc.) may be masked by the first- or second-order Raman scattering of diamond. The highest pressure that can be reached with pre-stressed sapphire anvils is somewhat limited, 3–5 GPa routinely and about 10–15 GPa in favorable cases [82,83].

Truncated sapphire balls can serve a double purpose, as anvils in a high pressure cell and as focusing optical elements (Figure 7). The setting is similar to a Weierstrass prism configuration [84] or the idea of a 'solid immersion lens'. Other designs of reshaped sapphire balls have been used as anvils [85]. Sapphire plates were used as backing plates for diamond anvils in DACs in order to increase the light collection efficiency in Raman scattering experiments [86].

2.5. *High-pressure modifications*

Near ambient pressure, Al_2O_3 occurs in several metastable crystallographic modifications (spinel-related and other) [87]. We skip over details here. Access points to the literature can be found in several recent reports [44,88–90] on relative phase stabilities. The results of temperature studies at moderate pressures are reported in [91,92].

Phase transitions of α-Al_2O_3 at high pressures were addressed in a number of theoretical studies, [93–98, and work cited therein]. A Rh_2O_3(II)-type phase (Figure 8a) was predicted to follow after α-Al_2O_3 [94–98]. Experimental evidence for a thermally activated phase change at 80–100 GPa to Rh_2O_3(II)-type was reported in [99] and confirmed, including a full structure refinement, in [58]. The original papers discuss why alternative interpretations of the diffraction data are less likely.

Shock wave experiments indicate two high-pressure phase transitions of Al_2O_3, one near 80 GPa [101] and the other near 130 GPa [102,103].

Several perovskite-related post-Rh_2O_3(II) phases were considered in [95,97,98]. In both α-Al_2O_3 and Rh_2O_3(II), the cations occupy a single crystallographic site, but this is not the case in the perovskite-related structures. More recently, a phase change from Rh_2O_3(II)-type to an orthorhombic 'post-perovskite' phase was predicted in [43,46,104]; the structure is described

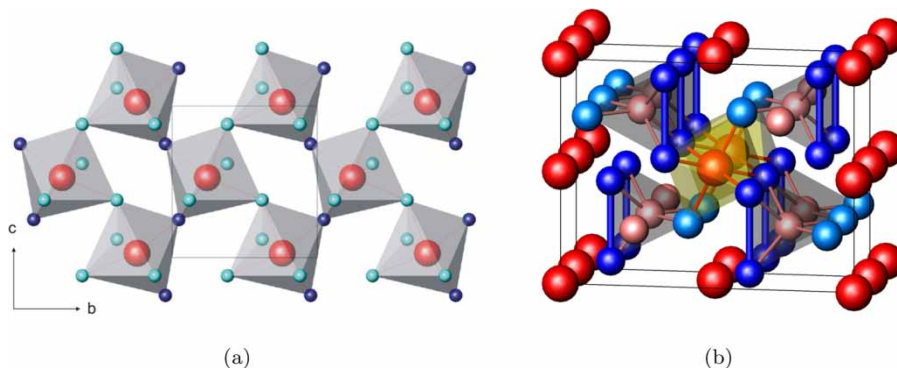(a)   (b)

Figure 8. (a) The orthorhombic Rh_2O_3(II)-type structure (SG 60, Pbna, $Z = 4$, Pearson oP20) of Al_2O_3 viewed along the a-axis. Only a single layer of polyhedra is shown. Structure parameters are taken from Lin et al. [58]. (b) Structure of the $CaIrO_3$-type modification of Al_2O_3 at 150 GPa (SG 63, Cmcm, $Z = 4$, oS20). Calculated atomic parameters as communicated by Oganov were used to generate the figure. Metal ions are located in distorted octahedral and trigonal-prismatic sites. The oxygen ions forming the triangular faces of prisms are weakly 'paired' with a short distance of 2.17 Å. Only very few ABX_3 compounds adopt this structure type at ambient pressure, *e.g.* $AgTaS_3$. The structure has some similarity to that of Pd_3Te_2 [100], but there is an important difference in the 4c positions.

as $CaIrO_3$ type, (Figure 8b). Further, in [46], the $CaIrO_3$-type modification is reported to be observed after thermal activation at ~130 GPa. For a follow-up report on that work, see Ono et al. [105]. Calculated static-lattice enthalpy differences [46] for the α-Al_2O_3, Rh_2O_3(II)-type, and $CaIrO_3$-type phases are shown in Figure 9. Similar calculated results for these and other structure candidates may be found in a number of reports [97,104,106]. For a recent molecular dynamics simulation of the phase stability of Al_2O_3 under pressure, see [107].

The various experimental and theoretical studies of the phase stability at high pressures suggest that α-Al_2O_3 is not the thermodynamically stable room-temperature form at pressures exceeding ~100 GPa (Figure 9). It is not clear whether, at room temperature, at $P > 100$ GPa, and in the presence of shear stress, the α-Al_2O_3 phase tends to transform to a different modification. According to [22], α-Al_2O_3 was observed in X-ray diffraction up to a pressure of 175 GPa. For a related discussion, including chemical stability in a hydrogen pressure medium, see [108] (essentially a response to [109]).

A structural instability of α-Al_2O_3 towards Rh_2O_3(II)-type does not induce a major change in the local coordination count for the metal ions; however, a change in point symmetry ($C_3 \rightarrow C_1$) and a related splitting of metal–oxygen distances are likely to affect the R-line emission of ruby [58,69]. A more pronounced change in emission characteristics would be expected at a transformation to
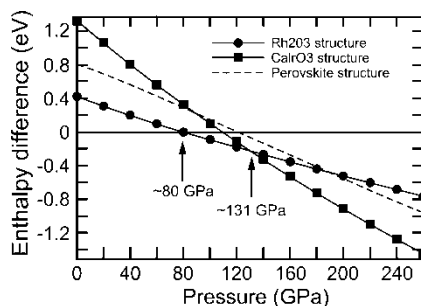

Figure 9. Calculated enthalpy of high-pressure phases of Al_2O_3 relative to the corundum modification, after Oganov et al. [46]. Their results are representative of several other calculations cited in the text.

a CaIrO$_3$-type phase because of changes in local coordination and symmetry; in the CaIrO$_3$-type modification, the metal ions are located in two different six-coordinated sites, octahedral and trigonal-prismatic.

3. Optical luminescence of ruby

3.1. *Energy levels of the Cr ion in ruby*

The optical spectra of Cr-doped corundum (ruby) was studied extensively in the 1950s and early 1960s [110–119] (see [120–123] for earlier work), partly because it is an important model system for the ligand field theory of d^3 systems [124–126] and partly because of the application of ruby in the first solid state laser [127]. The details of the optical absorption and emission spectrum were interpreted in terms of the ligand field theory [110,111,128–130]. The effect of external stress on the optical transitions (also termed *piezo-spectroscopic* effect) was investigated already during the early studies of the crystal field levels of Cr^{3+} in ruby, in order to obtain information on level degeneracy, splitting factors, and the orientation of the luminescence center [117,131,132]. Subsequently, refined optical spectroscopies were used to investigate energy transfer processes between Cr ions and ion pairs, fluorescence line narrowing, and spectral hole burning [133–139].

Figure 10 is a reminder on the basics of localized d-electron levels. An octahedral crystal field removes the 5-fold orbital degeneracy, resulting in three t$_{2g}$ orbitals pointing in between neighboring ions and two e$_g$ orbitals pointing toward the neighbors. The splitting between t$_{2g}$ and e$_g$ levels is usually labeled 10 Dq. The crystal-field ground state of Cr^{3+} has three electrons in t$_{2g}$. With electron–electron interaction taken into account, the ground state becomes a high spin orbital-singlet state (^{4}A$_{2g}$).

A schematic representation of the full-energy-level scheme of Cr^{3+} in ruby is shown in Figure 11. The lowest-energy free-ion multi-electron state of Cr^{3+} is a high-spin state (^{4}F); one of the excited states (^{2}G) is low-spin. The ligand field effects on the free-ion states are dominated by the octahedral crystal field component. The trigonal field in combination with spin–orbit interaction results in additional splittings. The ^{2}E levels are split by $\Delta R_{12} = 29\,\mathrm{cm}^{-1}$; the rather small splitting of the ^{4}A$_2$ ground state by $0.38\,\mathrm{cm}^{-1}$ is not shown in Figure 11.
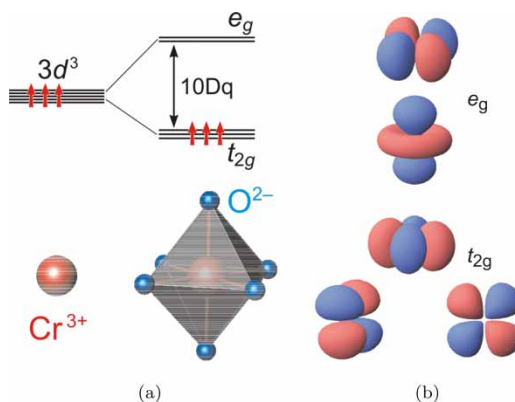
Figure 10.   (a) Level scheme for d-electron orbitals in an octahedral crystal field (strong field limit). The ground state of a d^3 configuration corresponds to the occupation of the three t$_{2g}$ orbitals. Excited states have one or two electrons occupying the e$_g$ orbitals. With electron–electron interaction switched on, the ground state forms a high-spin ^{4}A$_{2g}$ configuration and the spectrum of excited multi-electron states shown in Figure 11 develops. (b) Schematic contours of the t$_{2g}$ and e$_g$ orbitals.
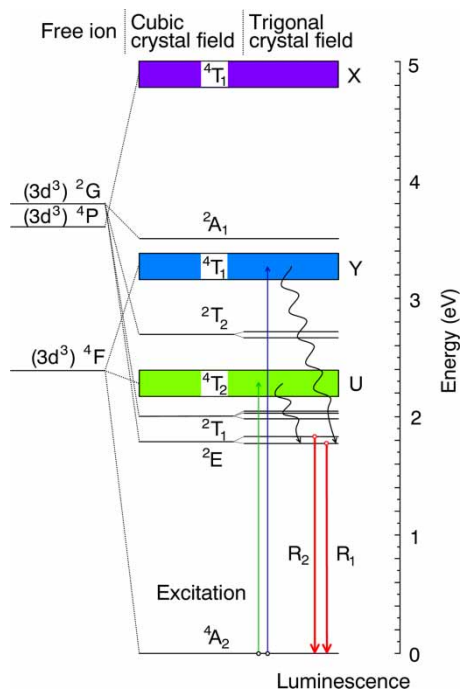
Figure 11. Excited states of Cr^{3+} in ruby (after Tanabe and Sugano). In the weak crystal field limit, one starts from the free-ion multi-electron states. The states split due to the ligand field and interactions between terms. Optical absorption into the $^4T_2$ and $^2T_2$ levels (the U and Y bands) and sharp R-line luminescence originating from the ^2E level are indicated. Note that the energies of the levels shown here are those of the observed optical transition. The final state of an optical transition does not necessarily correspond to fully relaxed spatial coordinates of the corresponding configuration. Thus, in analogy to a Frank–Condon picture, the energy diagram can be expanded as a function of a configuration coordinate [125,126].

Concerning optical transition probabilities, Laporte's parity rule is relaxed due to mixing effects arising from the odd-parity term of the trigonal crystal field, spin–orbit interaction, and configuration mixing. For this reason, the on-site d → d (gerade → gerade) transitions are weakly electric dipole allowed. So, broad spin-allowed U and Y absorption bands corresponding to excitations of the $^4T_2$ and $^2T_2$ levels are centered at about 18,200 and 24,800 cm^{-1}, respectively. These bands cause the pink or red color of ruby crystals (for related discussions see [140] and recent X-ray absorption spectroscopy studies of the relation between mean Cr–O distance and ligand field parameters throughout the solid solution $Al_2O_3 - Cr_2O_3$ [141,142]). At low temperature, the absorption spectra show vibronic structure [143].

Absorption via U and Y bands in combination with phonon-assisted relaxation leads to the population of the excited ^2E low-spin state, as indicated in Figure 11. The related sharp R1 and R2 lines (radiative lifetime ~4 ms at 300 K [144]) are spin-forbidden no-phonon emissions. They are observed near 14,404 and 14,433 cm^{-1} at $T = 300$ K (694.25 and 692.86 nm). For comparison, the experimental value for the energy of the exited $^2G_{7/2}$ free-ion state of Cr^{3+} (from which the ^2E states derive) is 15,056 cm^{-1} [145]. So, placing Cr^{3+} into the crystalline environment of Al_2O_3 reduces the lowest transition energy related to the parent $^4F \rightarrow {}^2G_{7/2}$ free-ion excitation by only about 4%.

We note that the ^2E states can also be populated via direct excitation of the $^2T_1$ levels which are slightly higher in energy compared with ^2E. Under normal conditions (and at least for pressures up to 20 GPa) the $^2T_1$ levels can be excited by the 632.8 nm line of a He-Ne Laser. Laser diode excitation is reported also (see Section 3.3). The lowest level of the $^2T_1$ manifold gives rise to an emission commonly labeled R'_3. X-ray excitation of the R-line luminescence is possible.

The dominant mechanism involves creation of electron–hole pairs in the Al_2O_3 matrix and energy transfer to the Cr^{3+} centers. The X-ray absorption cross-section of Al_2O_3 is rather small. Therefore, the efficiency of the conversion from X-rays to optical emission is much lower compared with that of common X-ray phosphors.

The frequencies of the R-lines show a small increase with Cr concentration [146]. With frequency shift given in wavenumber and concentration c_w in weight percent of Cr_2O_3, the linear relation is $\Delta \nu = 0.99\, c_w$. Since the lattice parameters of ruby also increase with Cr content, there is a volume coefficient of the frequency shift associated with doping $\Delta \nu (cm^{-1}) = 660 \Delta V / V_0$. The value of the volume coefficient is about one-third of that for hydrostatic compression (Section 4.3).

Temperature has a more pronounced effect on the R-line frequencies compared with doping (Section 3.2). It is usually assumed, and has to some extent been demonstrated experimentally at very moderate pressures [147,148], that the effects of doping, temperature, and pressure are independent of each other. So, the frequency shift can be expressed as a superposition

$$\Delta \nu = \Delta \nu(c_w) + \Delta \nu(T) + \Delta \nu(\sigma_{ij}), \qquad (9)$$

where σ_{ij} stands for a general symmetric stress tensor. The temperature effects depend on the phonon spectrum which is a function of applied stress; hence, assuming uncoupled temperature and stress effects is an approximation (see, *e.g.* [149] for related experimental observations).

3.2. *Effect of temperature on R-lines*

Figure 12a illustrates the temperature dependence of the R-line spectra at ambient pressure [150]. With decreasing temperature, the R-lines shift to higher energy, their widths decrease, and the R2/R1 intensity ratio decreases. The classical paper on the interpretation of the temperature effects on R-line emission is by McCumber and Sturge [151] (see also a short historical note [152] and
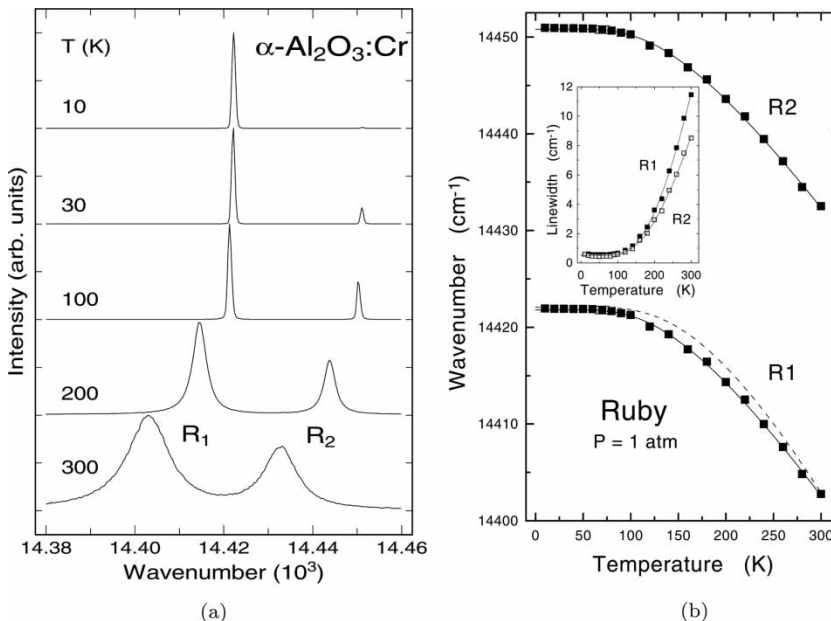
Figure 12. Effect of temperature on R-line luminescence spectra. (a) Spectra of a single crystal of sapphire (not intentionally doped with Cr) at different temperatures. Below $T = 50\,K$, the line width is mainly limited by the spectrometer resolution and residual internal strain. (b) Energies of the R1 and R2 emission lines as a function of temperature. The inset shows the temperature dependence of the corresponding line widths. Data collected by Ulrich [150].

perhaps take a look at 1916 [121] and 1934 [123] papers). A study of highly doped ruby is reported in [153]. In the context of high-pressure research, the investigation of temperature effects were reported in [154–161]. More citations appear in [158].

The change in intensity ratio mainly comes from the relative population of the two ^{2}E levels separated by the energy $\Delta R_{12} = 42$ K and is given by the temperature-dependent Boltzmann factor $\exp(-\Delta R_{12}/k_B T)$. A Boltzmann distribution applies because equilibrium by one-phonon processes is established within the lifetime of the ^{2}E states. One might think of determining the temperature from the relative intensities of the R-lines [162], provided the observed intensity ratio is not affected by other factors, *e.g.* non-isotropic macroscopic stress, polarization, etc. However, due to laser heating, the local temperature may differ from the average one.

Near room temperature, the spectral shape of the R-lines is basically of the Lorentzian type (the R1 line more so than the R2 line), indicating that the width is dominated by homogeneous broadening. For a discussion of the line profile, see [159,163,164]. A practical approach to model the measured R-line spectra is to use pseudo-Voigt or Pearson-VII peak profiles.

Figure 12b shows the frequencies of the R-lines as a function of temperature from 4 K to about 300 K [150]. For small ΔT, the shift $\Delta \nu(T)$ can be written as

$$\Delta \nu(T) = \left[\left(\frac{\partial \nu}{\partial V} \right)_T \left(\frac{\partial V}{\partial T} \right)_P + \left(\frac{\partial \nu}{\partial T} \right)_V \right] \Delta T. \tag{10}$$

The first factor in the square brackets describes the change caused by thermal expansion. Its sign is positive for the R-lines, but quite small (0.03 cm^{-1}/K at 300 K) when compared with the observed negative frequency shifts (-0.14 cm^{-1}/K at 300 K). The second factor is the isochoric (constant volume) temperature shift. Obviously, its sign is negative for the R-lines, as is also the case for energy band gaps of most of the tetrahedral semiconductors. The temperature-induced energy shift of the R-lines is caused by electron–phonon interaction [151]. The shift varies with phonon occupation number and is related to the change of the mean square displacement of atoms with change in temperature.

The shift of the R-lines due to electron–phonon interaction is given by [151]

$$\nu(T) = \nu(0) + \alpha \frac{T}{\Theta} D_3 \left(\frac{T}{\Theta} \right), \tag{11}$$

where α is a measure of the electron–phonon coupling strength, Θ is a temperature characteristic of the relevant part of the phonon spectrum, and

$$D_3 \left(\frac{T}{\Theta} \right) = \left(\frac{T}{\Theta} \right)^3 \int_0^{\Theta/T} \frac{x^3}{\exp(x) - 1} \mathrm{d}x \tag{12}$$

is the 'order-3' Debye function. Polynomial expressions of various degrees have been used to approximate Equation (11) over temperature ranges of interest [158,161]. To model the *low-temperature* regime ($T \lesssim 300$ K), one can apply an analytical relation which captures some of the underlying physics and is frequently used to describe the temperature dependence of semiconductor band gaps [165], *i.e.* excitations involving extended states. The fitted curve through the frequency versus temperature data in Figure 12b is

$$\nu(T) = \nu_0 - \alpha_\nu N \left(\frac{T}{\Theta_\nu} \right) \tag{13}$$

with

$$N \left(\frac{T}{\Theta} \right) = \frac{1}{\exp(\Theta/T) - 1}. \tag{14}$$

The exponential factor $N(T/\Theta)$ has the form of a Bose–Einstein phonon occupation probability for an average phonon energy $\langle \hbar\omega \rangle = k_B\Theta$. Actually, Equation (13) should be written as

$$\nu(T) = \nu_s - \alpha_s \left[1 + 2N\left(\frac{T}{\Theta}\right) \right]$$

where the term in square brackets represents the ensemble-averaged square of the phonon displacement, see [166, p. 329, and literature cited there].

The effective parameters in Equation (13), obtained by fitting the zero-pressure experimental data [150], are listed in Table 4. The zero-temperature wavenumber ν_0 varies slightly (± 1 cm^{-1}) for different samples, depending on the chromium concentration and history of the sample. Both Θ_ν and α_ν depend on pressure. Assuming that the increase in the average phonon frequency is the dominant pressure effect, we expect a weaker temperature dependence of the R-line frequency at high pressure.

Near room temperature, the R-line frequencies shift by about -0.14 cm^{-1}/K. Reported high-precision values are -0.144 and -0.134 cm^{-1}/K for the R1 and R2 lines, respectively, in [167] and -0.140 and -0.137 cm^{-1}/K in [163]. A temperature change of $\Delta T = +5$ K at $T = 300$ K has about the same effect as an increase in hydrostatic pressure by 0.1 GPa (-0.75 cm^{-1}). Therefore, if one aims for very accurate pressure determination by the ruby luminescence method at low pressures, the local temperature needs to be well controlled.

At temperatures higher than $\sim$50 K, the widths Γ (full width at half-maximum FWHM) of the R-lines are largely governed by phonon-assisted processes. The temperature dependence is given by [151]

$$\Gamma(T) = \Gamma_0 + \tilde{\alpha} \left(\frac{T}{\tilde{\Theta}}\right)^7 \int_0^{\tilde{\Theta}/T} \frac{x^6 \exp(x)}{[\exp(x) - 1]^2} \mathrm{d}x. \tag{15}$$

For $T \lesssim 300$ K, this relation can be approximated by

$$\Gamma(T) = \Gamma_0 + \alpha_\Gamma N\left(\frac{\Theta_\Gamma}{T}\right). \tag{16}$$

Corresponding effective parameters are also given in Table 4. At 300 K, the widths of the R-lines are about 11.5 cm^{-1} (R1) and 8.5 cm^{-1} (R2) for samples with low residual stress, (Figure 12b). The line widths depend on the doping level [144,161]. They decrease under hydrostatic stress [164].

Equations (13) and (16) are empirical approximations. For a detailed treatment of the temperature dependence of R-line widths, see [151–159]. Spectral analysis procedures for optical temperature sensing are also discussed in [159].

At temperatures higher than room temperature, the R-line emissions broaden further and their peak intensities decrease, such that it becomes more difficult to measure a luminescence spectrum. For details on the ruby luminescence at high temperatures, see [158] and citations therein. Rekhi et al. [160] discuss the high-temperature effects at moderate pressures up to 15 GPa.

Table 4. Parameters describing the temperature dependence of the R-line luminescence spectra of ruby [Equations (13) and (16)] between 4 and 300 K. The values were obtained by analyzing data of ref. [150]. The small line width (FWHM) at low temperatures is not corrected for spectrometer resolution and inhomogeneous broadening due to strain.

Line	Frequency			Line width		
	ν_0 (cm^{-1})	α_ν (cm^{-1})	Θ_ν (K)	Γ_0 (cm^{-1})	α_Γ (cm^{-1})	Θ_Γ (K)
R1	14421.8 ± 0.4	76.6 ± 6.9	482 ± 20	0.59 ± 0.07	129 ± 17	763 ± 35
R2	14450.8 ± 0.4	72.4 ± 6.5	478 ± 20	0.49 ± 0.07	75 ± 10	697 ± 35

3.3. *Absorption and R-line emission under pressure*

The ruby luminescence method for pressure measurement, originally proposed by Forman et al. [9] in 1972 and since then applied routinely in DAC studies [8], has created a strong interest in exploring and understanding the properties of the Cr impurity under large hydrostatic compression.

Figure 13, reproduced from [69], provides us with an overall picture of the effect of hydrostatic pressure on the Cr^{3+} energy levels in ruby. The large positive frequency shifts of some of the Cr^{3+} levels under pressure are mainly due an increase in the octahedral crystal field strength. In a simple point charge model, the octahedral splitting 10 Dq of a free-ion term scales as d^{-5}, where d is the average metal–ligand distance (in experiments, the exponent is often found to be closer to -4 for compounds containing 3d transition metal ions; this is a consequence of covalent effects.).

The energies of the ^2E states depend on the *difference* in crystal field splittings of two *different* free-ion levels (^4F and ^2G, cf. Figure 11). So, changes in their octahedral crystal field splittings/shifts nearly compensate each other. The net effect of pressure on the ^2E levels is a rather small negative frequency shift of $-7.53\,cm^{-1}$/GPa [12] (see also Figure 14). For comparison, typical values for optical-phonon frequency shifts under pressure are of the same order of magnitude ($\sim$3cm^{-1}/GPa for the first-order Raman mode of diamond, see also Table 3). A pressure of $\sim$100 GPa is required to induce a red shift of the R-lines by 4%, *i.e.* a shift that is equal in magnitude to the difference between the free-ion ^4F–^2G excitation energy and that of Cr^{3+} in α-Al_2O_3 at ambient pressure.

Several physics-oriented aspects of the ruby luminescence and absorption under pressure are covered in a series of reports by Eggert et al. [168–171] (for comments and reply see [172,173]) and by Duclos et al. [6]. For instance, the shift of the U and Y absorption bands to higher energy with increasing pressure, originally reported by Stephens and Drickamer [174], has been investigated and interpreted by Duclos et al. [175]. A consequence of this blue shift (Figure 15) is that the excitation of the R-line luminescence with green laser light becomes rather inefficient at high pressures. An alternative is the R-line excitation via the $^2T_1$ levels (cf. Figures 11 and 13), *i.e.* by using red (diode) laser excitation [176].

A notable effect is that the relatively long *radiative* lifetime of the excited ^2E state increases with pressure, reaching about 20 ms at 60 GPa [170,177,178]. For a theoretical treatment of the effect
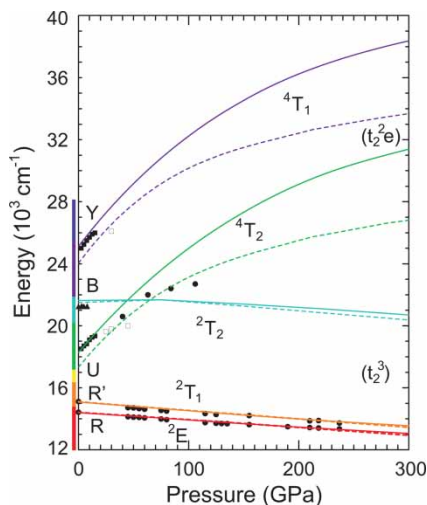

Figure 13. Calculated Cr^{3+} levels in ruby as a function of pressure [69]. Solid lines are for the α-Al_2O_3 phase and dashed lines refer to the Rh_2O_3(II) modification. The symbols represent the experimental data from various sources. Redrawn after [69].
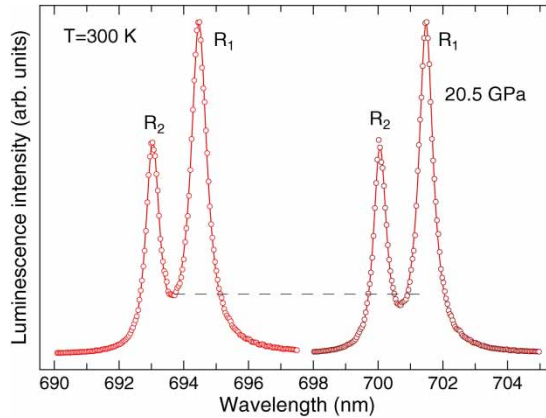
Figure 14.   Normalized ruby R-line spectra at zero pressure and at 20.5 GPa ($T = 300$ K). The total wavelength shift at 20 GPa (~7 nm) amounts to about 12 times the FWHM of the R1 line at 300 K (~0.6 nm). A narrowing of the R-lines with increasing pressure is evident from the decreasing intensity at the minimum between lines. The figure demonstrates a technical aspect: given a typical ruby spectrometer system equipped with a pixel (CCD) detector, a pressure of 20 GPa corresponds to a shift by 100–150 pixels.
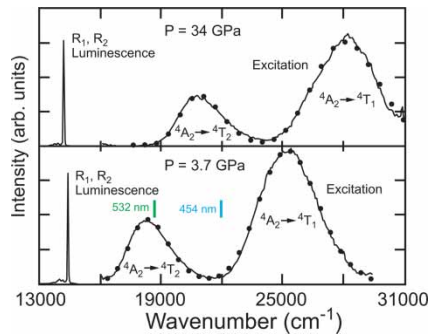

Figure 15.   Optical absorption of ruby at two different pressures [175]. Spectra were measured via luminescence excitation spectroscopy. A typical 'green laser' (a wavelength of 532 nm corresponds to $18,800 \, \text{cm}^{-1}$) matches well the lower-energy absorption band at ambient pressure, but its absorption efficiency decreases with increasing pressure.

of pressure on the lifetime, see also [179,180]. A related experimental study in a garnet is [181]. The long lifetime offers the possibility to discriminate in the time domain (simply by mechanical chopping) between 'slow' R-line emission and Raman scattering or other photoluminescence with shorter lifetime [168,171,182].

The red shift of the R-line energy depends on changes of the ionic potential, wave-function overlap (covalent or delocalization effects), screening, and structural relaxation around the Cr impurity. A theoretical treatment of the crystal field Hamiltonian of Cr^{3+} in ruby as a function of volume or deformation is given in [183–186]. For the calculated results shown in Figure 13, see [69]. A ligand-field-based interpretation of various pressure effects is also offered in several papers by Ma et al. [187–191] and volume/pressure effects were considered in [192].

3.4.   *Effects of static uniaxial stress on R-lines*

Under uniaxial stress parallel or perpendicular to the *c*-axis of a single-crystal ruby, the R1 and R2 lines shift to lower energy [117,131,132,167,193]. An important application of the uniaxial piezo-spectroscopic effects is the non-contact measurement of stresses and strains in polycrystalline

ceramics, oxide surface layers, and corundum fiber composites [194–197]. Static uniaxial stress experiments provide hydrostatic pressure coefficients and play a role in understanding R-line shifts under non-hydrostatic pressure conditions, *i.e.* in the presence of deviatoric stresses.

The frequency shift $\Delta \nu$ as a function of applied stress σ_{ij} can be expanded as [167,194]

$$\Delta \nu = \Pi_{ij}\sigma_{ij} + \Lambda_{ijkl}\sigma_{ij}\sigma_{kl} + \cdots . \tag{17}$$

The purpose of this relation simply is to define coefficients. The Π_{ij} are the linear piezo-spectroscopic coefficients and the σ_{ij} determine the stress state in a suitably chosen orthogonal crystallographic basis of the host lattice (see Appendix). A common reference frame for Cr ions in corundum is defined by the 3-axis along c, the 2-axis parallel to the $\underline{m}$-plane, and the 3-axis along a' (Figure 1b). Clear indications for the importance of higher-order terms in Equation (17) come from the nonlinear dependence of the R-line frequencies on hydrostatic pressure and under shock compression.

Experiments indicate some nonlinear behaviour under uniaxial stress of less than 1 GPa applied along the a'-direction [167] (Figure 16) which has been attributed to a change of symmetry of the oxygen arrangement around a chromium ion. In this context, it is mentioned that the effect of uniaxial stress on the structural relaxation around the Cr ions has been studied by EXAFS combined with modeling [198].

The second rank tensor Π_{ij} is proposed to be symmetric, reflecting the symmetry of the stress tensor σ_{ij} [194]. The form of the tensor Π_{ij} is governed by the point symmetry of the Cr ions in corundum. In the orthogonal crystallographic reference frame, the Π_{ij} tensor is expected to be diagonal, *i.e.*

$$\Pi_{ij} = \begin{bmatrix} \Pi_{11} & 0 & 0 \\ 0 & \Pi_{22} & 0 \\ 0 & 0 & \Pi_{33} \end{bmatrix} . \tag{18}$$

Furthermore, for the *non-deformed* trigonal corundum crystal, the identity $\Pi_{11} = \Pi_{22}$ holds.
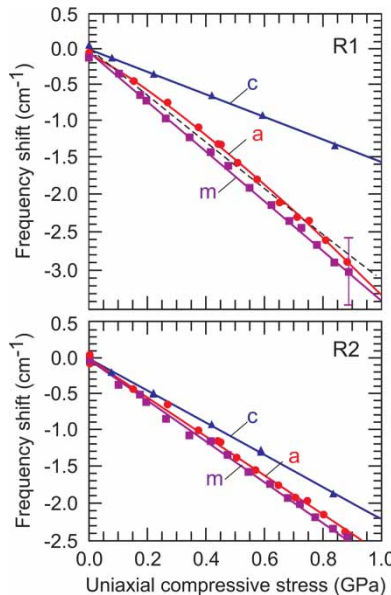

Figure 16.   Frequency shift of the ruby R1 and R2 lines under uniaxial compressive stress after He and Clarke [167]. For the different directions of stress, see Figure 1(b).

Static uniaxial and shear stress effects have been investigated in a systematic manner [167] up to a maximum stress of 0.82 GPa. Some of the experimental results of that work are summarized here.

Shear stress experiments show that the values of the off-diagonal elements of Π_{ij} are indeed less than 10% of the diagonal elements. The *linear* dependence of R-line frequencies on uniaxial stress may be summarized in one expression

$$\Delta\nu_R = \Pi_{11}\,\sigma_{11} + \Pi_{22}\,\sigma_{22} + \Pi_{33}\,\sigma_{33}. \tag{19}$$

The experimental results are (frequency in wavenumber, stress in GPa)

$$\Delta\nu_{R_2} = 2.66\sigma_{11} + 2.80\sigma_{22} + 2.16\sigma_{33}$$
$$\Delta\nu_{R_1} = 2.56\sigma_{11} + 3.50\sigma_{22} + 1.53\sigma_{33}. \tag{20}$$

The original source [167] does not quote error bars for the coefficients. Judging from data points presented in figures, an average statistical error margin of about 3% applies, with systematic errors not specified. It should be noted that the differences between the Π_{ii} coefficients for the R2 line are smaller than those for the R1 line. A consequence is that the frequency of the R2 line will be affected less than that of the R1 line by the presence of uniaxial stress components in a quasi-hydrostatic environment (see also [199,200] for a related discussion of shock compression studies).

The hydrostatic pressure shift following from the set of piezo-spectroscopic coefficients is given by

$$\Delta\nu(P) = -(\Pi_{11} + \Pi_{22} + \Pi_{33})P. \tag{21}$$

One obtains $-7.61\,\mathrm{cm}^{-1}/\mathrm{GPa}$ for R2 and $-7.59\,\mathrm{cm}^{-1}/\mathrm{GPa}$ for R1, close to the hydrostatic shift of $-7.53\,\mathrm{cm}^{-1}/\mathrm{GPa}$ for R1 line reported by Piermarini et al. [12]. For uniaxial compression along the a'-axis, a nonlinear shift of the R1 line was observed (Figure 16), and the corresponding average coefficient Π_{11} for 0.82 GPa applied stress is somewhat larger than the linear coefficient used here. In other words, the absolute hydrostatic-pressure shift derived from the linear frequency shifts of the R1 line under different uniaxial stress conditions may be a lower bound.

For the change of the R-line splitting Δ_{12} under uniaxial static stress, one finds [167]

$$\Delta_{12}(c) = -0.7(1)\,\mathrm{cm}^{-1}/\mathrm{GPa},$$
$$\Delta_{12}(m') = +0.55(10)\,\mathrm{cm}^{-1}/\mathrm{GPa},$$
$$\Delta_{12}(a') = +0.6(1)\,\mathrm{cm}^{-1}/\mathrm{GPa}.$$

Thus, for small uniaxial compressive stress along the c-axis, the splitting decreases, while it increases for stress perpendicular to c. Within error limits, the effect is isotropic in the a', m' plane.

Recently, Margueron and Clake [201] have reported static uniaxial stress effects on the lifetime of the R-lines. The Appendix of that report contains a brief discussion of uniaxial stress effects on the $^2\mathrm{T}_2$ levels.

3.5. *R-lines under dynamic uniaxial loading*

The ruby luminescence was investigated in shock experiments with large uniaxial stress in different directions, but within the elastic limits (range $\sim$10 GPa). The results, related analysis, and implications for the R-line emission under static stress conditions are presented in a series of papers by Gupta and coworkers [185,186,199,202–207]. In general, the observations and conclusions from shock experiments and the results of the static uniaxial stress experiments described
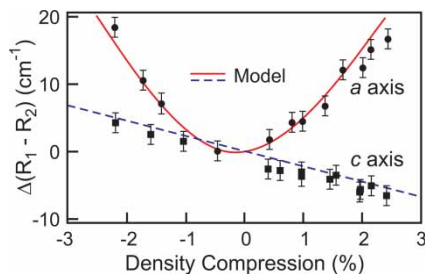
Figure 17. Change of the R1–R2 splitting of ruby R-lines as a function of density change for shocks along the *a*- and *c*-axes. Redrawn after [186].

in Section 3.4 are consistent. In the shock experiments, the magnitude of the change in splitting for strain along the *a*-axis was found to be strongly nonlinear and up to a factor of 4 larger in comparison to the *c*-axis data (Figure 17). The R1-R2-splitting increases for both compression and tension along the *a*-axis, whereas the *c*-axis results vary linearly with compression.

A phenomenological model considering symmetry-adopted strains and based on crystal field theory was developed by Sharma and Gupta [185] in order to analyze and interpret shock wave compression results along the *a*- and *c*-axes. Actually, the model provides a consistent description of R-line shifts under shock deformation, hydrostatic compression, and static uniaxial compression in the limit of small strain values. The analysis of [185] was extended by Shen and Gupta [186] to arbitrary elastic deformations and loading directions.

Early shock wave studies by Goto et al. [208] of the optical absorption of ruby have evidenced a blue shift of the U and Y absorption bands. The R-line emission of ruby has been investigated for shock pressures exceeding the Hugoniot elastic limit by Kobayashi et al. [209].

3.6. *R-lines and deviatoric static stress*

A change of the R1–R2 line splitting observed in a quasi-hydrostatic pressure experiment may be an indication for the presence of deviatoric stress. A demonstration is given in Figure 18 where an observed splitting of $40 \, cm^{-1}$ indicates, based on the linear piezo-spectroscopy coefficients, a substantial deviatoric stress superimposed on an average hydrostatic pressure of about 3.5 GPa.

Chai and Brown [200] have investigated the effect of controlled deviatoric stress on the shifts of the R-lines under confining pressures using a DAC geometry. They state that: (1) the shift of the R2 line is insensitive to deviatoric stress and hence is an indicator of mean stress (as was first suggested in [199]), (2) with ruby loaded along *c*, the line splitting decreases at a rate of $-0.5 \, cm^{-1}$/GPa of deviatoric stress, (3) the splitting increases nonlinearly with deviatoric stress for ruby loaded along *a*, and (4) the results are consistent with the conclusions of Shen and Gupta [186].

Changes of the R1–R2 splitting by $10 \, cm^{-1}$ or more have been reported in static experiments at megabar pressures [211]. A quantitative correlation between this change in splitting and the degree of non-hydrostatic stresses acting on the ruby at these high mean pressures has not been established from static experiments in the megabar range. Estimates have to be based on what is known about the splitting at low pressures.

In the context of deviatoric stress, the yield strength of ruby under pressure is of interest. It has been studied by Maede and Jeanloz [212] for polycrystalline Al_2O_3. The strength is reported to increase from ~4 GPa at ambient to ~5.8 GPa at 70 GPa.

When non-broadened ruby lines are observed at high pressures, it is sometimes concluded that the stress is isotropic. This conclusion is not valid in general because the widths of the ruby lines
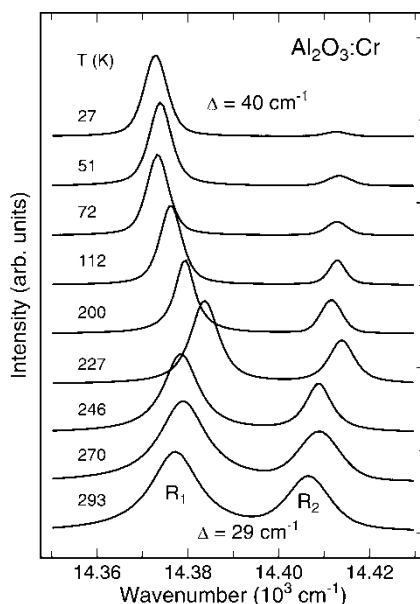
Figure 18.   Luminescence spectra for a ruby crystal measured in a DAC with helium as a pressure medium. At room temperature, where the pressure was about 3.5 GPa, the ruby was compressed isotropically. The thickness of the ruby chip was such that it was about to touch the diamond anvils. Upon cooling, the R-lines first shift to higher frequency as expected from the normal temperature behaviour. At about 220 K, the ruby became squeezed between the diamond anvils due to a slight reduction of their separation. At this point, the R1–R2 splitting starts to increase, reaching a value of 40 cm^{-1} at the lowest temperature. The fact that the lines do not sharpen further at low temperature indicates that the ruby experienced an inhomogeneous stress distribution. Data were collected by Zhou [210].

are related to the degree of *non-uniform* (inhomogeneous) stress across the optically excited part of the sample (stress gradients). Thus, *sharp ruby lines indicate a uniform stress state, but this does not rule out the presence of a substantial deviatoric stress.* Furthermore, unless the crystal orientation with respect to the principal stresses is known, *a constant splitting of R-lines is not necessarily a proof for the absence of deviatoric stress.*

3.7.   *Sidebands of R-lines*

The R-line spectra show vibronic sideband structure (Figure 19). The total width of the vibronic Stokes-shifted emission is similar to that of the one-phonon density of states (Figure 5b). The overall intensity distribution in the phonon sideband emission differs from the one-phonon DOS because the coupling of a localized electronic state to vibrations is selective. Upon cooling, more structure is seen in the vibronic sideband spectrum [122,123]. A detailed experimental study and analysis is reported in [213].

A second contribution to 'sideband' emission consists of the sharp zero-phonon pair-emission lines [112,122,214,215] originating from exchange coupling between chromium ions. Some of the pair emissions can be easily seen at room temperature (Figure 19). Pair-emission lines that are red-shifted relative to the R-line emission originate from leaving behind exchange-coupled Cr pairs in excited configurations; the corresponding energy scale is determined by the magnitude of the relevant exchange coupling constants.

As for the effect of static pressure on the vibronic sidebands of the ruby R-line emission, see [177,216]. The effect of pressure on zero-phonon pair-emission energies was considered by Munro [217]. Pressure effects on the strongest pair lines up to $\sim$10 GPa were reported by
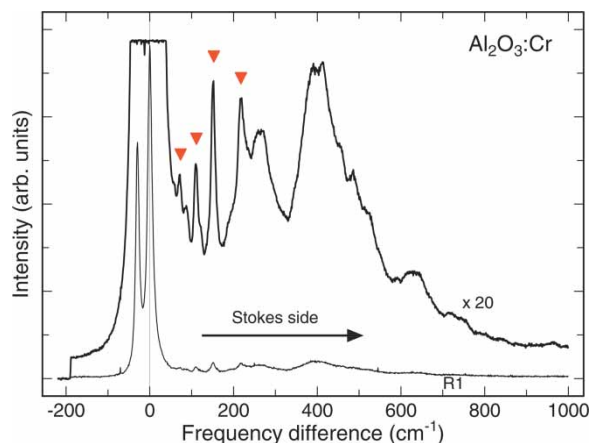
Figure 19. An unpolarized room-temperature luminescence spectrum of ruby (∼1% Cr) covering the Stokes-shifted sideband region. The main contribution to the overall sideband intensity originates from vibrational excitations. Sharp peaks marked by triangles correspond to the zero-phonon emission of exchange-coupled pairs of chromium ions.

Merkle et al. [177] and by Williams and Jeanloz [218]. For early piezo-spectroscopic studies, see [219,220].

The overall intensity and spectral distribution of the sideband emission depends on Cr content. In this context, the optical properties of heavily doped ruby are of interest. They have been reviewed in [221].

4. Ruby pressure scale

4.1. *General comments*

An accurate determination of high static pressure is needed for testing quantitative predictions of material properties by modern theoretical methods. Accurate equations of state are essential for modeling and extrapolations in the geosciences and elsewhere. So, there are important science-related driving forces for establishing an experimental pressure scale that is as accurate as possible.

While accuracy at an absolute level is difficult to obtain, it is important to at least have generally accepted and consistent standards for pressure determination. Furthermore, the methods must be practical in the sense that they can be routinely applied in static pressure experiments. As for the latter criterion, the ruby luminescence method dominates in experimental studies using the DAC and other pressure devices with optical access, at least at temperatures near room temperature and below.

Historically, based on the piezo-spectroscopic effect in ruby, Forman et al. [9] suggested the use of the R-line luminescence to measure pressure in a DAC. Shortly thereafter, Barnett et al. [10] described the optical system they used to perform quantitative micro-spectroscopy measurements on ruby in a DAC, and Piermarini et al. [11] demonstrated hydrostatic limits of various media using the ruby luminescence. These reports served as recipes for many others working or starting to work with DACs.

The RPS denotes the quantitative relation between applied hydrostatic pressure P and wavelength change $\Delta\lambda$ or frequency change $\Delta\nu$ of the R-line emission over a wide pressure range. The linear shift of the R-lines was calibrated by Piermarini et al. [12] for pressures up to ∼20 GPa. At higher pressures, the R-line shift becomes substantially nonlinear in pressure [14,15]. A re-calibration of the *nonlinear* component has been the main concern in recent reports on the RPS.

The RPS comes as a *secondary standard*, at best. In this section, we briefly introduce the principle methods of pressure calibration, consider calibrations of the linear R-line shifts at modest pressures, then turn to some of the used and newly proposed nonlinear calibration relations covering the range up to $P/K_0 \approx 0.6$, comment on how accurate a ruby pressure calibration can be expected to be at this point, and propose an averaged version of the recently proposed revised scales.

4.2. *Calibration methods*

The review by Decker et al. [222] covers the basics of static high pressure calibration in the pre-DAC age. Many of the general thoughts presented therein remain valid.

To calibrate an optical sensor such as ruby, there are three basic routes.

(1) At low pressures, the calibration may be based on direct measurements of pressure using a piston-cylinder-type pressure balance or a gas compressing unit. Static uniaxial stress experiments fall into the same category; they can provide hydrostatic pressure coefficients as discussed in Section 3.4.

(2) A well-established PT phase diagram of a simple substance (simple means elemental or binary compound) can provide 'fixed points' in PT space. A spectral shift of the sensor can be calibrated by passing through the phase boundaries.

(3) The common calibration procedure for the R-line shift in the high pressure regime is to measure the frequency ν_R (wavelength λ_R) of the R-lines and simultaneously, by using X-ray diffraction, the specific volume V_M of a marker compound assumed to be exposed to the same stress conditions as the ruby. The 'known' isothermal equation of state (EOS) of the marker is used for volume to pressure conversion. For calibration at constant temperature, one works within the 'calibration triangle' (Figure 20).

Where does the 'known' EOS come from? Some possibilities (Figure 21) are as follows.

(1) Probing acoustic wave propagation by ultrasonic techniques: One basically follows the approach described in the early literature [223]. The adiabatic bulk modulus K_0 of the marker and its pressure derivative K_0' are derived from acoustic wave velocities measured at low pressures ($P < 1$ GPa) using ultrasonic techniques. For extrapolation to high pressure, the values of K_0 (usually quite accurate) and K_0' are plugged into a semi-empirical $P(V)$ relation. This relation is based on a phenomenological macroscopic description (*e.g.* finite strain equations [50]) or a semi-empirical microscopic model (*e.g.* interatomic potentials) which provide an expression for the dependence of K' on volume V. The incorporation of high-temperature effects in the analysis is addressed in [224]. Recent advances along this route consist of the application of ultrasonic techniques at pressures of the order 10 GPa generated in DACs and large-volume cells and the combination with simultaneous X-ray scattering, [225,226].

(2) Combined Brillouin scattering and X-ray diffraction: The calibration consists of (1) determination of elastic wave velocities under compression using Brillouin scattering by an optically
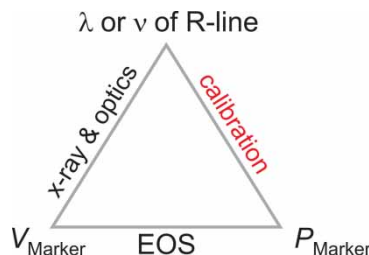

Figure 20. The 'calibration triangle' linking pressure P and specific V of a marker substance M to the ruby R-line frequency (or an optical or Raman excitation frequency of any other optical pressure sensor).
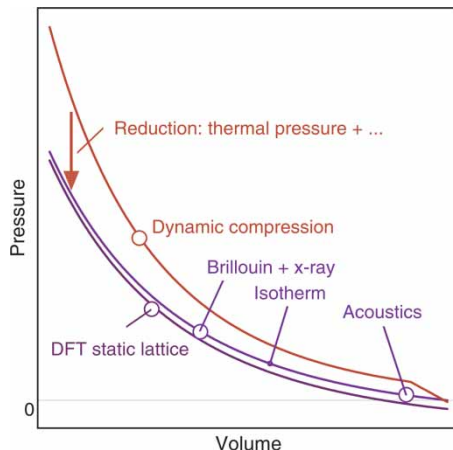
Figure 21.   Schematic: Routes to generate isothermal pressure-volume relationships.

transparent sample of high symmetry (preferably cubic), (2) measurement of the specific volume V by X-ray diffraction, (3) relating sound velocities to volume via the ruby R-line wavelength measured in both experiments, (4) applying elementary transformations to obtain the volume-dependent isothermal bulk modulus $K(V)$ from sound velocities, and (5) integrating the $K(V)$ dependence to obtain the pressure

$$P(V) = -\int_{V_0}^{V} \frac{K(V')}{V'} dV'. \tag{22}$$

This approach is independent of any model assumptions. It has been applied, for instance, to cubic MgO at pressures up to 55 GPa [227]. A recently installed synchrotron-based system for *simultaneous* Brillouin scattering and X-ray diffraction is described by Sinogeikin et al. [228]. A drawback inherent to this approach is that systematic errors in the input data are amplified by the integration.

(3) Dynamic compression: The isothermal PV relation of the marker compound (usually an elemental metal) is derived from dynamic compression. The compression can be along a Hugoniot path or along an isentropic (or quasi-isentropic) path. Dynamic experiments may cover wide pressure ranges (Hugoniot limited to 2-fold increase in density) [229]. A key step in the data analysis is the estimation of the volume- and temperature-dependent isochoric thermal pressure $P^*(V, T)$ which is to be subtracted from the experimental pressure in order to obtain the isothermal compression curve $P(V)$, commonly denoted by the acronym RSWI for 'reduced shock wave isotherm'. The thermal pressure varies between 4% and 20% of the 'cold' pressure at 150 GPa. The reduction of shock wave data to isothermal conditions is briefly described in [229,230], but see also [231–234]. The calculation of thermal effects involves modeling of anharmonicity in the two variables, temperature and volume. A reduction of dynamic compression data within mean field potential theory has received quite some attention [235].

(4) The DFT route: The derivative of the bulk modulus $K'(V)$ is taken from DFT calculations. Combining the calculated $K'(V)$ with experimental values of V_0 and K_0 and *small* corrections due to zero-point motion and finite temperature gives $P(V)$. In brief, the reasons why a DFT-based calibration should work are as follows (more details are presented in [236]): (i) The DFT is said to be 'exact' if the exchange-correlation energy were known exactly [237]. (ii) While calculated (equilibrium) volume, pressure, and bulk modulus of a given substance depend on the approximation for exchange-correlation (LDA, PBE-GGA, or else), all differences nearly

disappear when inspecting the volume-dependent K' (potential anharmonicity) that is obtained from DFT calculations in different approximations. Examples are the results for Al_2O_3 shown in Figure 3b and those for diamond shown in Figure 22. (iii) An (almost) logical consequence of (i) and (ii) is that the calculated $K'(V)$ must be close to 'exact' (pathological substances excluded). (iv) Before accepting this, one better compares with experimental data. The calculated results are generally observed to be in excellent agreement with values of K'_0 obtained from acoustic measurements; here 'excellent' means that differences due to approximations in the theory are smaller than scatter of the experimental data and error bars attached to them. So, the DFT route does not use the $P(V)$ as calculated, but only takes information on the material-specific form of $K'(V)$ including K'_0. Special care is needed when extracting $K'(V)$ from the calculations via a fitting procedure. By testing a bouquet of EOS expressions, *e.g.* Birch, Rydberg–Vinet, Davis–Gordon, and some other empirical EOS forms, one will usually be able to find a simple analytical form which perfectly fits the calculated results for the potential anharmonicity using only K'_0 as an adjustable parameter.

In general, whatever method is applied to determine $P(V)$ of a particular pressure marker, one will check for consistency with other routes to determine the relevant EOS parameters of that marker. In case of discrepancy (sometimes a matter of definition), the accuracy of experimental data needs to be re-assessed and/or any model-related assumptions need to be evaluated critically.

Instead of selecting just one particular substance for calibration via its EOS, it is common to use mixed sets of input data for several different marker materials. These are analyzed by correlated or reverse fitting of the desired ruby calibration parameters. Such techniques have been applied, at different degrees of sophistication, in establishing the original nonlinear calibrations and in most of the recently proposed revisions of the ruby scale. The disadvantage of this kind of *averaging* over multiple-sample data is that the analysis procedure may not look particularly transparent with respect to propagation of errors. On the other hand, the averaging over different sets of input data for different materials has the advantage that any 'outliers' are readily detected, and if
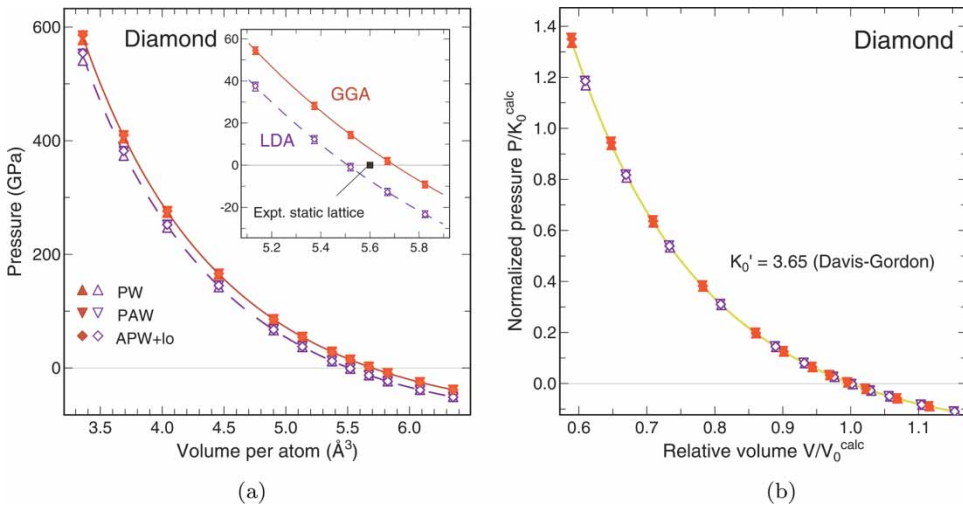
Figure 22. (a): Pressure–volume relations of diamond from DFT calculations [238]. Calculations were performed in LDA and GGA and by using three different methods. (b) Normalized pressure P/K_0 versus normalized volume V/V_0. As in Figure 3b, each set of calculated PV data is normalized with respect to the corresponding calculated equilibrium volume V_0 and bulk modulus K_0. After applying this normalization, one observes that DFT, independent of approximations and computational method, predicts a unique dependence of P/K_0 on V/V_0. In this particular example, the best fit is obtained with the Davis–Gordon form Equation (7a) giving $K'_0 = 3.65(5)$. The error refers to the small scatter for different approximations and methods in the DFT calculations.

systematic errors in individual sets of data are *randomly* distributed over different experiments, they will cancel. Also, the method may help to identify the material which eventually can serve as the reference for a pressure standard.

4.3. *R-lines at modest pressures*

We consider the R-line shift in the pressure regime up to 20 GPa or $P/K_0 < 0.1$ (Figure 14). As usual, zero subscripts refer to ambient pressure or equilibrium volume.

The reported experimental values for the linear pressure coefficients of the R-lines and the conditions of the experiments are listed in Table 5. The 'original' and for a long time accepted value of Piermarini et al. [12] [$(\mathrm{d}\nu/\mathrm{d}P)_0 = -7.53\,\mathrm{cm}^{-1}/\mathrm{GPa}$, $(\mathrm{d}P/\mathrm{d}\lambda)_0 = 0.2746 \pm 0.014\,\mathrm{GPa/Å}$ for the R1 line] appears to have been confirmed by measurements of Nakano et al. [239]. Both experiments covered a pressure range up to ~20 GPa, and Decker's EOS for NaCl [240] served as a reference for pressure determination in both cases. Grasset [163] studied the pressure shift up to 1 GPa using the melting line of water as a reference; he obtained slightly larger (2–3%) absolute pressure coefficients for the energies of the R1 and R2-lines (cf. Table 5).

The linear coefficient of Piermarini et al. (Nakano et al. [239] as well) is averaged over the 0–20 GPa range, *i.e.* it is not the linear coefficient in the zero pressure limit (as pointed out in [241]). Because of nonlinearity (see Section 4.4), the back-extrapolated zero-pressure value of [12,239] should be $(\mathrm{d}\nu/\mathrm{d}P)_0 \sim -7.78\,\mathrm{cm}^{-1}/\mathrm{GPa}$. That value is a little larger than the low-pressure (1 GPa) result for the R1-line of Grasset [163].

The definition of other parameters given in Table 5 is as follows: The pressure coefficient $(\mathrm{d}\nu/\mathrm{d}P)_0$ converts to a volume scaling coefficient (unit is wavenumber)

$$D_0 = -K_0 \left(\frac{\mathrm{d}\nu}{\mathrm{d}P} \right)_0 = V_0 \left(\frac{\mathrm{d}\nu}{\mathrm{d}V} \right)_0. \tag{23}$$

Note that D_0 is positive if the frequency change is negative under compression. An analogy to D_0 is the gap deformation potential in semiconductor physics (the sign convention for D_0 originated there). The value of $D_0 \approx 2000\,\mathrm{cm}^{-1} \approx 0.25\,\mathrm{eV}$ for the R-lines (Table 5) is of course small compared with that of fundamental energy band gaps of semiconductors (silicon 1.4 eV, GaAs −8.2 eV). The linear shift of the R1-line with pressure is commonly characterized by the 'modulus' A_0 (unit is pressure)

$$A_0 = - \left(\frac{\mathrm{d}P}{\mathrm{d}\ln\nu} \right)_0 = \left(\frac{\mathrm{d}P}{\mathrm{d}\ln\lambda} \right)_0. \tag{24}$$

Table 5. Experimental linear pressure coefficients of the R1 and R2-line frequencies of ruby. The corresponding values of the deformation potential D_0 (Equation (23)), calculated with a bulk modulus value of $K_0 = 253\,\mathrm{GPa}$, are also listed. The modulus A_0 is defined in Equation (24). The arrows in the A_0-column point to back-extrapolated values (see text). Marker, pressure range, pressure medium, etc, are given in the column labeled 'conditions'.

Line	$\mathrm{d}\nu/\mathrm{d}P$ $(\mathrm{cm}^{-1}/\mathrm{GPa})$	D_0 (cm^{-1})	A_0 (GPa)	Conditions	First author [reference]
R1	−7.530 (38)	1905	1904 → 1850	NaCl EOS; 20 GPa; ME	Piermarini [12]
R1	−7.548 (12)	1910	1900 → 1850	NaCl EOS; 22 GPa; N_2; 10 K	Nakano [239]
R1	−7.68	1943	1876	H_2O; 1 GPa	Grasset [163]
R2	−7.79	1971	1849		
R1	−7.59	1920	1893	Static uniaxial stress	He [167]
R2	−7.61	1925	1888		

Again, A_0 is positive if the frequency change is negative under compression. The relation between D_0 and A_0 is

$$D_0 A_0 = \nu_0 K_0. \tag{25}$$

For the R1 transition at 300 K, the numerical value of the product is $\nu_0 K_0 = 3.64 \times 10^6$ GPa/cm. The ratio A_0/K_0 is 7.35.

If one takes the value of A_0 as being the average of Piermarini's and Nakano's back-extrapolated values and the other results listed in Table 5 and the average value (1868 GPa) is rounded to three significant digits, one arrives at

$$A_0 = 1870(30) \text{ GPa}. \tag{26}$$

So far, this may be considered the 'best' value in the sense that it originates from measurements on ruby under low-pressure conditions only and that it is largely independent of correlations with higher-order pressure coefficients. It is noted that the error estimate of 1.5% is smaller than the typical errors (3–5%) reported for pressure coefficients of electronic excitations, for instance, semiconductor optical band gaps.

4.4. *Nonlinear calibration relationships*

At high pressures, a substantial nonlinear component of the R-line shift is observed (Figure 23a). As mentioned, the nonlinearity was first determined by Mao et al. in 1978 [14] and then redetermined up to ∼80 GPa in 1986 [15]. The RSWIs of selected metals (Cu, Pd, Mo, Ag) served as pressure references. The calibration of 1986 became known as the quasi-hydrostatic scale; we refer to it by the acronym RPS86. The RPS86 has been confirmed in subsequent work by the same laboratory [211,227]. Moreover, based on the so-called 'primary scale' of Zha et al. [227], the RPS86 was stated to have an accuracy of 1–2% at ∼50 GPa. The RPS86 and its extrapolation into the megabar regime have been widely applied and have served as a practical standard in experimental high-pressure research with the DAC for two decades.

In connection with measurements of the optical zone-center phonon frequency of diamond under pressure up to ∼40 GPa and related first-principle frozen-phonon calculations of the phonon frequency up to 600 GPa, Hanfland et al. [250] pointed out that: (1) the $P(\lambda)$ relation of ruby used at that time [14] underestimated the pressure at a given wavelength and (2) the pressure shift of the diamond phonon could provide a pressure calibration for $P > 50$ GPa (see also [251]). The first point was confirmed shortly thereafter through the re-calibration of the RPS in 1986 [15]. In 1987, Aleksandrov et al. [242] considered diamond as a reference material for ruby pressure calibration, but they focused on the EOS. They proposed an RPS that is based on an experimental determination of the diamond volume V as a function of ruby wavelength λ using combined X-ray diffraction and photoluminescence. A $P(V)$ relation of the Davis–Gordon form Equation (7a) was used for the $V \rightarrow P$ conversion. The calibration of Aleksandrov et al. was considered inconsistent with the RPS86. In retrospect, when comparing with the revised RPSs proposed more recently, the results of Aleksandrov et al. pointed into the 'right' direction.

More recently, the reasons leading to consider a revision of the RPS86 are manifold: larger pressures covered in static experiments, improved control of hydrostaticity by using, *e.g.* helium as a pressure medium in the DAC, advances in analytical experimental methods such as high-resolution X-ray diffraction at synchrotrons, improved analysis of dynamic compression data concerning both shear strength effects and calculation of thermal pressure, and the need to understand discrepancies between *first principles* EOS calculations and experimental $P(V)$ data.

The wave of proposed revisions of the RPS86 apparently started with Holzapfel's proposal of a new calibration relation [241], published in 2003 but widely circulated in mid-2002 already. Holzapfel analyzed the published static compression data and SWRIs of the noble metals [231]
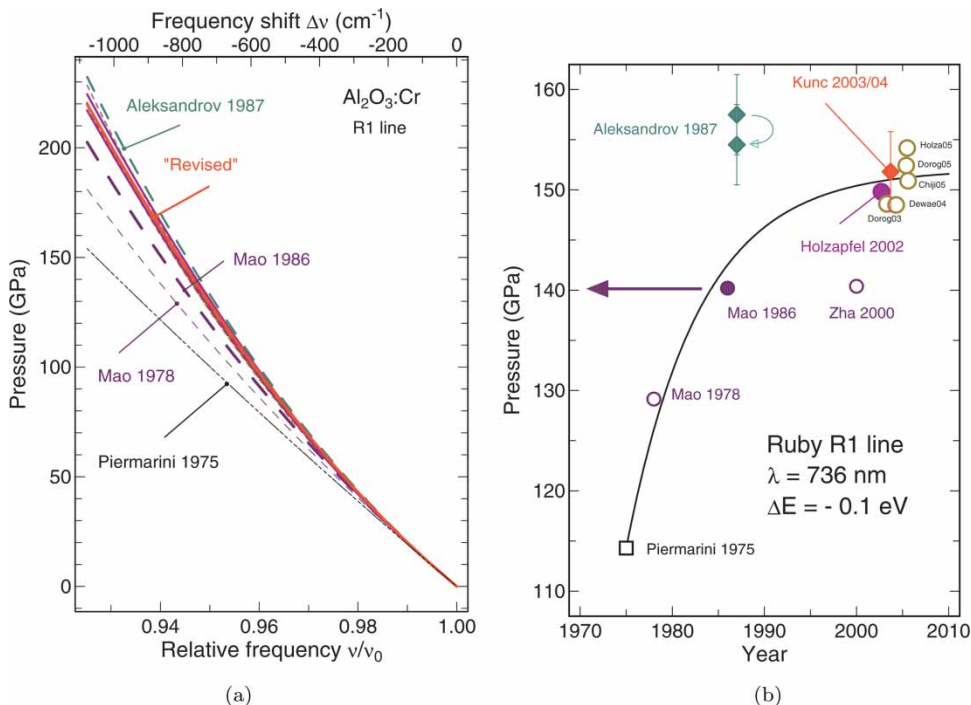
Figure 23.   Ruby pressure calibration history and present state. (a) Pressure P as a function of the relative frequency ν/ν_0 of the R1-line of ruby. The linear relation is an extrapolation of the original calibration by Piermarini et al. [12] for pressures up to 20 GPa. A nonlinear calibration was introduced by Mao et al. in 1978 [14] and updated in 1986 [15]. On the plot scales used here, the relation marked 'Revised' is representative of several revisions discussed in the recent literature (see text). Near 150 GPa, the 'nonlinear component' of the pressure amounts to $\sim$30% of the total pressure. Compare with $P(V)$ in Figure 4 to see that at 150 GPa $\Delta\nu/\nu_0 \approx (1/5)\Delta V/V_0$). (b) How the pressure value assigned to a ruby R1 wavelength of 736 nm corresponding to a redshift of 0.1 eV ($P = 140$ GPa on the 1986 scale) changed with time. Closed symbols [15,241,242] (149.8 GPa), [238,243] (151.8 GPa). Open circles refer to [232] (149.8 GPa), [244] (148.5 GPa), [245] (154.2 GPa), [246] (152.4 GPa), and [247–249] (150.9 GPa). Note that some of the calibration points are extrapolated using expressions that were constrained experimentally at pressures well below 100 GPa. The effect of different extrapolations (i.e. using Equation (27c) or Equation (27d)) is indicated for one of the entries.

and subsequently proposed a revision of the RPS86 [241]. The study had at least three ingredients: (1) the linear pressure coefficient $(d|\nu|/dP)_0$ of the R-line shift was allowed to be $\sim$4% larger ($A_0 \sim$4% smaller) than the value of Piermarini et al. (2) Consistency with the 'primary scale' [227] was required. (3) For selected metals, the static $P(V)$ data measured at $P > 50$ GPa and based on the RPS86 provide a correction by requiring consistency with revised versions of RSWIs; the candidates considered most suitable are materials for which RSWIs are also consistent with (extrapolated) ultrasonic data. Specific examples discussed in [241] are based on high-pressure X-ray diffraction results of tungsten [211], tantalum [253], and other metals. Also, new EOS data for diamond [250,254] were taken into account.

Several reports, including updates, were published addressing the calibration issue and proposing new calibration relations [232,236,243–249,255]. The revision of the RPS86 proposed by Holzapfel in 2002 was basically supported by the analysis of shock data for Cu and Ag by Dorogokupets and Oganov [232] and by comparing EOS and Raman data for diamond obtained by Occelli et al. [250,254] with DFT calculations by Kunc et al. [236,243].

Of prominent importance has been the static pressure experiments on six different metals reported by Dewaele et al. [244] in 2004. Similar to [250,254], X-ray diffraction experiments were performed at the ESRF up to 100–150 GPa in a DAC with helium pressure medium which in

the data analysis was assumed to be hydrostatic. The data of [244] provided new relations between 'X-ray specific volume' V of the metals and the frequency ν of the ruby R-line emission; these have then been used in the follow-up proposals for a new calibration relation. Holzapfel [245] has updated his original revision, this time using input from acoustics and static compression, without resorting to RWSIs in the initial steps of his procedures. On the other hand, the report by Chijioke et al. [246,255] is more heavily based on revised RWSIs. Finally, the analysis by Dorogokupets et al. [247–249,256] considers a large body of available thermodynamic data.

The procedures for generating new calibration relations differ in various respects: use of multiple- or single-marker data, choice of input data, different reduction procedures for shock wave data (if used), and the analytical form used to represent the nonlinear calibration relationship. Although approaches differ, all the recently proposed RPSs arrive at roughly the same correction to be applied to the extrapolated RPS86 at $P \approx 150$ GPa. This is demonstrated in Figure 23b which shows how the pressure assigned to a fixed ruby R1-line wavelength of 736 nm (corresponding to a redshift of 0.1 eV) changed over the years. Values reported after the year 2000 cluster near $\sim$151 GPa which is $\sim$11 GPa higher in pressure compared with the extrapolated RPS86. The spread of the points representing all the new calibrations including revisions is about ± 3 GPa or 2%.

Table 6 lists information on the nonlinear calibration relationships. The related analytical expressions, identified in the first column of this table, are

$$A: \quad P = A_0\epsilon, \quad \epsilon = \frac{1}{B}\left[\left(\frac{\lambda}{\lambda_0}\right)^B - 1\right], \tag{27a}$$

$$B: \quad P = \frac{A_0}{B+C}\left[\exp[(B+C)\eta] - 1\right], \quad \eta = \frac{1}{C}\left[1 - \left(\frac{\nu}{\nu_0}\right)^C\right], \tag{27b}$$

$$C: \quad P = A_0\,\epsilon\,[1 + B_\lambda\,\epsilon], \quad \epsilon = \frac{\lambda}{\lambda_0} - 1, \tag{27c}$$

$$D: \quad P = A_0\,\eta\,[1 + B_\nu\,\eta], \quad \eta = 1 - \frac{\nu}{\nu_0}. \tag{27d}$$

Similar to the definition of strain as a function of principal stretch in isotropic elasticity [257, p. 118], the intermediate variables ϵ or η are used to expand pressure in terms of R-line wavelength

Table 6. The parameters for different *nonlinear* calibrations of the ruby R1 spectral shift under pressure. The coefficients A_0, B, and C refer to the analytical expression identified in the first column and given in the text. If $A_0 = 1904$ GPa, then the original linear pressure coefficient of Piermarini et al. [12] was adopted. Entries are ordered by year. Error bars are those given in the original publication.

Equation	A_0 (GPa)	B	C	Comment	First author [reference]
A (27a)	1904	7.665		Cu, Ag, Ar; 80 GPa	Mao [15]
C (27c)	1892(13)	6.4 (5)		Diamond; He; 70 GPa	Aleksandrov [242]
B (27b)	1820 (30)	14.0 (30)	7.3 (25)	Analysis publ. data	Holzapfel [241]
A (27a)	1871	10.06		Cu, Ag, analysis shocks	Dorogokupets [232]
D (27d)	1860 (30)	7.75 (7)		Dia EOS, phonon, DFT	NDBC [252] + [238,243]
A (27a)	1904	9.5		Six metals; He; 100–150 GPa	Dewaele [244]
B (27b)	1845 (30)	14.7 (17)	7.5 (20)	Analysis publ. data	Holzapfel [245]
A (27a)	1873.4 (67)	10.82 (14)		Various, revised SWRI	Chijioke [246]
C (27c)	1884	5.5		Analysis publ. data	Dorogokupets [247–249]

or frequency/energy, respectively. The general forms are

$$\epsilon = \frac{1}{m}\left[\left(\frac{\lambda}{\lambda_0}\right)^m - 1\right] \quad \text{or} \quad \eta = \frac{1}{n}\left[1 - \left(\frac{\nu}{\nu_0}\right)^n\right]. \tag{28}$$

The coefficients $m, n > 0$ are either taken as a constant integer (*e.g.* $m = 1$ for wavelength shift, $n = 1$ for negative frequency shift) or allowed to be an adjustable real number. Actually, a separate expression for η would not be needed if $m < 0$ is allowed for in Equation (28).

Holzapfel employed the three-parameter form Equation (27b) because it can be viewed as a higher-order expansion of Equation (27a). It has been pointed out, however, that the analytical expression Equation (27b) with the recommended values for its three parameters is representable by the two-parameter form Equation (27d), at least for pressures up to 150 GPa.

Figure 24 shows a difference plot for the recently proposed calibration relations. The new diamond-based calibration of [238,243] (denoted NDBC) is used as reference simply because it happens to reflect the average trend. We observe that the pressures from four out of the six new calibration relations fall into the shaded band of $\pm 1.5\%$ deviation and two more are outside, but only by a small amount and presumably because other (older) EOS data (static in one case, RSWIs in the other) were used in the analysis. At least four of the proposed calibrations are consistent when allowing for a scatter of $\pm 1.5\%$ with respect to the average. In other words, throughout the range up to 150 GPa, the overall agreement must be considered as quite good.

4.5. *Possible systematic errors*

Estimates of error margins of a calibration need to take into account the uncertainties treated by statistical methods and possible systematic errors [258]. As for statistical uncertainties due to randomness (type A uncertainties), one just follows their propagation through all steps of the analysis procedure. The only degree of freedom should be whether to go for just one standard
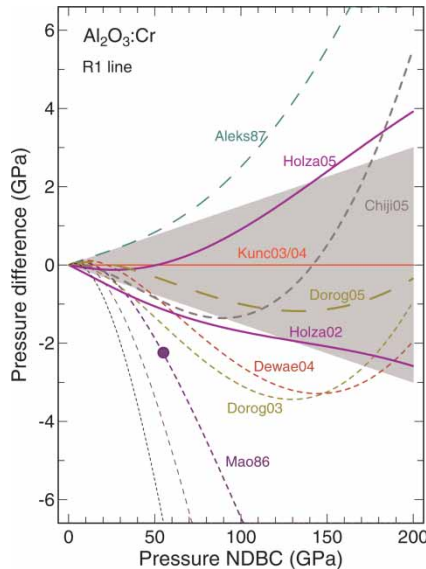

Figure 24. Ruby R-line pressure calibrations compared. Pressure differences relative to the NDBC pressure are plotted as a function of NDBC pressure. All recently proposed calibration relations including revised versions are included. The boundaries of the shaded field mark the region of $\pm 1.5\%$ difference.

deviation or for a more conservative margin representing something like the 'estimated maximum errors'. *Possible* systematic errors (type B uncertainties) in a ruby calibration using a given marker are as follows.

(1) Uncertainty in the isothermal $P(V)$ relation of the marker substance. The pressure derivative $K'(V)$ of the marker is the key property in any pressure calibration based on an EOS. At ambient conditions the values of K'_0 for most elemental solids fall in the range from 3 to 6. Figure 25 illustrates the uncertainty in pressure determination at 150 GPa if the error in the EOS is expressed by $\Delta K'_0 = 0.1$, perhaps a somewhat optimistic number.

(2) Deviatoric stresses due to non-hydrostaticity of the pressure medium lead to errors in the volume measurement as is schematically shown in Figure 26. The effects were first discussed in the 1970s [259–261] with application to aggregates of cubic crystals compressed between opposed anvils and by considering Voigt or Reuss averaging schemes. A detailed analysis of Bragg peak positions in high-pressure X-ray diffraction may aim at estimating the single-crystal elastic parameters of a material at high pressure [262–264] or at obtaining information on the pressure-dependent strength of a material [261,265,266]. An aspect specific to pressure calibration is that one can estimate bounds on the magnitude of the uniaxial stress sustained by a pressure transmitting medium [267–270]. In addition to deviatoric stresses, the diffraction geometry as such can cause errors in the volume measurements. Figure 25 illustrates the uncertainty in pressure at 150 GPa for an error of 0.1% in volume determination by diffraction. That arbitrarily assumed error value is about a factor of 30 larger than the achievable relative precision of a d-value measurement ($\sim 3 \times 10^{-5}$) by synchrotron X-ray diffraction in a DAC.

(3) The measured R-line frequencies can be affected by non-hydrostatic stresses imposed by the pressure medium. Perhaps more important, marker substance and ruby may not be exposed to the same stress field unless the EOS of ruby itself serves as a reference.

(4) There may be errors of systematic character that one could imagine to come into play, but which are not so well understood at present. These are effects related to sample preparation (particle size and shape, purity, degree of filling of the DAC gasket by the sample), work hardening in case of plastic deformation, stress concentration effects, and awkward stress distributions due to the small dimensions of the sample volume in a DAC at very high pressures.
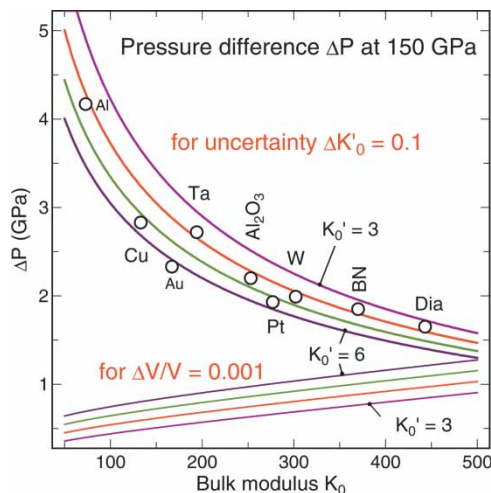
Figure 25.   Difference in pressure plotted as a function of bulk modulus K_0 and with K'_0 as a parameter. The plots are for 150 GPa pressure assuming a Rydberg–Vinet relation. The upper group of lines corresponds to assuming a change of $\Delta K'_0$ by = 0.1. The lower group indicates the pressure difference if an uncertainty of 0.1% is assumed for the volume measurement.
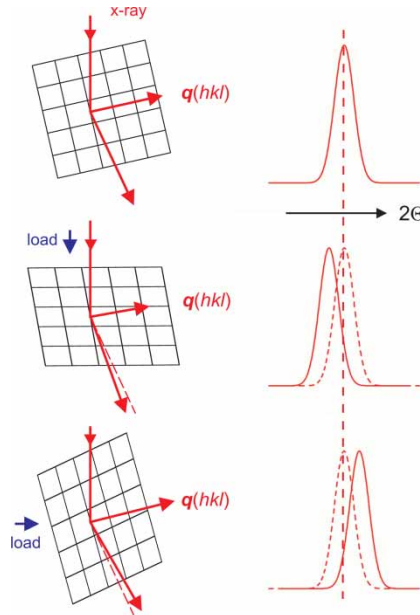
Figure 26.   Diffraction geometry for a set of lattice planes with Miller indices *hkl* under different stress conditions. From top to bottom, the stress states are hydrostatic, uniaxial with load axis nearly perpendicular to the diffraction wave vector **q**(*hkl*), and uniaxial with load nearly parallel to **q**(*hkl*). Uniaxial stress induces a shear deformation as indicated by the angular distortion of the lattice. Bragg reflections are displaced relative to the hydrostatic case. The sign and magnitude of the displacement depend on the relative orientation of diffraction wave vector **q**(*hkl*) and load axis, on the set of Miller indices *hkl*, and on compressive as well as shear elastic constants.

Using helium as a pressure medium in DAC experiments is usually assumed to take care of possible errors caused by deviatoric stresses and stress gradients. At least the consensus now appears to be that helium is to be preferred over other rare gases. However, at around 100 GPa, the melting temperature of helium [271] extrapolates to 1000 K and DFT calculations predict elastic properties of He similar to those of platinum at ambient conditions [272] (see also J. Tse and D. Klug, private communication). Hence, even for dense helium, the effects related to a finite shear strength may not be negligible if the sample-medium composite is kept at room temperature and is not annealed. So, deviations of lattice strains from those under hydrostatic conditions and pressure gradients may cause systematic deviations between 'X-ray volume' and true volume of a marker and therefore shifts in pressure values assigned to a measured R-line wavelength. For a related discussion of the helium pressure medium, see *e.g.* reports by Takemura and Singh [267,269,270] and by Dewaele and Loubeyre [273].

Takemura [270] specifies the hydrostatic limit of helium as being about 50 GPa. It should perhaps be emphasized that Takemura's limit applies to diffraction experiments at room temperature. At low temperatures, optical spectroscopic studies of excitonic transitions in semi-conductors reveal non-hydrostaticity of the helium medium at pressures well below 10 GPa. Further, at 10 K and an average pressure of 20 GPa, a helium medium supports an uniaxial stress of $\sim$0.5 GPa, as can be inferred from the analysis of low-temperature X-ray diffraction experiments [274].

The message of Figure 25 is that the limited accuracy of the reference EOS combined with experimental uncertainties in the specific volume measurement may cause an error in pressure at 150 GPa that can be of the order 3 GPa (2%). The total systematic error of an individual calibration experiment using a given marker may then easily be of the order 5 GPa (>3%) at 150 GPa. Figure 25 also demonstrates that, contrary to intuition, an incompressible material is well suited for calibration purposes, *provided* that its K_0'-value is known with sufficient accuracy.

By averaging over results of independent experiments and different markers, one assumes that systematic errors mostly cancel. The relatively small scatter ($\pm 1.5\%$) between the recently proposed ruby calibration relations supports this view. However, this does not fully rule out a systematic deviation from an 'absolute' calibration of the ruby R-line shift.

4.6. *Averaged version of the proposed revisions*

Let's focus on the three calibration relationships proposed most recently [245–247]. These are based on experimental input data (plus thermal modeling in the case that dynamic compression data are used). It is assumed that the calibration relationship proposed by Dewaele et al. [244] need not be considered separately because the authors tend to agree with the analysis in [247]. Also, calibration relationships in Refs. [248] and [249] seem to be identical to that of Ref. [247].

There appears to be no easy way (meaning non-debatable) to come up with different relative weights for the three recent calibration relations. Even if error bars for related calibration coefficients differ between different reports, it is a little difficult to see whether this may have resulted from different attitudes towards error estimation. Given this situation and the fact that differences between calibration relations are small compared with possible systematic errors of an individual calibration experiment, it should be acceptable to just *average* over the calibration relations proposed in [245–247]. After all, each of the three calibrations itself represents an average, though sophisticated, over different input data.

Different analytical expressions [power-law Equation (27a), polynomial Equation (27c), and exponential-power-law combination Equation (27b) with two (three) adjustable parameters have been used in [245–247] to represent the nonlinear relation between pressure and R-line shift. As a result, the pressure differences in Figure 24 exhibit different degrees of nonlinearity. The differences may be real, *i.e.* supported by the EOS data fed into the analysis procedure, or produced by letting the analysis be attracted towards a particular set of input data or just a consequence of adopting in an *ad hoc* fashion a particular analytical expression, for instance Equation (27a), without testing other expressions. Using the same analytical expression in analyzing different sets of data is highly desirable.

A suitable starting point is a second-order polynomial in relative wavelength or frequency change (Equation (27c) or (27d). Whatever experimental input data are used for testing, it seems not possible at present to tell whether a wavelength or frequency variable is to be preferred in a polynomial expression, because corresponding differences in pressure are smaller than possible systematic errors. Representing pressure as a function of frequency (Equation 27d) may be preferred in a theoretical treatment. On the other hand, from modeling nonlinear behaviour in various contexts, one can construct an argument why one should first turn to writing pressure in terms of inverse frequency, *i.e.* wavelength. An analogous argument is invoked when expanding the strain energy of a solid in inverse principal stretch rather than stretch. So, the expression to start with then is Equation (27c). Figure 27a shows the calibration relationships of [245–247] in the corresponding reduced coordinates, *i.e.* P/ϵ versus ϵ, where a quadratic dependence on wavelength change comes as a straight line.

By combining the calibration relations using equal weights and by least-squares fitting the combined 'data' for pressures up to 150 GPa using Equation (27c) and $A_0 = 1870$ GPa (Equation (26)), one finds $B_\lambda = 5.92$. For A_0 the estimated error is 1.5% (cf. Section 4.3) and that for B_λ should be less than 10%. Hence, it makes no sense to give three digits for the nonlinear coefficient B_λ and the averaged calibration relation is (P in GPa)

$$P = 1870\epsilon \left[1 + 5.9\epsilon\right], \quad \epsilon = \frac{\lambda}{\lambda_0} - 1. \tag{29}$$
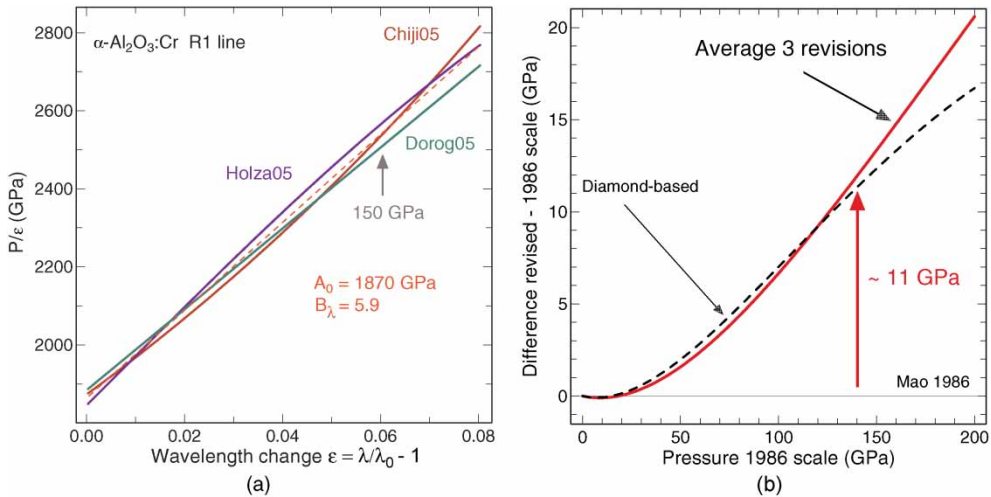
Figure 27. (a) Proposed R-line calibration relations of Holzapfel [245], Chijioke et al. [246], and Dorogokupets and Oganov [247] in linearizing coordinates using the R-line wavelength as the independent variable. The dashed line represents an averaged relation (see text). (b) Difference in pressure between the averaged revised RPS and that of 1986 [15] as a function of the '1986' pressure. The dashed curve refers to Kunc et al. [238,243] who have used an expansion in the frequency of the R-line shift.

For the three calibrations [245–247], the deviations from this average relation are $\lesssim 1.5\%$ in pressure for the range 0–150 GPa. For an estimated uncertainty of ± 30 GPa in the linear coefficient, cf. Equation (26), the variation in the nonlinear coefficient due to parameter correlation is ∓ 0.3.

Figure 27b shows the difference between the pressure calculated with the averaged calibration relation Equation (29) and the RPS86 pressure as a function of the RPS86 pressure. Obviously, the revision of the ruby scale has little effect at pressures below ~ 50 GPa.

Also shown in Figure 27b is the same difference for the single-marker NDBC which is based on a combination of experimental data [252,254] and DFT calculations for diamond [238,243]. The NDBC was represented by the quadratic polynomial in frequency change Equation (27d). It is written as (nonlinear coefficient also rounded to two digits)

$$P = 1860\,\eta\,[1 + 7.7\,\eta]\,, \quad \eta = 1 - \frac{\nu}{\nu_0}. \tag{30}$$

The difference between linear coefficients in Equations (29) and (30) is insignificant. The fact that the nonlinear coefficient in Equation (30) is larger than that in Equation (29) simply comes from choosing a different 'reference frame', *i.e.* different normalization of the R-line shift. Up to 150 GPa, the NDBC agrees with the averaged calibration relation Equation (29) to within 0.5 GPa (cf. Figure 27b). The two relations displayed in Figure 27b start to diverge above the imposed limit of 150 GPa where the NDBC gives a lower pressure. This simply means that expanding the R-line shift in frequency instead of wavelength gives lower pressures when extrapolated beyond 150 GPa.

4.7. *R-line frequency versus volume*

We assume the $P(V)$ relation of ruby to be known [$K_0 = 253$ GPa and $K_0' = 4.30$, Rydberg–Vinet form Equation (6) or Davis–Gordon form Equation (7a)]. With the R1-line shift under pressure according to Equation (30), one obtains the nonlinear volume dependence of the R1-line frequency displayed in Figure 28a.

There seems to exist no *simple* analytical model for the volume dependence of the R-lines (ligand-field theory has scaling parameters). For the volume change ($\cong 200\,\text{GPa}$) spanned in Figure 28a, we consider the exponential form

$$\Delta \nu = \frac{D_0}{\beta} \left[1 - \exp\left(-\beta \frac{\Delta V}{V_0} \right) \right]. \tag{31}$$

The parameter β is just a scaling factor for the independent variable volume. For the curve in Figure 28a, we fit $D_0 = 1959(1)$ and $\beta = 3.042(3)$ (rms deviation $<0.5\,\text{cm}^{-1}$) using $\nu_0 = 14{,}404\,\text{cm}^{-1}$ (R1-line frequency at 300 K). Via Equation (25), the D_0-value converts to $A_0 = 1860\,\text{GPa}$ which is consistent with the 'best' value (see Equation (26)). This consistency and the small rms deviation only mean that the analytical form Equation (31) fits quite well into the system of mutual dependences of the three variables volume, pressure, and revised R-line frequency shift.

An extrapolation of Equation (31) to infinite volume yields an absolute frequency of $15{,}058\,\text{cm}^{-1}$ which happens to agree with the experimental value of the $^2G_{7/2}$ free-ion state of Cr^{3+}, $15{,}056\,\text{cm}^{-1}$ [145]. So, by plugging the known free-ion excitation energy and the zero-pressure energy into Equation (31), the full volume dependence of the R1-line at 300 K can be characterized by a single scaling parameter $\beta \approx 3$. A physics-based argument on why Equation (31) works well needs to be worked out.

There are various ways to obtain linearized relationships in volume: for instance, if the change of the R-line frequency is divided by pressure, one obtains a straight line when plotted versus volume (Figure 28b). The corresponding numerical expression is

$$\frac{\Delta \nu \, (\text{cm}^{-1})}{P(\text{GPa})} = -7.76 - 8.55 \frac{\Delta V}{V_0}. \tag{32}$$

The good description by a linear relation appears to be accidental.

If one had a direct measurement of $\nu(V)$ over a sufficiently large volume range of $\alpha\text{-Al}_2\text{O}_3$ with low Cr doping, one would solve for $V(\nu)$ and insert the volume into the $P(V)$ relation of
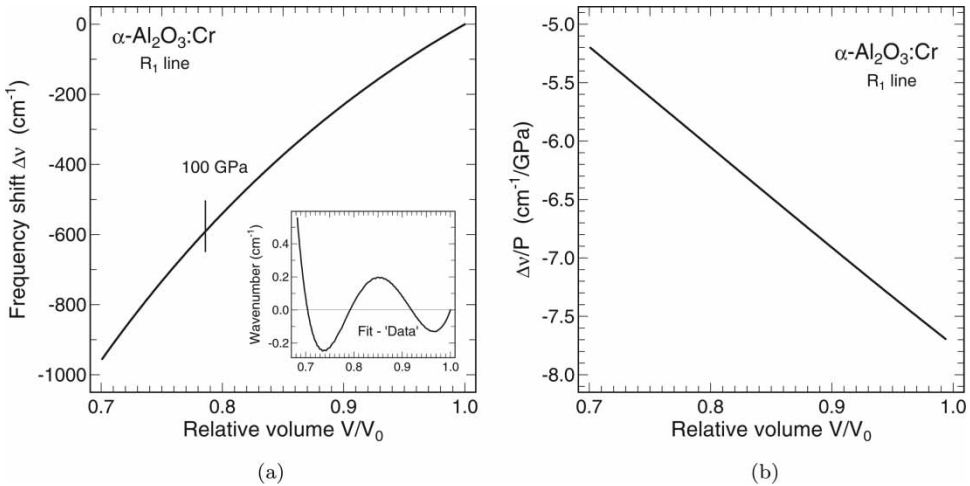
Figure 28. (a) Frequency shift of the ruby R1 line as a function of relative volume. The curve is derived from Equation (30). Pressure is converted to volume using the Rydberg–Vinet-type $P(V)$ relation shown in Figure 4. The inset shows the difference between the fitted Equation (31) and 'data' (see text for parameters). (b): One way to linearize the volume dependence of the R1-line: the frequency shift divided by pressure and plotted as a function of relative volume produces an essentially linear relation.

α-Al_2O_3. Assuming the EOS to be known, the result would be a calibration relation $P(\nu)$ for the R-line frequency based on Al_2O_2 only. At present, the $\nu(V)$ part of the 'calibration triangle' of ruby (Figure 20), is still missing. A precise determination of $\nu(V)$, designed as a single-sample measurement, would be a worthwhile experiment in the context of ruby pressure calibration. At least, the deformation potential D_0 and the modulus A_0 could become constrained within a narrower margin compared with presently available data. A simple estimate of possible errors in a high-accuracy measurement of $\nu(V)$ at modest pressures (say up to 10 GPa) shows that a good resolution and reproducibility in the optical measurement of frequency changes would be crucial; synchrotron-based angle-dispersive diffraction offers the accuracy required for the determination of volume changes.

5. Afterwords

5.1. *Ruby pressure scale*

(1) Within reasonable estimates of possible systematic uncertainties, all newly proposed ruby calibration relations must be considered as being equivalent. It also appears that the revised RPS finds adherents in both the static-pressure and shock-wave communities.

(2) The RPS of 1986 (RPS86) is strongly linked to shock wave data. This still applies to some of the proposed revisions, which are heavily based on EOSs derived from newer shock data and analysis. One observes a tendency to draw more information from data obtained in static experiments. The work of Zha et al. [227] would be an example. The recent analysis by Holzapfel [245] also is mainly based on data obtained under static conditions. Further, one observes that none of those revised calibrations which are based on experiment-derived EOSs challenges a calibration based on DFT-calculated EOS parameters of a weakly anharmonic $[K_0'(V) \approx 4]$ material such as diamond. In general, one can state an overall convergence of different approaches and a large degree of consistency. This is also supported by more recent EOS studies [275]. However, unanimous agreement on the validity of the revision cannot be stated at this point.

(3) For the revised scale, the correction in pressure is $+7\%$ at 140 GPa measured by the RPS86. Thinking in terms of energy, *i.e.* the work of compression, instead of pressure, the revision brings about an increase in $-\int P dV$ which is considerably smaller than 7%; this is because up to 50 GPa, there is not much difference between the RPS86 and the revised scale.

(4) The revised RPS may be affected by non-hydrostaticity in the combined diffraction-spectroscopy experiments that are performed at static pressures of 50–150 GPa. Even for a helium pressure medium, which for a long time was declared to be essentially hydrostatic, the effects related to its finite shear strength are addressed now in experimental studies [267,269,270,273]. Other systematic errors of the revised RPS could possibly arise from the EOS information used to determine pressure. So, despite the good convergence of the proposed revisions, one cannot fully rule out systematic errors.

(5) It appears that further refinements of the RPS in the megabar regime would require better control and understanding of the stress–strain conditions in the DAC sample volume and how they depend on various experimental parameters. This of course applies to other pressure sensors as well. It is not clear whether related experimental studies will mainly satisfy curiosity or could have further implications for EOS studies.

(6) We have avoided comments on the pressure up to which the RPS could be used, not considering the intensity loss of the R-lines under pressure. The pressure limits of the DAC were initially explored on the basis of ruby pressure sensing [276,277], and the technique is applied in more recent explorations [278]. The estimation of mean local pressure values from strongly broadened R-line spectra seen at pressures above 200 GPa may be justified, because the

present evidence is that, even when undergoing phase changes, the chromium ions are likely to remain 6-fold coordinated by oxygen. However, the pressure values should perhaps be taken with a grain of salt.

5.2. *Some consequences of the revision*

(1) The revision of the RPS does not affect much the interpretation of earlier experiments that were performed at pressures up to ∼50 GPa with RPS86 pressures. For instance, only small corrections of at most 2% would be required for pressure coefficients of semiconductor band gaps or vibrational frequencies. Experimental uncertainties (mapped onto the pressure variable) are anyway often larger than 2%.

(2) The revised ruby calibration clearly affects the comparison of experiments and *first principles* EOS calculations. The good news is that static compression data at 50–150 GPa, if based on the new scale, appear to agree much better with isotherms (normalized if necessary), calculated within DFT. For example, adjusted experimental $P(V)$ data of Na [279] (a highly compressible important model system in the physics of nearly-free-electron models) can be shown to almost coincide with the results of *full-potential* total energy calculations. Other examples could serve for demonstration [236]. A comparison of experimental and calculated lattice-dynamical properties may also lead to a better agreement at pressures above 50 GPa.

(3) Evaluations of the merits and shortcomings of common isothermal equations of state expressions (Birch, Rydberg–Vinet, etc.) have been a popular topic in the high-pressure literature [280]. These evaluations are affected by the new ruby calibration (both by the magnitude of the pressure correction and by the degree of nonlinearity), but this is relevant mainly if applied to highly compressible materials at $P > 50$ GPa.

(4) A revision of the RPS has implications for the geosciences and modeling of matter under extreme conditions in other contexts. In general, whenever an extrapolation of pressure-dependent material properties is made, any data based on the revised ruby scale should provide a more solid basis.

5.3. *'Practical' alternatives*

(1) For luminescence-based pressure sensing in high-temperature experiments, substances other than ruby need to be considered. Examples are borates and garnets containing Sm^{2+} or Sm^{3+} as the optically active ion [281–290]. Other candidates have been proposed [291]. It appears that SrB_4O_7:Sm^{2+} is an alternative that largely avoids the limitations of ruby.

(2) Raman-spectroscopy-based pressure sensing is a little more demanding concerning the optical spectroscopy system but one can take advantage of recent technical developments in micro-spectroscopy. In general, an insulating material with relatively small phonon anharmonicity (phonon–phonon interactions) is preferable. The obvious candidates for markers are diamond, cubic BN, and perhaps some light-element oxide of suitable symmetry and stability. Isotopic degrees of freedom in the case of diamond [292] could be helpful. Concerning the calibration of Raman shifts, a comparison to DFT-based predictions may be of some value. For diamond, there is good agreement between measured [242,252] and predicted [238,250,293,294] frequency shifts of the 3-fold degenerate zone-center mode. Cubic boron nitride (apparently first proposed by [295]) is another candidate. It is tested in recent experimental studies [149,296–298] and a phenomenological description is given in [299]. In this context it should be mentioned that c-BN is also advocated as a candidate for establishing a primary pressure scale based on static pressure experiments [298].

(3) An increasing number of DAC experiments is performed at pressures well above 100 GPa. The ruby method poses difficulties in that range because the R-line luminescence intensity becomes weak. Also, the α-Al_2O_3 phase is taken into a metastable regime. Thus, a different laboratory-based optical method for pressure determination is desirable. Raman scattering from the tip region of strained diamond anvils, originally proposed in [306] and occasionally looked at [307], has attracted attention again recently [182,300–305]. It is not clear at this point whether the shift of the diamond tip 'Raman edge' as a function of some kind of average pressure in the sample region as derived from EOS data (Figure 29), could eventually result in a method for pressure determination which is sufficiently robust for practical application at megabar pressures or whether it will remain a fallback method in case the signal from some *in situ* optical pressure marker is lost.

5.4. *Other thoughts*

(1) Most of the proposed revisions of the RPS are based on the thermoelastic properties of several markers (mainly metals). One may ask if a pressure calibration (not necessarily a practical scale) should ultimately be based on the properties of a single reference substance which is well understood. Thinking from scratch, the ideal substance is an insulator with high Θ_{Debye}, small potential and thermal anharmonicity, a high symmetry of the crystal structure, and Raman activity. Chemical inertness towards common pressure media is a prerequisite. A high value of the acoustical Θ_{Debye} is assumed to be equivalent to high hardness, which is considered an advantage in a not perfectly hydrostatic environment. So, one is zooming in (again) on diamond, c-BN, or perhaps corundum. Raman activity is highly desirable because the local stress state can be probed optically in two ways: the frequency shift of a Raman feature can serve as a cross-check on pressure derived from diffraction and Raman spectra can provide information on deviatoric stresses via a
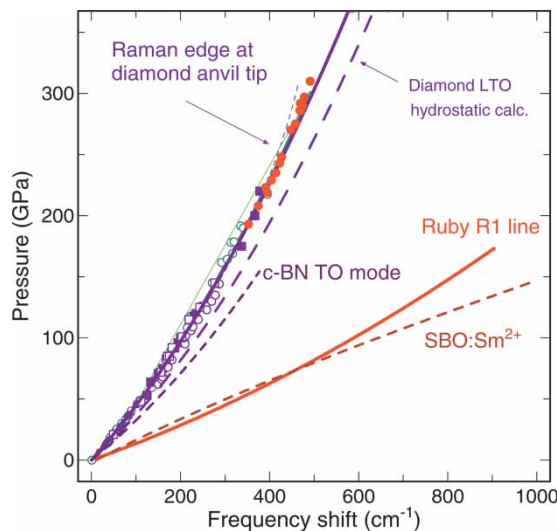

Figure 29. Pressure as a function of frequency shift for different optical sensing methods. Data points for the 'Raman-edge' frequency measured at the tip of diamond anvils under load are taken from [182,300–305]. The solid line drawn through the data is a second-order polynomial in frequency change $\Delta\nu/\nu$ (inserted for $\Delta\rho/\rho_0$ in Equation (7a), fitted parameters are $K_0 = 550$ GPa, $K_0' = 3.65$ for combined data). The associated dashed line refers to the calculated shift of the zone-center Raman mode of diamond under hydrostatic pressure [238]. For a given pressure, the frequency shift of the diamond Raman edge amounts to about one-third of the R-line shift of ruby. Also indicated is the pressure versus frequency shift for the TO Raman mode of cubic BN and the D→F transition of Sm^{2+} in SrB_4O_7 (see text for references).

splitting of degenerate zone-center phonon modes (for diamond in [111] orientation [293,308], in polar c-BN, it is the degenerate TA mode that can split). A combination of static experimental data and DFT-calculated anharmonicity parameters [potential via $K'(V)$, sublattice displacement via optical phonon $\gamma(V)$] of diamond, c-BN, or a similar insulator could be considered in establishing a 'single-sample' reference.

(2) It may sound a bit far fetched, but for calibration experiments at around 100 GPa, sodium may be a candidate for a pressure medium more hydrostatic than helium, as proposed in [279]. It has a very low melting point [309]. Of course, sodium would only be used in experiments that are specifically devoted to establishing a pressure scale for a marker.

(3) Concerning the problem of non-hydrostaticity in solid media, insight may be gained from a simulation of the compression process in a DAC which takes into account the stress-dependent elastic and plastic properties of the four relevant materials (diamond anvils, gasket, pressure medium, and sample) interacting in the tiny space between diamond anvils. Perhaps, this will be possible in the near future.

Acknowledgements

References

[1] C.E. Weir, E.R. Lippincott, A. Van Valkenburg, and E.N. Bunting, *Infrared studies in the* 1 *to* 15 *micron region to* 30 000 *atmospheres*, J. Res. Natl. Bur. Stand. A 63A (1959), p. 55.

[2] J.C. Jamieson, A.W. Lawson, and N.D. Nachtrieb, *New device for obtaining X-ray diffraction patterns from substances exposed to high pressure*, Rev. Sci. Instrum. 30 (1959), p. 1016.

[3] H.-K. Mao, W.A. Bassett, and T. Takahashi, *Effect of pressure on crystal structure and lattice parameters of iron up to* 300 kbar, J. Appl. Phys. 38 (1967), p. 272.

[4] L. Merrill and W.A. Bassett, *Miniature diamond anvil pressure cell for single crystal X-ray diffraction studies*, Rev. Sci. Instrum. 45 (1974), p. 290.

[5] G.J. Piermarini and S. Block, *Ultrahigh pressure diamond-anvil cell and several semiconductor phase transition pressures in relation to the fixed point pressure scale*, Rev. Sci. Instrum. 46 (1975), p. 973.

[6] A. Jayaraman, *Diamond anvil cell and high-pressure physical investigations*, Rev. Mod. Phys. 55 (1983), p. 65.

[7] A. Jayaraman, *Ultrahigh pressures*, Rev. Sci. Instrum. 57 (1986), p. 1013.

[8] M.I. Eremets, *High Pressure Experimental Methods*, Oxford University Press, New York, 1996.

[9] R.A. Forman, G.J. Piermarini, J.D. Barnett, and S. Block, *Pressure measurement made by the utilization of ruby sharp line luminescence*, Science 176 (1972), p. 274.

[10] J.D. Barnett, S. Block, and G.J. Piermarini, *An optical fluorescence system for quantitative pressure measurement in the diamond-anvil cell*, Rev. Sci. Instrum. 44 (1973), p. 1.

[11] G.J. Piermarini, S. Block, and J.D. Barnett, *Hydrostatic limits in liquids and solids to* 100 kbar, J. Appl. Phys. 44 (1973), p. 5377.

[12] G.J. Piermarini, S. Block, J.D. Barnett, and R.A. Forman, *Calibration of the pressure dependence of the* R_1 *ruby fluorescence line to* 195 kbar, J. Appl. Phys. 46 (1975), p. 2774.

[13] H.K. Mao and P.M. Bell, *High-pressure physics: the* 1-*megabar mark on the ruby* R_1 *static pressure scale*, Science 191 (1976), p. 851.

[14] H.K. Mao, P.M. Bell, J.W. Shaner, and D.J. Steinberg, *Specific volume measurements of Cu, Mo, Pd, and Ag and calibration of the ruby* R_1 *fluorescence pressure gauge from* 0.06 *to* 1 Mbar, J. Appl. Phys. 49 (1978), p. 3276.

[15] H.K. Mao, J. Xu, and P.M. Bell, *Calibration of the ruby pressure gauge to* 800 kbar *under quasihydrostatic conditions*, J. Geophys. Res. 91 (1986), p. 4673.

[16] R.E. Newnham and Y.M. de Haan, *Refinement of the* Al_2O_3-*alpha,* Ti_2O_3, V_2O_3 *and* Cr_2O_3 *structures*, Z. Kristallogr. Kristall. Kristallphys. Kristallchem. 117 (1962), p. 235.

[17] S.C. Moss and R.E. Newnhan, *Chromium position in ruby*, Z. Kristallogr. 120 (1964), p. 359.

[18] J.W. McCauley and G.V. Gibbs, *Redetermination of chromium position in ruby*, Z. Kristallogr. 135 (1972), p. 435.

[19] H.V. Hart and H.G. Drickamer, *Effect of high pressure on the lattice parameters of* Al_2O_3, J. Chem. Phys. 43 (1965), p. 2265.

[20] Y. Sato and S. Akimoto, *Hydrostatic compression of four corundum-type compounds: alpha-*Al_2O_3, V_2O_3, Cr_2O_3, *and alpha-*Fe_2O_3, J. Appl. Phys. 50 (1979), p. 5285.

[21] P. Richet, J.A. Xu, and H.K. Mao, *Quasi-hydrostatic compression of ruby to* 500 kbar, Phys. Chem. Miner. 16 (1988), p. 207.

[22] A.P. Jephcoat, R.J. Hemley, and H.K. Mao, *X-ray diffraction of ruby* (Al_2O_3:$Cr3^+$) *to* 175 GPa, Physica B 150 (1988), p. 115.

[23] H. d'Amour, D. Schiferl, W. Denner, H. Schulz, and W.B. Holzapfel, *High-pressure single-crystal structure determinations for ruby up to* 90 kbar *using an automatic diffractometer*, J. Appl. Phys. 49 (1978), p. 4411.

[24] L.W. Finger and R.M. Hazen, *Crystal structure and compression of ruby to* 46 kbar, J. Appl. Phys. 49 (1978), p. 5823.

[25] J. Kim-Zajonz, S. Werner, and H. Schulz, *High pressure single crystal X-ray diffraction study on ruby up to* 32 GPa, Z. Kristallogr. 214 (1999), p. 331.

[26] J.H. Gieske and G.R. Barsch, *Pressure dependence of the elastic constants of single crystalline aluminum oxide*, Phys. Status Solidi 29 (1968), p. 121.

[27] J.B. Wachtman Jr, W.E. Tefft, D.G. Lain Jr, and R.P. Stinchfield, *Elastic constants of synthetic single crystal corundum at room temperature*, J. Res. Natl. Bur. Stand. 64A (1960), p. 213.

[28] W.G. Mayer and E.A. Hiedemann, *Corrected values of the elastic constants of sapphire*, Acta Crystallogr. 14 (1961), p. 323.

[29] B.T. Bernstein, *Elastic constants of synthetic sapphire at* 27°C, J. Appl. Phys. 34 (1963), p. 169.

[30] E. Schreiber and O.L. Anderson, *Pressure derivatives of the sound velocities of polycrystalline alumina*, J. Am. Ceram. Soc. 49 (1966), p. 184.

[31] W. Tefft, *Elastic constants of synthetic single crystal corundum*, J. Res. Natl. Bur. Stand. A, Phys. Chem. A 70 (1966), p. 277.

[32] D.H. Chung and G. Simmons, *Pressure and temperature dependences of the isotropic elastic moduli of polycrystalline alumina*, J. Appl. Phys. 39 (1968), p. 5316.

[33] R.E. Hankey and D.E. Schuele, *Third-order elastic constants of* Al_2O_3, J. Acoust. Soc. Am. 48 (1970), p. 190.

[34] T. Goto, O.L. Anderson, T. Ohno, and S. Yamamoto, *Elastic constants of corundum up to* 1825 K, J. Geophys. Res. 94 (1989), p. 7588.

[35] G. Simmons and H. Wang, *Single Crystal Elastic Constants and Calculated Aggregate Properties: A Handbook*, 2nd edn., MIT, Cambridge, Massachusetts, 1971; H. Wern, *Single Crystal Elastic Constants and Calculated Aggregate Properties: A Handbook*, Reprint, Logos, Berlin, 2004.

[36] F.R.S. Hearmon, *Part I: The elastic constants of crystals and other anisotropic materials; Part II: the third and higher-order elastic constants*, in *Landoldt Börnstein Numerical Data and Functional Relationships in Science and Technology New Series Vol. III/11*, K.H. Hellwege and A.M. Hellwege eds., Springer, Berlin, 1979, pp. 1–276, (See also Vols. 18 and 29 of the same series).

[37] J.P. Nye, *Physical Properties of Crystals*, Oxford University Press, Oxford, 1967.

[38] D.C. Wallace, *Thermodynamics of Crystals*, J. Wiley, New York, 1972, (Republished by Dover, 1997).

[39] W. Duan, B.B. Karki, and R.M. Wentzcovich, *High-pressure elasticity of alumina studied by first principles*, Am. Miner. 84 (1999), p. 1961.

[40] D.B. Hovis, A. Reddy, and A.H. Heuer, *X-ray elastic constants for* α-Al_2O_3, Appl. Phys. Lett. 88 (2006), p. 131910.

[41] O.L. Anderson, *Equations of State of Solids for Geophysicists and Ceramic Science*, Oxford University Press, New York, 1995.

[42] J.C. Boettger, *High-pecision, all-electron, full-potential calculation of the equation of state and elastic constants of corundum*, Phys. Rev. B 55 (1997), p. 750.

[43] R. Caracas and R.E. Cohen, *Prediction of a new phase transition in* Al_2O_3 *at high pressures*, Geophys. Res. Lett. 32 (2005), p. L06303.

[44] B. Holm, R. Ahuja, Y. Yourdshahyan, B. Johansson, and B.I. Lundqvist, *Elastic and optical properties of* α- *and* κ-Al_2O_3, Phys. Rev. B 59 (1999), p. 12777.

[45] M.M. Ossowski, L.L. Boyer, M.J. Mehl, and H.T. Stokes, *Lattice dynamics and elastic properties of corundum by the self-consistent atomic deformation method*, Phys. Rev. B 66 (2002), p. 224302.

[46] A.R. Oganov and S. Ono, *The high pressure phase of alumina and implications for Earth's D" layer*, Proc. Natl. Acad. Sci. USA 102 (2005), p. 10828.

[47] M. Iuga, G. Steinle-Neumann, and J. Meinhardt, *Ab-initio simulation of elastic constants for some ceramic materials*, Eur. Phys. J. B, Condens. Matter Complex Syst. 58 (2007), p. 127.

[48] P. Vinet, J. Ferrante, J.R. Smith, and J.H. Rose, *A universal equation of state for solids*, J. Phys. Condens. Matter 19 (1986), p. L467.

[49] F. Birch, *Finite elastic strain of cubic crystals*, Phys. Rev. 71 (1947), p. 809.

[50] ———, *Finite strain isotherm and velocities for single-crystal and polycrystalline NaCl at high pressures and* 300 K, J. Geophys. Res. 83 (1978), p. 1257.

[51] L.A. Davis and R.B. Gordon, *Compression of mercury at high pressure*, J. Chem. Phys. 46 (1967), p. 2650.

[52] V.R. Rydberg, *Graphische Darstellung einiger bandenspektroskischer Ergebnisse*, Z. Phys. 73 (1932), p. 376.

[53] F.D. Stacey, B.J. Brennan, and R.D. Irvine, *Finite strain theories and comparisons with seismological data*, Geophys. Surv. 4 (1981), p. 189.

[54] S. Gaurav, B.S. Sharma, S.B. Sharma, and S.C. Upadhyaya, *Analysis of equations of state for solids under high compressions*, Physica B 322 (2002), p. 328.

[55] J. Hama and K. Suito, *Thermoelastic model of minerals: applications to* Al_2O_3, Phys. Chem. Miner. 28 (2001), p. 258.

[56] T.J. Ahrens, D.L. Anderson, and A.E. Ringwood, *Equations of state and crystal structures of high-pressure phases of shocked silicates and oxides*, Rev. Geophys. 7 (1969), p. 667.

[57] D. Erskine, *High-pressure Hugoniot of sapphire*, in *High-Pressure Science Technology*, S.C. Schmidt ed., AIP Press, New York, 1994, pp. 141–143, (Proceedings AIRAPT Colorado Springs 1993).

[58] J.F. Lin, O. Degtyareva, C.T. Prewitt, P. Dera, N. Sata, E. Gregoryanz, H.K. Mao, and R.J. Hemley, *Crystal structure of a high-pressure high-temperature phase of alumina by in situ X-ray diffraction*, Nature Mater. 3 (2004), p. 389.

[59] M. Catti and A. Pavese, *Equation of state of α-Al_2O_3 (corundum) from quasi-harmonic atomistic simulations*, Acta Crystallogr. B 54 (1988), p. 741.

[60] S.P.S. Porto and R.S. Krishnan, *Raman effect of corundum*, J. Chem. Phys. 47 (1967), p. 1009.

[61] G.H. Watson, Jr., W.B. Daniels, and C.S. Wang, *Measurements of Raman intensities and pressure dependence of phonon frequencies in sapphire*, J. Appl. Phys. 52 (1981), p. 956.

[62] J.A. Xu, E. Huang, J.F. Lin, and L.Y. Xu, *Raman study at high pressure and the thermodynamic properties of corundum: application of Kieffer's model*, Am. Miner. 80 (1995), p. 1157.

[63] H. Schober, D. Strauch, and B. Dorner, *Lattice dynamics of sapphire (Al_2O_3)*, Z. Phys. B 92 (1993), p. 273.

[64] R. Heid, D. Strauch, and K.-P. Bohnen, *Ab initio lattice dynamics of sapphire*, Phys. Rev. B 61 (2000), p. 8625.

[65] M. Ashkin, J.H. Parker, and D.W. Feldmann, *Temperature dependence of Raman lines of α-Al_2O_3*, Solid State Commun. 6 (1968), p. 343.

[66] A.S. Barker, *Infrared lattice vibrations and dielectric dispersion in corundum*, Phys. Rev. 132 (1963), p. 1374.

[67] M.E. Innocenzi, R.T. Swimm, M. Bass, R.H. French, A.B. Villaverde, and M.R. Kokta, *Roomtemperature optical absorption in undoped α-Al_2O_3*, J. Appl. Phys. 67 (1990), p. 7542.

[68] Y.S.E. Loh, *Ultraviolet absorption and emission spectrum of ruby and sapphire*, J. Chem. Phys. 44 (1966), p. 1940.

[69] W. Duan, R.M. Wentzcovitch, and K.T. Thomson, *First-principles study of high-pressure alumina polymorphs*, Phys. Rev. B 57 (1998), p. 10363.

[70] D.E. Gray (ed.), *American Institute of Physics Handbook*, 3rd edn., McGraw-Hill, New York, 1973.

[71] J.A. Mandarino, *Refraction, absorption, and biabsorption in synthetic ruby*, Am. Miner. 44 (1959), p. 961.

[72] N.M. Balzaretti, J.P. Denis, and J.A.H. da Jornada, *Variation of the refractive index and polarizability of sapphire under high pressures*, J. Appl. Phys. 73 (1993), p. 1426.

[73] G. Pezzotti, K. Wan, M.C. Munisso, and W. Zhu, *Stress dependence of F^+-center cathodoluminescence of sapphire*, Appl. Phys. Lett. 89 (2006), p. 041908.

[74] R.H. French, *Electronic band structure of Al_2O_3 with comparison to AlON and AlN*, J. Am. Ceram. Soc. 73 (1990), p. 477.

[75] Z.X. Liu, J. Xu, H.P. Scott, Q. Williams, H.K. Mao, and R.J. Hemley, *Moissanite (SiC) as windows and anvils for high-pressure infrared spectroscopy*, Rev. Sci. Instrum. 75 (2004), p. 5026.

[76] R. Graham and W. Brooks, *Shock-wave compression of sapphire from 15 to 420 kbar. The effects of large anisotropic compressions*, J. Phys. Chem. Solids 32 (1971), p. 2311.

[77] D.E. Hare, N.C. Holmes, and D.J. Webb, *Shock-wave-induced optical emission from sapphire in the stress range 12 to 45 GPa: images and spectra*, Phys. Rev. B 66 (2002), p. 014108.

[78] O.V. Fat'yanov, R.L. Webb, and Y.M. Gupta, *Optical transmission through inelastically deformed shocked sapphire: stress and crystal orientation effects*, J. Appl. Phys. 97 (2005), p. 123529.

[79] D.B. Hayes, C.A. Hal, J.R. Asay, and M.D. Knudson, *Continuous index of refraction measurements to 20 GPa in Z-cut sapphire*, J. Appl. Phys. 94 (2003), p. 2331.

[80] S.C. Jones, M.C. Robinson, and Y.M. Gupta, *Ordinary refractive index of sapphire in uniaxial tension and compression along the c axis*, J. Appl. Phys. 93 (2003), p. 1023.

[81] J. Xu and H.K. Mao, *Moissanite, a window for high pressure experiments*, Science 290 (2000), p. 783.

[82] R. Hawke, K. Syassen, and W. Holzapfel, *An apparatus for high pressure Raman spectroscopy*, Rev. Sci. Instrum. 45 (1974), p. 1598.

[83] I.N. Goncharenko, *Neutron diffraction experiments in diamond and sapphire anvil cells*, High Press. Res. 24 (2004), p. 193.

[84] W. Wittke, A. Hatta, and A. Otto, *Efficient use of the surface plasmon resonance in light scattering from adsorbates*, Appl. Phys. A 48 (1989), p. 289.

[85] K.J. Takano and M. Wakatsuki, *An optical high pressure cell with spherical sapphire anvils*, Rev. Sci. Instrum. 62 (1991), p. 1576.

[86] K.R. Hirsch and W.B. Holzapfel, *Diamond anvil high-pressure-cell for Raman-spectroscopy*, Rev. Sci. Instrum. 52 (1981), p. 52.

[87] *Landold-Börnstein, Crystal Structure Data of Inorganic Compounds New Series Vol. III/7b1*, Springer, Berlin, 1975.

[88] C. Wolverton and K.C. Hass, *Phase stability and structure of spinel-based transition aluminas*, Phys. Rev. B 63 (2000), p. 024102.

[89] G. Gutierrez, A. Taga, and B. Johansson, *Theoretical structure determination of γ-Al_2O_3*, Phys. Rev. B 65 (2001), p. 1.

[90] Z. Lodziana and K. Parlinski, *Dynamical stability of the α and θ phases of alumina*, Phys. Rev. B 67 (2003), p. 174106.

[91] S.N. Vaidya, C. Karunakaran, R.V. Kamath, K.T. Pillai, and V.N. Vaidya, *New polymorphs of alumina*, High Press. Res. 16 (1999), p. 147.

[92] N. Vaidya, C. Karunakaran, S.N. Achary, and A.K. Tyagi, *New polymorphs of alumina: Part II μ and λ alumina*, High Press. Res. 16 (1999), p. 265.

[93] R.E. Cohen, *Calculation of elasticity and high pressure instabilities in corundum and stishovite with the potential induced breathing model*, Geophys. Res. Lett. 14 (1987), p. 37.

[94] H. Cynn, D.G. Isaak, R.E. Cohen, M.F. Nicol, and O.L. Anderson, *A high-pressure phase transition of corundum predicted by the potential induced breathing model*, Am. Miner. 75 (1990), p. 439.

[95] F.C. Marton and R.E. Cohen, *Prediction of a high-pressure phase transition in Al_2O_3*, Am. Miner. 79 (1994), p. 789.

[96] K.T. Thomson, R.M. Wentzcovitch, and M.S.T. Bukowinski, *Polymorphs of alumina predicted by first principles: putting pressure on the ruby pressure scale*, Science 274 (1996), p. 1880.

[97] W. Duan, G. Paiva, R.M. Wentzcovitch, and A. Fazzio, *Optical transitions in ruby across the corundum to Rh_2O_3 (II) phase transformation*, Phys. Rev. Lett. 81 (1998), p. 3267.

[98] M. Wilson, *High-pressure phase behavior of alumina: predictions of a transferable ionic potential model*, J. Am. Ceram. Soc. 81 (1998), p. 255864.

[99] N. Funamori and R. Jeanloz, *High-pressure transformation of Al_2O_3*, Science 278 (1997), p. 1109.

[100] P. Matkovic and K. Schubert, *Kristallstruktur von Pd_3Te_2*, J. Less-Common Met. 52 (1977), p. 217.

[101] T. Mashimo, K. Tsumoto, K. Nakamura, Y. Noguchi, K. Fukuoka, and Y. Syono, *High pressure phase transformation of corundum observed under shock compression*, Geophys. Res. Lett. 27 (2000), p. 2021.

[102] S.T. Weir, M.C. Mitchell, and W.J. Nellis, *Electrical resistivity of single-crystal Al_2O_3 shockcompressed in the pressure range 91 to 220 GPa*, J. Appl. Phys. 80 (1996), p. 1522.

[103] J. Hama and K. Suito, *The evidence for the occurrence of two successive transitions in Al_2O_3 from the analysis of Hugoniot data*, High Temp. - High Press. 34 (2002), p. 323.

[104] J. Tsuchiya, T. Tsuchiya, and R.M. Wentzcovitch, *Transition from the Rh_2O_3(II)-to-$CaIrO_3$ structure and the high-pressure-temperature phase diagram of alumina*, Phys. Rev. B 72 (2005), p. 20103.

[105] S. Ono, A.R. Oganov, T. Koyama, and H. Shimizu, *Stability and compressibility of the high-pressure phases of Al_2O_3 up to 200 GPa: implications for the electrical conductivity of the base of the lower mantle*, Earth Planet. Sci. Lett. 246 (2006), p. 326.

[106] S. Jahn, P.A. Madden, and M. Wilson, *Transferable interaction model for Al_2O_3*, Phys. Rev. B 74 (2006), p. 024112.

[107] S. Jahn, P.A. Madden, and M. Wilson, *Dynamic simulation of pressure-driven phase transformations in crystalline A_2O_3*, Phys. Rev. B 69 (2004), p. 020106.

[108] H.K. Mao, R.J. Hemley, and M. Hanfland, *Stability of ruby in solid hydrogen at megabar pressures*, Phys. Rev. B 45 (1992), p. 8108.

[109] A.L. Ruoff, H. Luo, and Y.K. Vohra, *The closing diamond anvil optical window in multimegabar research*, J. Appl. Phys. 69 (1991), p. 6413.

[110] S. Sugano and Y. Tanabe, *Absorpion spectra of Cr^{3+} in Al_2O_3, Part A. Theoretical studies of the absorption bands and lines*, J. Phys. Soc. Jpn. 13 (1958), p. 880.

[111] S. Sugano and I. Tsujikawa, *Absorption spectra of Cr^{3+} in Al_2O_3, Part B. Experimental studies of the Zeeman effect and other properties of the line spectra*, J. Phys. Soc. Jpn. 13 (1958), p. 899.

[112] A.L. Schawlow, D.L. Wood, and A.M. Clogston, *Electronic spectra of exchange-coupled ion pairs in crystals*, Phys. Rev. Lett. 3 (1959), p. 271.

[113] D.S. McClure, *Electronic spectra of molecules and ions in crystals part II, spectra of ions in crystals*, in *Solid State Physics Vol.* 9, F. Seitz and D. Turnbull, eds., Academic Press, New York, 1959, pp. 399–524.

[114] R.A. Ford, *Polarized absorption spectrum of ruby between 14,400 and 16,000 cm^{-1} at 100 K*, Spectrochim. Acta 16 (1960), p. 582.

[115] W. Low, *Absorption lines of Cr^{3+} in ruby*, J. Chem. Phys. 33 (1960), p. 1162.

[116] A. Linz and R.E. Newnham, *Ultraviolet absorption spectra in ruby*, Phys. Rev. 123 (1961), p. 500.

[117] A.L. Schawlow, *Fine structure and properties of chromium fluorescence in aluminum and magnesium oxide*, in *Advances in Quantum Electronics*, J.R. Singer ed., Columbia University Press, New York, 1961, pp. 50–62.

[118] G.K. Klauminzer, P.L. Scott, and H.W. Moos, $^2E \rightarrow {}^2T_2$ *absorption spectrum of ruby*, Phys. Rev. 142 (1966), p. 248.

[119] T. Kushida and M. Kukuchi, *R, R', and B absoption linewidths and phonon-induced relaxations in ruby*, J. Phys. Soc. Jpn. 23 (1967), p. 1333.

[120] H. du Bois and G.J. Elias, *Der Einfluss von Temperatur und Magnetisierung bei selektiven Absorptions- und Fluoreszenzspektren*, Ann. Phys. 27 (1908), p. 233.

[121] K.S. Gibson, *The effect of temperature upon the absorption spectrum of a synthetic ruby*, Phys. Rev. 8 (1916), p. 38.

[122] O. Deutschbein, *Die linienhafte Emission und Absorption der Chromphosphore I*, Ann. Phys. 14 (1932), p. 712.

[123] ———, *Die linienhafte Emission und Absorption der Chromphosphore III; Verhalten bei tiefen Temperaturen und im Magnetfeld*, Ann. Phys. 20 (1934), p. 828.

[124] C.J. Ballhausen, *Introduction to ligand field theory*, McGraw-Hill Book Company, New York, 1962.

[125] H. Schläfer and L. Gliemann, *Basic principles of ligand field theory*, Wiley Interscience, 1969, German version: *Einführung in die Ligandenfeldtheorie*, Akademische Verl.-Ges., Frankfurt, 1967.

[126] D. Reinen, *Ligand-field spectroscopy and chemical bonding in Cr^{3+}-containing oxidic solids*, Struct. Bond. 6 (1969), p. 30.

[127] T.H. Maiman, *Optical and microwave-optical experiments in ruby*, Phys. Rev. Lett. 4 (1960), p. 564.

[128] D.S. McClure, *Optical spectra of transition-metal ions in corundum*, J. Chem. Phys. 36 (1962) p. 2757; Erratum, J. Chem. Phys. 37 (1962), p. 1571.

[129] R.M. Macfarlane, *Analysis of the spectrum of d^3 ions in trigonal crystal fields*, J. Chem. Phys. 39 (1963), p. 3118.

[130] D.F. Nelson and M.D. Sturge, *Relation between absorption and emission in the region of the R lines of ruby*, Phys. Rev. A 137 (1965), p. 1117.

[131] A.A. Kaplyanskii and A.K. Przhevuskii, *The piezospectroscopic effect in ruby crystals*, Sov. Phys.-Dokl. 7 (1962), p. 3740.

[132] E. Feher and M.D. Sturge, *Effect of stress on the trigonal splittings of d^3 ions in sapphire (α-Al_2O_3)*, Phys. Rev. 172 (1968), p. 244.

[133] G.F. Imbusch, *Energy transfer in ruby*, Phys. Rev. 153 (1967), p. 326.

[134] S.K. Lyo, *Critical concentration for single-ion-single-ion energy transfer in ruby*, Phys. Rev. B 3 (1971), p. 3331.

[135] A. Szabo, *Laser-Induced fluorescence line narrowing in ruby*, Phys. Rev. Lett. 25 (1970), p. 924.

[136] ———, *Observation of the optical analog of the Mössbauer effect in ruby*, Phys. Rev. Lett. 27 (1971), p. 323.

[137] ———, *Observation of hole burning and cross relaxation effects in ruby*, Phys. Rev. B 11 (1975), p. 4512.

[138] P.M. Selzer, D.S. Hamilton, and W.M. Yen, *Nonradiative spectral and spatial energy transfer in ruby*, Phys. Rev. Lett. 38 (1977), p. 858.

[139] P.M. Selzer, D.L. Huber, B.B. Barnett, and W.M. Yen, *Fluorescence-line-narrowing and energy transfer studies in ruby*, Phys. Rev. B 17 (1978), p. 4979.

[140] E. Thilo, J. Jander, and H. Seemann, *Die Farbe des Rubins und der* $(Al, Cr)_2O_3$ *Mischkristalle*, Z. Anorg. Allg. Chem. 219 (1954), p. 2.

[141] J.M. Garcia-Lastra, M.T. Barriuso, J.A. Aramburu, and M. Moreno, *Origin of the different color of ruby and emerald*, Phys. Rev. B 72 (2005), p. 113104.

[142] E. Gaudry, P. Sainctavit, F. Juillot, F. Bondioli, P. Ohresser, and I. Letard, *From the green color of eskolaite to the red color of ruby: an X-ray absorption spectroscopy study*, Phys. Chem. Miner. 32 (2006), p. 710.

[143] R.A. Ford and O.F. Hill, *Vibronic coupling in the* $^4T_{2g}$ *excited state of ruby*, Spectrochim. Acta 16 (1960), p .493.

[144] G.C. Brown, Jr, *Fluorescence lifetimes of ruby*, J. Appl. Phys. 35 (1964), p. 3062.

[145] X. Joos and A. Saur, in A. Eucken (Ed.), *Landoldt-Börnstein: Zahlenwerte und Funktionen aus Physik, Chemie, Astronomie, Geophysik und Technik, 6. Auflage, I. Band: Atom- und Molekularphysik, 1. Teil: Atome und Ionen*, Springer, Berlin, 1950, p. 108.

[146] A.A. Kaplyanskii, A.K. Przhevuskii, and R.B. Rozenbaum, *Concentration-dependent line-shift in optical spectra of ruby*, Sov. Phys. Solid State 10 (1969), p. 1864.

[147] R.A. Noack and W.B. Holzapfel, *Calibration of the ruby pressure scale at low temperatures*, in *High-Pressure Science Technolgy*, K.D. Timmerhaus and M.S. Barber, eds., Plenum, New York, 1979, vol. II, p. 748, Proceedings AIRAPT Boulder 1979.

[148] S.L. Wunder and P.E. Schoen, *Pressure measurement at high temperatures in the diamond anvil cell*, J. Appl. Phys. 52 (1981), p. 3772.

[149] A.F. Goncharov, J.C. Crowhurst, J.K. Dewhurst, and S. Sharma, *Raman spectroscopy of cubic boron nitride under extreme conditions of high pressure and temperature*, Phys. Rev. B 72 (2005), p. 100104.

[150] C. Ulrich, *Untersuchungen elektronischer und gitterdynamischer Eigenschaften von Halbleitern unter hohem Druck*, PhD thesis, Universität Stuttgart, 1997.

[151] D.E. McCumber and M.D. Sturge, *Linewidth and temperature shift of the R lines in ruby*, J. Appl. Phys. 34 (1963), p. 1682.

[152] G.F. Imbusch and Y.M. Yen, *The McCumber and Sturge formula*, J. Lumin. 85 (2000), p. 177.

[153] R.C. Powell, B. DiBartolo, B. Birang, and C.S. Naiman, *Temperature dependence of the widths and positions of the R and N lines in heavily doped ruby*, J. Appl. Phys. 37 (1966), p. 4973.

[154] S. Yamaoka, O. Shimomura, and O. Fukunaga, *Simultaneous measurements of temperature and pressure by the ruby fluorescence line*, Proc. Jpn. Acad. B 56 (1980), p. 103.

[155] S. Buchsbaum, R.L. Mills, and D. Schiferl, *Phase diagram of N_2 determined by Raman spectroscopy from* 15 *to* 300 K *at pressures to* 52 GPa, J. Phys. C Solid State Phys. 88 (1984), p. 2522.

[156] W.L. Vos and J.A. Schouten, *On the temperature correction to the ruby pressure scale*, J. Appl. Phys. 69 (1991), p. 6744.

[157] J. Yen and M. Nicol, *Temperature dependence of the ruby luminescence method for measuring high pressures*, J. Appl. Phys. 72 (1992), p. 5535.

[158] D.D. Ragan, R. Gustavsen, and D. Schiferl, *Calibration of the ruby R_1 and R_2 fluorescence shifts as a function of temperature from* 0 *to* 600 K, J. Appl. Phys. 72 (1992), p. 5539.

[159] T.-H. Huang, C.-C. Hsu, C.-T. Kuo, P. Lu, W.-S. Tse, D.P. Wang, T.C. Chou, and A.Y.G. Fuh, *Ruby spectral band-profile analysis for temperature sensing*, J. Appl. Phys. 75 (1994), p. 3599.

[160] S. Rekhi, L.S. Dubrovinsky, and S.K. Saxena, *Temperature-induced ruby fluorescence shifts up to a pressure of* 15 GPa *in an externally heated diamond anvil cell*, High Temp. - High Press. 31 (1999), p. 299.

[161] J.C. Chervin, B. Canny, and M. Mancinelli, *Ruby-spheres as pressure gauge for optically transparent high pressure cells*, High Press. Res. 21 (2001), p. 305.

[162] B.A. Weinstein, *Ruby thermometer for cryobaric diamond anvil cell*, Rev. Sci. Instrum. 57 (1986), p. 910.

[163] O. Grasset, *Calibration of the R ruby fluorescence lines in the pressure range* 0–1 GPa *and the temperature range* 250–300 K, High Press. Res. 21 (2001), p. 139.

[164] R.G. Munro, G.J. Piermarini, S. Block, and W.B. Holzapfel, *Model line-shape analysis for the ruby R lines used for pressure measurement*, J. Appl. Phys. 57 (1985), p. 165.

[165] L. Vina, S. Logothetidis, and M. Cardona, *Temperature dependence of the dielectric function of germanium*, Phys. Rev. B 30 (1984), p. 1979.

[166] P.Y. Yu and M. Cardona, *Fundamentals of Semiconductors*, Springer, Berlin, 1996, (3rd edn., 2001).

[167] J. He and D.R. Clarke, *The piezo-spectroscopic coefficients for Cr-doped sapphire*, J. Am. Chem. Soc. 78 (1995), p. 1347.

[168] J.H. Eggert, K.A. Goettel, and I.F. Silvera, *Elimination of pressure-induced fluorescence in diamond anvils*, Appl. Phys. Lett. 53 (1988), p. 2489.

[169] ———, *Ruby at high pressure. I. Optical line shifts to 156 GPa*, Phys. Rev. B 40 (1989), p. 5724.

[170] ———, *Ruby at High Pressure II. Fluorescence lifetime of the R-line to 130 GPa*, Phys. Rev. B 40 (1989), p. 5733.

[171] J.H. Eggert, F. Moshary, W.J. Evans, K.A. Goettel, and I.F. Silvera, *Ruby at high-pressure III. A pumping scheme for the R-lines up to 230 GPa*, Phys. Rev. B 44 (1991), p. 7202.

[172] Y.K. Vohra, C.A. Vanderborgh, S. Desgreniers, and A.L. Ruoff, *Comment on "Ruby at high pressure. I. Optical line shifts to 156 GPa"*, Phys. Rev. B 42 (1990), p. 9189.

[173] J.H. Eggert, K.A. Goettel, and I.F. Silvera, *Reply to "Comment on 'Ruby at high pressure. I. Optical line shifts to 156 GPa'"*, Phys. Rev. B 42 (1990), p. 9191.

[174] D.R. Stephens and H.G. Drickamer, *Effect of pressure on the spectrum of ruby*, J. Chem. Phys. 35 (1961), p. 427.

[175] S.J. Duclos, Y. Vohra, and A.L. Ruoff, *Absorption bands of ruby to 35 GPa*, Phys. Rev. B 41 (1990), p. 5372.

[176] N.H. Chen and I.F. Silvera, *Excitation of ruby fluorescence at multimegabar pressures*, Rev. Sci. Instrum. 67 (1996), p. 4275.

[177] L.D. Merkle, I.L. Spain, and R.C. Powell, *Effects of pressure on the spectra and lifetimes of $Nd_xY_{1-x}P_5O_{14}$ and ruby*, J. Phys. C Solid State Phys. 14 (1981), p. 2027.

[178] Y. Sato-Sorensen, *Measurements of the lifetime of the ruby R_1 line under high pressure*, J. Appl. Phys. 60 (1986), p. 2985.

[179] M. Grinberg and T. Orlikowski, *The adiabatic model of electronic and vibronic structure of $2E,2T1$, and $4T2$ spinorbit coupled states. Ruby fluorescence decay time under pressure*, J. Lumin. 53 (1992), p. 447.

[180] B.R. Jovanovic, *Lifetime of the ruby R_1 line under ultrahigh pressure*, Chem. Phys. Lett. 190 (1992), p. 440.

[181] Y.R. Shen and K.L. Bray, *Effect of pressure and temperature on the lifetime of Cr^{3+} in yttrium aluminum garnet*, Phys. Rev. B 56 (1997), p. 10882.

[182] M.I. Eremets, *Megabar high-pressure cell for Raman measurements*, J. Raman Spectrosc. 34 (2003), p. 515.

[183] S.M. Sharma and Y.M. Gupta, *Analysis of the absorption spectrum of ruby at high pressures*, Phys. Rev. B 40 (1989), p. 3329.

[184] ———, *Oscillator strength of ruby R_1 line under high pressure*, Appl. Phys. Lett. 54 (1989), p. 84.

[185] ———, *Theoretical analysis of R-line shifts of ruby subjected to different deformation conditions*, Phys. Rev. B 43 (1991), p. 879.

[186] X.A. Shen and Y.M. Gupta, *Effect of crystal orientation on ruby R-line shifts under shock compression and tension*, Phys. Rev. B 48 (1993), p. 2929.

[187] D.-D. Ma, X.-T. Zheng, X.-S. Xu, and Z.-G. Zhang, *Theoretical calculations of the R_1 red shift of ruby under high pressure*, Phys. Rev. A 115 (1986), p. 245.

[188] D.-D. Ma, Z.-Q. Wang, J.-R. Chen, and Z.-G. Zhang, *Theoretical calculations of pressure-induced blue and red shifts of spectra of ruby*, J. Phys. C Solid State Phys. 21 (1988), p. 3585.

[189] D.P. Ma, *Theoretical calculations of the pressure-induced shifts of the entire energy spectrum of ruby*, J. Phys. Condens. Matter 7 (1995), p. 4883.

[190] ———, *Theoretical calculation of optical and EPR spectra and their pressure-induced shifts for ruby*, J. Phys. Chem. Solids 60 (1999), p. 463.

[191] D.P. Ma, Y.Y. Liu, N. Ma, and J.R. Chen, *Theoretical calculations of thermal shifts and thermal broadenings of sharp lines and zero-field splitting for ruby. Part I. Thermal shifts of R_1 and R_2 lines*, J. Phys. Chem. Solids 61 (2000), p. 799.

[192] M.G. Zhao, *Microscopic origin of the high-pressure-induced spectral shifts in ruby*, J. Chem. Phys. 109 (1998), p. 8003.

[193] I. Fujishiro, Y. Nakamura, T. Kawase, and B. Okai, *The property of a ruby high pressure sensor under uniaxial compressive stress*, JSME Int. J. 3, Vib. Control Eng. Eng. Ind. 31 (1988), p. 136.

[194] L. Grabner, *Spectroscopic technique for the measurement of residual stress in sintered Al_2O_3*, J. Appl. Phys. 49 (1978), p. 580.

[195] Q. Ma and D.R. Clarke, *Piezo-spectroscopic determination of residual stresses in polycrystalline alumina*, J. ACM 77 (1994), p. 298.

[196] M.R. Gallas, Y.C. Chu, and G.J. Piermarini, *Calibration of the Raman effect in α-Al_2O_3 ceramic for residual stress measurements*, J. Mater. Res. 10 (1995), p. 2817.

[197] J. He and D.R. Clarke, *Polarization dependence of the Cr^{3+} R-line fluorescence from sapphire and its application to crystal orientation and piezospectroscopic measurement*, J. ACM 80 (1997), p. 69.

[198] P. Kizler, J. He, D.R. Clarke, and P.R. Kenway, *Structural relaxation around substitutional Cr^{3+} ions in sapphire*, J. ACM 79 (1996), p. 3.

[199] Y.M. Gupta and X.A. Shen, *Potential use of the ruby R_2 line shift for static high-pressure calibration*, Appl. Phys. Lett. 58 (1991), p. 583.

[200] M. Chai and J.M. Brown, *Effects of static non-hydrostatic stress on the R lines of ruby single crystals*, Geophys. Res. Lett. 23 (1996), p. 3539.

[201] S.H. Margueron and D.R. Clarke, *Stress anisotropy of the R-line luminescence lifetime in single crystal Cr-doped sapphire (ruby)*, J. Appl. Phys. 101 (2007), p. 093521.

[202] P.D. Horn and Y.M. Gupta, *Wavelength shift of the ruby luminescence R lines under shock compression*, Appl. Phys. Lett. 49 (1986), p. 856.

[203] ———, *Luminescence R-line spectrum of ruby crystals shocked to* 125 kbar *along the crystal c axis*, Phys. Rev. B 39 (1989), p. 973.

[204] S.M. Sharma and Y.M. Gupta, *Erratum: theoretical-analysis of R-line shifts of ruby subjected to different deformation conditions*, Phys. Rev. B 48 (1993), p. 3579.

[205] Y.M. Gupta, P.D. Horn, and J.A. Burt, *Effect of tension on R-lines in ruby crystals shocked along crystal c-axis*, J. Appl. Phys. 76 (1994), p. 1784.

[206] J.K. Hyun, S.M. Sharma, and Y.M. Gupta, *Ruby R-line shifts for shock compression along* (1-102), J. Appl. Phys. 84 (1998), p. 1947.

[207] M.D. Knudson and Y.M. Gupta, *Feasibility of stimulated emission to measure R-line shifts in shock compressed ruby*, J. Appl. Phys. 85 (1999), p. 6425.

[208] T. Goto, T.J. Ahrens, and G.R. Rossman, *Absorption spectra of Cr^{3+} in Al_2O_3 under shock compression*, Phys. Chem. Miner. 4 (1979), p. 253.

[209] T. Kobayashi, T. Sekine, X. Li, and Y. Yamashita, *Observation of wavelength shifts in ruby under shock compression to* 36 GPa *by time-resolved luminescence spectroscopy*, Phys. Rev. B 69 (2004), p. 054108.

[210] T. Zhou, *Optical spectroscopic studies on transition metal oxisdes under high pressure*, PhD thesis, Universiät Stuttgart, 1998.

[211] R.J. Hemley, C.S. Zha, A.P. Jephcoat, H.K. Mao, and L.W. Finger, *X-ray diffraction and equation of state of solid neon to* 110 GPa, Phys. Rev. B 39 (1989), p. 11820.

[212] C. Meade and R. Jeanloz, *Yield strength of Al_2O_3 at high pressures*, Phys. Rev. B 42 (1990), p. 2532.

[213] U. Rothamel, J. Heber, and W. Grill, *Vibronic sidebands in ruby*, Z. Phys. B Condens. Matter 50 (1983), p. 297.

[214] P. Kisliuk, N.C. Chang, P.L. Scott, and M.H.L. Pryce, *Energy levels of chromium ion pairs in ruby*, Phys. Rev. 184 (1969), p. 367.

[215] M. Naito, *Cr ion pair spectrum in ruby*, J. Phys. Soc. Jpn. 34 (1973), p. 1491.

[216] L. Zhang and A. Chopelas, *Sound velocity of Al_2O_3 to* 616 kbar, Phys. Earth Planet. Inter. 87 (1994), p. 77.

[217] R.G. Munro, *Theory of pressure-dependence of a prototype exchange integral*, Phys. Rev. B 17 (1978), p. 4460.

[218] Q. Williams and R. Jeanloz, *Pressure shift of Cr^{3+}-ion-pair emission lines in ruby*, Phys. Rev. B 31 (1985), p. 7449.

[219] A.A. Kaplyanskii and A.K. Przhevuskii, *Deformational splitting of luminescence spectrum lines and structures of exchange-linked pais of chromium ions in ruby*, Sov. Phys. Solid State 9 (1967), p. 190.

[220] L.F. Mollenauer and A.L. Schawlow, *Piezospectroscopic studies of exchange-coupled Cr^{3+} ion pairs in ruby*, Phys. Rev. 168 (1968), p. 309.

[221] R.C. Powell and B. Dibartolo, *Optical properties of heavily doped ruby*, Phys. Status Solidi A 10 (1972), p. 315.

[222] D.L. Decker, W.A. Basset, L. Merill, H.T. Hall, and J.D. Barnett, *High-pressure calibration – a critical review*, J. Phys. Chem. Ref. Data 1 (1972), p. 773.

[223] O.L. Anderson, *The use of ultrasonic measurements under modest pressure to estimate compression at high pressure*, J. Phys. Chem. Solids 27 (1966), p. 547.

[224] O.L. Andersen, D.G. Isaak, and S. Yamamoto, *Anharmonicity and the equation of state of gold*, J. Appl. Phys. 65 (1989), p. 1534.

[225] W.A. Bassett, H.J. Reichmann, R.J. Angel, H. Spetzler, and J.R. Smyth, *New diamond anvil cells for gigahertz ultrasonic interferometry and X-ray diffraction*, Am. Miner. 85 (2000), p. 283.

[226] B. Li, J. Kung, T. Uchida, and Y. Wang, *Pressure calibration to* 20 GPa *by simultaneous use of ultrasonic and X-ray techniques*, J. Appl. Phys. 98 (2005), p. 13521.

[227] C.-S. Zha, H. Mao, and R.J. Hemley, *Elasticity of MgO and a primary pressure scale to* 55 GPa, Proc. Natl. Acad. Sci. USA 97 (2000), p. 13494.

[228] S. Sinogeikin, J. Bass, V. Prakapenka, D. Lakshtanov, G.Y. Shen, C. Sanchez-Valle, and M. Rivers, *Brillouin spectrometer interfaced with synchrotron radiation for simultaneous X-ray density and acoustic velocity measurements*, Rev. Sci. Instrum. 77 (2006), p. 103905.

[229] W.J. Nellis, *Adiabat-reduced isotherms at* 100 GPa *pressures*, High Press. Res. 27 (2007), p. 393.

[230] ———, *Dynamic high-pressure effects in solids*, Encycl. Appl. Phys. 5 (1997), p. 541.

[231] W.B. Holzapfel, M. Hartwig, and W. Sievers, *Equations of state for Cu, Ag, and Au for wide ranges in temperature and pressure up to* 500 GPa *and above*, J. Phys. Chem. Ref. Data 30 (2001), p. 515.

[232] P.L. Dorogokupets and A.R. Oganov, *Equations of State of Cu and Ag and revised ruby pressure scale*, Dokl. Akad. Nauk 391 (2003), p. 515; Dokl. Earth Sci. 391A (2003), p. 854, (English Translation).

[233] A.D. Chijioke, W.J. Nellis, and I.F. Silvera, *High pressure equations of state of Al, Cu, Ta, and W*, J. Appl. Phys. 98 (2005), p. 73526.

[234] W.B. Holzapfel and M.F. Nicol, *Refined equations of state for Cu, Ag, and Au in the sub-Tpa region*, High Press. Res. 27 (2007), p. 377.

[235] Y. Wang, R. Ahuja, and B. Johansson, *Reduction of shock-wave data with mean-field potential approach*, J. Appl. Phys. 92 (2002), p. 6616.

[236] K. Syassen and K. Kunc, *Note on EOS parameters of solids from DFT*, unpublished, 2005.

[237] Z. Wu and R.E. Cohen, *More accurate generalized gradient approximation for solids*, Phys. Rev. B 73 (2006), p. 235116.

[238] K. Kunc, I. Loa, and K. Syassen, *Equation of state and phonon frequency calculations of diamond at high pressure*, Phys. Rev. B 68 (2003), p. 94107.

[239] K. Nakano, Y. Akahama, and Y. Ohishi, *Ruby scale at low temperatures calibrated by the NaCl gauge: wavelength shift of ruby R_1 fluorescence line at high pressure and low temperature*, Jpn. J. Appl. Phys. 39 (3A) (2000), p. 1249.

[240] D.L. Decker, *High-pressure equation of state for NaCl, KCl, and CsCl*, J. Appl. Phys. 42 (1971), p. 3239.

[241] W.B. Holzapfel, *Refinement of the ruby luminescence pressure scale*, J. Appl. Phys. 93 (2003), p. 1813.

[242] I.V. Aleksandrov, A.F. Goncharov, A.N. Zisman, and S.M. Stishov, *Diamond at high pressures: Raman scattering of light, equation of state, and high-pressure scale*, Sov. Phys. - JETP 66 (1987), p. 384.

[243] K. Kunc, I. Loa, and K. Syassen, *Equation of state and phonon frequency calculations of diamond revisited*, High Press. Res. 24 (2004), p. 101.

[244] A. Dewaele, P. Loubeyre, and M. Mezouar, *Equations of state of six metals above 94 GPa*, Phys. Rev. B 70 (2004), p. 94112.

[245] W.B. Holzapfel, *Progress in the realization of a practical pressure scale for the range 1–300 GPa*, High Press. Res. 25 (2005), p. 87.

[246] A.D. Chijioke, W.J. Nellis, A. Soldatov, and I.F. Silvera, *The ruby pressure standard to 150 GPa*, J. Appl. Phys. 98 (2005), p. 114905.

[247] P.I. Dorogokupets and A.R. Oganov, *Ruby pressure scale: revision and alternatives*, Proceedings Joint 20th AIRAPT and 43th EHPRG International Conference on High Pressure Science and Technology, June 27 to July 1, 2005, Karlsruhe/Germany (Forschungszentrum Karlsruhe, Karlsruhe, 2005), CD-ROM version.

[248] P.I. Dorogokupets and A.R. Oganov, *Equations of state of Al, Au, Cu, Pt, Ta, and W and revised ruby pressure scale*, Dokl. Earth Sci. (Dokl. Akad. Nauk) 410 (2006), p. 239243.

[249] ———, *Ruby, metals, and MgO as alternative pressure scales: a semiempirical description of shock-wave, ultrasonic, X-ray, and thermochemical data at high temperatures and pressures*, Phys. Rev. B 75 (2007), p. 024115.

[250] F. Occelli, P. Loubeyre, and R. LeToullec, *Properties of diamond under hydrostatic pressures to 140 GPa*, Nature Mater. 2 (2003), p. 151.

[251] M. Hanfland, K. Syassen, S. Fahy, S.G. Louie, and M.L. Cohen, *Pressure dependence of the firstorder Raman mode in diamond*, Phys. Rev. B 31 (1985), p. 6896.

[252] W.F. Sherman, *The diamond Raman band as a high-pressure calibrant*, J. Phys. C Solid State Phys. 18 (1985), p. L973.

[253] M. Hanfland, K. Syassen, and J. Koehler, *Pressure-volume relation of tantalum*, J. Appl. Phys. 91 (2002), p. 4143.

[254] R. LeToullec and P. Loubeyre, Abstracts booklet, AIRAPT Conference, Beijing, 2001.

[255] I.F. Silvera, A.D. Chijioke, W.J. Nellis, A. Soldatov, and J. Tempere, *Calibration of the ruby pressure scale to 150 GPa*, Phys. Status Solidi B 244 (2007), p. 460.

[256] P.I. Dorogokupets and A. Dewaele, *Equations of state of MgO, Au, Pt, NaCl-B1, and NaCl-B2: internally consistent high-temperature pressure scales*, High Press. Res. 27 (2007), p. 431.

[257] R.W. Ogden, *Nonlinear Elastic Deformations*, Horwood, Chichester, 1984, Republished by Dover.

[258] B.N. Taylor and C.E. Kuyatt, *NIST Technical note 1297 1994 edition: guidelines for evaluating and expressing the uncertainty of NIST measurement results*, Tech. Rep. NIST, 1994.

[259] A.K. Singh and G.C. Kennedy, *Uniaxial stress components in tungsten carbide anvil high pressure X-ray cameras*, J. Appl. Phys. 45 (1974), p. 4686.

[260] A.L. Ruoff, *Stress anisotropy in opposed-anvil high pressure cells*, J. Appl. Phys. 46 (1975), p. 1389.

[261] G.L. Kinsland and W.A. Bassett, *Modification of the diamond anvil cell for measuring strain and the strength of materials at pressures up to 300 kbar*, Rev. Sci. Instrum. 47 (1976), p. 130.

[262] A.K. Singh, H.-K. Mao, J. Shu, and R.J. Hemley, *Estimation of single-srystal elastic moduli from polycrystalline X-ray diffraction at high pressure: application to FeO and iron*, Phys. Rev. Lett. 80 (1998), p. 2157.

[263] A.K. Singh, C. Balasingh, H.K. Mao, R.J. Hemley, and J. Shu, *Analysis of lattice strains measured under nonhydrostatic pressure*, J. Appl. Phys. 83 (1998), p. 7567.

[264] T.S. Duffy, G. Shen, D.L. Heinz, J. Shu, Y. Ma, H.-K. Mao, R.J. Hemley, and A.K. Singh, *Lattice strains in gold and rhenium under nonhydrostatic compression to 37 GPa*, Phys. Rev. B 60 (1999), p. 15063.

[265] A. Kavner and T.S. Duffy, *Elasticity and rheology of platinum under high pressure and nonhydrostatic stress*, Phys. Rev. B 68 (2003), p. 144101.

[266] A.K. Singh, H.-P. Liermann, Y. Akahama, and H. Kawamura, *Aluminum as a pressure-transmitting medium cum pressure standard for X-ray diffraction experiments to 200 GPa with diamond anvil cells*, J. Appl. Phys. 101 (2007), p. 123526.

[267] K. Takemura, *Evaluation of the hydrostaticity of a helium-pressure medium with powder X-ray diffraction techniques*, J. Appl. Phys. 89 (2001), p. 662.

[268] A.K. Singh and K. Takemura, *Measurement and analysis of nonhydrostatic lattice strain component in niobium to 145 GPa under various fluid pressure-transmitting media*, J. Appl. Phys. 90 (2001), p. 3269.

[269] K. Takemura and A.K. Singh, *High-pressure equation of state for Nb with a helium pressure medium: powder X-ray diffraction experiments*, Phys. Rev. B 73 (2006), p. 224119.

[270] K. Takemura, *Pressure scales and hydrostaticity*, High Press. Res. 27 (2007), p. 465.

[271] F. Datchi, P. Loubeyre, and R. LeToullec, *Extended and accurate determination of the melting curves of argon, helium, ice (H_2O), and hydrogen (H_2)*, Phys. Rev. B 61 (2000), p. 6535.

[272] Z. Nabi, L. Vitos, B. Johansson, and R. Ahuja, *Ab initio calculation of elastic properties of solid He under pressure*, Phys. Rev. B 72 (2005), p. 172102.

[273] A. Dewaele and P. Loubeyre, *Pressurizing conditions in helium pressure-transmitting medium*, High Press. Res. 27 (2007), p. 419.

[274] I. Loa, X. Wang, K. Syassen, and M. Hanfland, *Low-temperature high-pressure X-ray diffraction studies of structural phase transitions of germanium*, unpublished.

[275] Y. Fei, A. Ricolleau, M. Frank, K. Mibe, G. Shen, and V. Prakapenka, *High-Pressure Geoscience Special Feature: toward an internally consistent pressure scale*, Proc. Natl. Acad. Sci. 104 (2007), p. 9182, http://www.pnas.org/cgi/reprint/104/22/9182.pdf

[276] P.M. Bell, H.K. Mao, and K. Goettel, *Ultrahigh pressure: beyond* 2 *megabars and the ruby fluorescence scale*, Science 226 (1984), p. 542.

[277] J.A. Xu, H.K. Mao, and P.M. Bell, *High-pressure ruby and diamond fluorescence: observations at* 0.21 *to* 0.55 *Terapascal*, Science 232 (1986), p. 1404.

[278] M.I. Eremets, I.A. Trojan, P. Gwaze, J. Huth, R. Boehler, and V.D. Blank, *The strength of diamond*, Appl. Phys. Lett. 87 (2005), p. 141902.

[279] M. Hanfland, I. Loa, and K. Syassen, *Sodium under pressure: bcc to fcc transition and pressurevolume relation to* 100 GPa, Phys. Rev. B 65 (2002), p. 184109.

[280] R.E. Cohen, O. Gulseren, and R.J. Hemley, *Accuracy of equation-of-state-formulations*, Am. Miner. 85 (2000), p. 338.

[281] A. Lacam and C. Chateau, *High-pressure measurements at moderate temperatures in a diamond anvil cell with a new optical sensor:* $SrB_4O_7:Sm^{2+}$, J. Appl. Phys. 66 (1989), p. 366.

[282] J.M. Leger, C. Chateau, and A. Lacam, $SrB_4O_7:Sm^{2+}$ *pressure optical sensor: investigations in the megabar regime*, J. Appl. Phys. 68 (1990), p. 2351.

[283] N.J. Hess and D. Schiferl, *Pressure and temperature dependence of laser-induced fluorescence of Sm:YAG at* 100 kbar *and* 700 C *and an empirical model*, J. Appl. Phys. 68 (1990), p. 1953.

[284] ———, *Comparison of the pressure-induced frequency shift of Sm:YAG to the ruby and nitrogen vibron pressure scales from* 6 *to* 820 K *and* 0 *to* 25 GPa *and suggestions for use as a high-temperature pressure calibrant*, J. Appl. Phys. 71 (1992), p. 2082.

[285] J. Liu and K. Vohra, *Photoluminescence and X-ray diffraction studies on Sm-doped yttrium aluminum garnet to ultrahigh pressures*, J. Appl. Phys. 79 (1996), p. 7978.

[286] F. Datchi, R. LeToullec, and P. Loubeyre, *Improved calibration of the* $SrB_4O_7:Sm^{2+}$ *optical pressure gauge: advantages at very high pressures and high temperatures*, J. Appl. Phys. 81 (1997), p. 3333.

[287] Y. Zhao, W.A. Barvosa-Carter, S.D. Theiss, S. Mitha, M.J. Aziz, and D. Schiferl, *Pressure measurement at high temperatures using ten Sm:YAG flourescence peaks*, J. Appl. Phys. 84 (1998), p. 4049.

[288] C. Sanchez-Valle, I. Daniel, B. Reynard, R. Abraham, and C. Goutaudier, *Optimization of* Sm^{3+} *fluorescence in Sm-doped yttrium aluminum garnet: application to pressure calibration in diamond anvil cell at high temperature*, J. Appl. Phys. 92 (2002), p. 4349.

[289] A.F. Goncharov, J.M. Zaug, J.C. Crowhurst, and E. Gregoryanz, *Optical calibration of pressure sensors for high pressures and temperatures*, J. Appl. Phys. 97 (2005), p. 094917.

[290] F. Datchi, A. Dewaele, P. Loubeyre, R. Letoullec, Y.L. Godec, and B. Canny, *Optical pressure sensors for high-pressure high-temperature studies in a diamond anvil cell*, High Press. Res. 27 (2007), p. 447.

[291] A.H. Jahren, M.B. Kruger, and R. Jeanloz, *Alexandrite as a high-temperature pressure calibrant, and implications for the ruby-fluorescence scale*, J. Appl. Phys. 71 (1992), p. 1579.

[292] D. Schiferl, M. Nicol, J.M. Zaug, S.K. Sharma, T.F. Cooney, S.Y. Wang, T.R. Anthony, and J.F. Fleischer, *The diamond C*-13/*C*-12 *isotope Raman pressure sensor system for high-temperature/pressure diamond anvil cells with reactive samples*, J. Appl. Phys. 82 (1997), p. 3256.

[293] O.H. Nielsen, *Optical phonons and elasticity of diamond at megabar stresses*, Phys. Rev. B 34 (1986), p. 5808.

[294] R. Maezono, A. Ma, M.D. Towler, and R.J. Needs, *Equation of state and Raman frequency of diamond from quantum Monte Carlo simulations*, Phys. Rev. Lett. 98 (2007), p. 025701.

[295] O.H. Nielsen and K. Kunc, *Optical Phonons in Boron Nitride Under Very High Pressures, In Festschrift In Honor of R. C. Leite*, World Scientific, Singapore, 1991, pp. 112–123.

[296] F. Datchi and B. Canny, *Raman spectrum of cubic boron nitride at high pressure and temperature*, Phys. Rev. B 69 (2004), p. 144106.

[297] F. Datchi, A. Dewaele, Y.L. Godec, and P. Loubeyre, *Equation of state of cubic boron nitride at high pressures and temperatures*, Phys. Rev. B 75 (2007), p. 214104.

[298] A.F. Goncharov, S. Sinogeikin, J.C. Crowhurst, M. Ahart, D. Lakshtanov, V. Prakapenka, J. Bass, P. Beck, S.N. Tkachev, J.M. Zaug, and Y. Fei, *Cubic boron nitride as a primary calibrant for a high temperature pressure scale*, High Press. Res. 27 (2007), p. 409.

[299] F. Aguado and V.G. Baonza, *Prediction of bulk modulus at high temperatures from longitudinal phonon frequencies: application to diamond, c-BN, and* 3*C-SiC*, Phys. Rev. B 73 (2006), p. 024111.

[300] M. Popov, *Pressure measurement from Raman spectra of stressed diamond*, J. Appl. Phys. 95 (2004), p. 5509.

[301] Y. Akahama and H. Kawamura, *High-pressure Raman soectroscopy of diamond anvils to* 250 GPa*: method for pressure determination in the multimegabar pressure range*, J. Appl. Phys. 96 (2004), p. 3748.

[302] L. Sun, A.L. Ruoff, and G. Stupian, *Convenient optical pressure gauge for multimegabar pressures calibrated to* 300 GPa, Appl. Phys. Lett. 86 (2005), p. 14103.

[303] Y. Akahama and H. Kawamura, *Raman study of the stress state of* 111 *diamond anvils at megabar pressures*, J. Appl. Phys. 98 (2005), p. 83523.

[304] ———, *Pressure calibration of diamond anvil Raman gauge to* 310 GPa, J. Appl. Phys. 100 (2006), p. 43516.

[305] Y. Akahama and H. Kawamura, *Diamond anvil Raman gauge in multimegabar pressure range*, High Press. Res. 27 (2007), p. 473.

[306] M. Hanfland and K. Syassen, *A Raman study of diamond anvils under stress*, J. Appl. Phys. 57 (1985), p. 2752.
[307] S.K. Sharma, H.K. Mao, P.M. Bell, and J.A. Xu, *Measurement of stress in diamond anvils with micro-Raman spectroscopy*, J. Raman Spectr. 16 (1985), p. 350.
[308] M.H. Grimsditch, E. Anastassakis, and M. Cardona, *Effect of uniaxial stress on the zone-center optical phonon of diamond*, Phys. Rev. B 18 (1978), p. 901.
[309] E. Gregoryanz, O. Degtyareva, M. Somayazulu, R.J. Hemley, and H.-K. Mao, *Melting of dense sodium*, Phys. Rev. Lett. 94 (2005), p. 185502.
[310] K. Koyama-Nakazawa, M. Koeda, M. Hedo, and Y. Uwatoko, *In situ pressure calibration for piston cylinder cells via ruby fluorescence with fiber optics*, Rev. Sci. Instrum. 78 (2007), p. 066109.

Appendix 1. Stress and pressure

In the context of pressure calibration, it is useful to recall the definitions of terms in continuum mechanics. A variant of the related remarks by Decker et al. [222] is as follows.

Stress tensor: In order to exactly specify the meanings of mean pressure, deviatoric stress tensor, hydrostatic pressure, and uniaxial pressure, one refers to the stress tensor $[\sigma_{ij}]$. In component form the stress tensor is written as

$$\boldsymbol{\sigma} = \begin{bmatrix} \sigma_{11} & \sigma_{12} & \sigma_{13} \\ \sigma_{21} & \sigma_{22} & \sigma_{23} \\ \sigma_{31} & \sigma_{32} & \sigma_{33} \end{bmatrix}. \tag{A1}$$

The subscripts ij refer to the axes of an orthogonal three-dimensional coordinate system of arbitrary or symmetry-adopted orientation. The scalar components σ_{ij} represent the magnitude of the *internal* forces per unit area. The first index refers to the direction of stress acting on a plane (normal or tangential) and the second index to the direction of the normal of the plane on which the stress acts (Figure A1). An alternative definition exists where indices are reversed. Each component of $[\sigma_{ij}]$, in general, depends on position and time, $\sigma_{ij}(\mathbf{x}, t)$. So, the stress tensor is a *local* quantity. In static equilibrium, $[\sigma_{ij}]$ is symmetric and has only six independent components. Any symmetric stress tensor can be transformed to the three principal directions of stress. Then, only components on the diagonal can be non-zero.
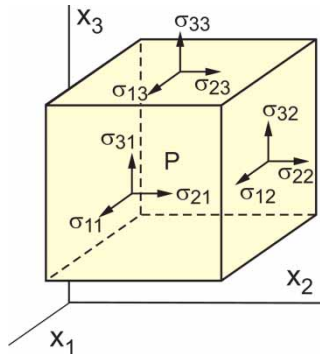

Figure A1. An infinitesimal parallelepiped removed from a stressed body. Shown are the stress components σ_{ij} which the removed part of the body transmits through the facets onto the material inside of the parallelepiped. Besides taking tensile stress as positive, a second convention adopted here is that the first index of a component σ_{ij} refers to the direction of the force and the second index refers to the plane on which the force acts. For the center of the parallelepiped to be at rest, the forces exerted on the cube through the three hidden faces must be equal and opposite to those shown for the visible faces. Furthermore, the absence of any rotational moment imposes the symmetry $\sigma_{ij} = \sigma_{ji}$.

Mean pressure and deviatoric stress tensor: These are given by

$$\overline{P}(\boldsymbol{x}, t) = -\frac{1}{3}[\sigma_{11}(\boldsymbol{x}, t) + \sigma_{22}(\boldsymbol{x}, t) + \sigma_{33}(\boldsymbol{x}, t)]$$
$$\tau_{ij}(\boldsymbol{x}, t) = \sigma_{ij}(\boldsymbol{x}, t) - \delta_{ij}\overline{P}(\boldsymbol{x}, t). \tag{A2}$$

The mean pressure $\overline{P}$ is defined as the negative of the average of the three normal (diagonal) stress components. The sum in the square brackets is the trace of the stress tensor; the trace is invariant under rotation of coordinates. All other stresses, *i.e.* the shear stresses, are given by the zero-trace stress tensor $[\tau_{ij}]$. Note that individual diagonal components of $[\tau_{ij}]$ may be non-zero. If the mean pressure $\overline{P}$ is larger compared with the absolute values of all components τ_{ij}, then $[\tau_{ij}]$ is referred to as the deviatoric stress tensor. The deviatoric stress tensor should not be confused with various scalar measures of differential stress, stress ratio, etc.

Hydrostatic pressure: Hydrostatic pressure is characterized by isotropic normal stresses and zero deviatoric stresses, formally written as

$$-P(\mathbf{x}, t) = \sigma_{11}(\boldsymbol{x}, t) = \sigma_{22}(\boldsymbol{x}, t) = \sigma_{33}(\boldsymbol{x}, t)$$
$$\tau_{ij}(\boldsymbol{x}, t) = 0. \tag{A3}$$

These equations define hydrostaticity at a point inside a body at a given time. If an extended region of a body is to be hydrostatic, each point in the volume must satisfy the hydrostatic condition. This does not imply homogeneous (constant in space) stress conditions. However, in static equilibrium, a non-homogeneity of stress can only arise from volume (body type) forces (*e.g.* gravitational, electric, or magnetic field). In a system where stress is homogeneous (constant) in space, hydrostatic, and independent of time, one can simply define pressure as the applied external force per unit area. Such idealized conditions are difficult to realize in solid or high-viscosity environments.

Uniaxial and biaxial stress: Uniaxial stress acts in one direction only; stresses in the two perpendicular directions are zero. Biaxial or plane stress means that stress is zero in one direction. Uniaxial and biaxial stress can be decomposed into a tensor for the mean pressure (all diagonal components have the same value) and a zero-trace stress tensor.

Quasi-hydrostatic stress: The term may refer to qualitatively different conditions, *e.g.* a homogeneous deviatoric stress, an inhomogeneous stress distribution (stress gradients across a sample), or the presence of microscopic stresses (for instance at grain boundaries) being superimposed on some predominant spatially and/or orientationally averaged pressure. The term may also refer to a transient state of deviatoric or inhomogeneous stress. A common situation is that the meaning of 'quasi-hydrostatic' stress or pressure is not or cannot be specified qualitatively and quantitatively.

Appendix 2. R-line spectroscopy light

This appendix is a technical note. It describes a simple portable setup for microscopic ruby luminescence measurements in routine DAC studies.

A typical optical system for ruby luminescence measurement is sketched in Figure A2: the microscope bench consists of a $10\times$ or $20\times$ objective with long working distance and ∞ tube length, a matching achromatic tube lens of about 200 mm focal length, a colour CCD camera (preferably with extended sensitivity in the red) for viewing the front- or back-illuminated sample and for locating the ruby via its luminescence under laser illumination, a non-stabilized frequency-doubled Nd:YAG laser delivering >20 mW at 532 nm (corresponds to about 10 mW entering the sample volume of a DAC), a dichroic beam splitter, and a few mechanical components. The bench is then fiber-coupled to an optical spectrometer, or as shown in Figure A2, the spectrometer is
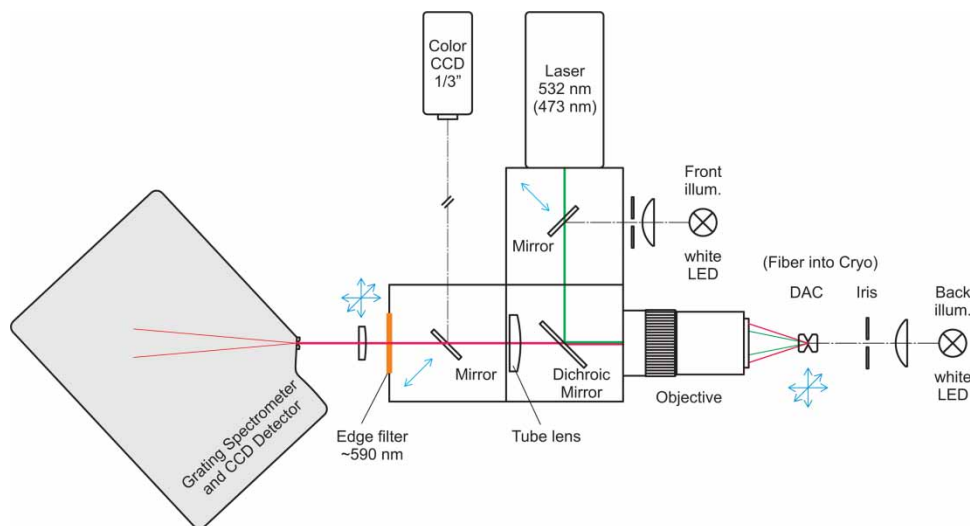
Figure A2. A typical optical bench of a portable ruby luminescence system for pressure measurement. The main components are a 10× or 20× objective with long working distance, a solid state laser, a red-sensitive CCD camera, and a small-size grating spectrometer with specifications suitable for ruby line shift measurements. The spectrometer is either directly attached to the bench as shown or it is fiber-coupled. For measurements in a cryostat not equipped with optical windows, a fiber entrance is placed at the indicated DAC position and the fiber is fed into the cryostat via a vacuum feedthrough.

placed directly at the exit port of the bench. Compared with fiber coupling, the latter mode is preferable if one prefers to minimize the intensity losses.

Of considerable practical value in DAC experiments is the use of annealed ruby spheres of several microns in diameter as described by Chervin et al. [161]. The annealing temperature is in the range of 1200 to 1500°C; this is where tests show internal strain to be released in ordinary ruby powder of 1–5 μm particle size. When ruby balls of 5–10 μm size are illuminated with a focused green laser of about 1–10 mW power, the red luminescence of the micron-size spheres can be seen by eye in microscopic observations and the intensity locally saturates a red-sensitive CCD viewing camera mounted as shown in Figure A2. This means that the high-level sensitivity of a cooled 2D CCD detector is not really needed for measuring R-line spectra at $P < 50$ GPa if the experiment goes well.

A compact plug-and-play-type spectrometer module (Ocean Optics model HR 2000, nominally $f/4$, 101 mm focal length, USB-driven) has proved suitable for routine studies using the DAC. It comes with an uncooled one-dimensional CCD detector of 2048 pixels. The fixed setting of a properly blazed 1800 lines/mm grating is adjusted to cover the spectral range of interest for ruby luminescence under pressure and simultaneously that of Sm-based optical pressure sensors emitting in the deep red. The wavelength dispersion is ∼0.053 nm per CCD pixel and the nominal optical resolution is 0.065 nm for the smallest entrance slit of 5 μm. Hence, despite the rather small focal length, the spectrometer module is suitable to resolve pressure changes of about 0.05 GPa, as can be judged from Figure A3. An application at relatively low pressures up to ∼4 GPa is reported in [310]. Using an entrance slit of 25 μm to enhance the throughput is a possibility; the lower resolution would hardly affect the determination of R-line *shifts* at 300 K, as can be inferred from the simulated broadening in Figure A3. On the other hand, increasing the slit width is not a good idea for experiments at low temperature because the R-lines narrow upon cooling (cf. Figure 12). For low temperature applications, one would choose an alternative CCD linear sensor having smaller pixel size, *i.e.* more pixels per unit of length. This simply puts more pixels into an
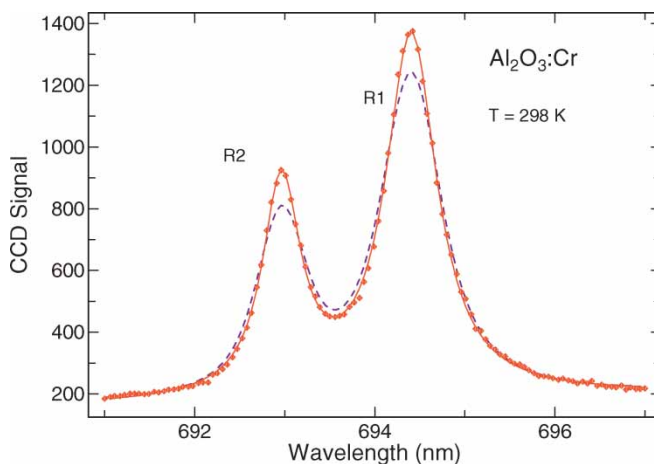
Figure A3.   A ruby luminescence spectrum measured with a mini-spectrometer like the one mentioned in the text. The pixel separation corresponds to a wavelength interval of ∼0.055 nm. About 12 pixels fall into the FWHM of the ruby R1 line at 298 K (∼0.7 nm). The spectrum was measured using an entrance slit of 5 μm width corresponding to a nominal optical resolution of 0.065 nm. The dashed line simulates the line broadening if the slit width is increased to 25 μm.

emission line of interest, but does not offer any advantages with respect to sensitivity and signal to noise.

With some modifications (cylindrical lens in front of the CCD sensor, blue laser excitation), the R-line sensitivity of a compact spectrometer like that described above could be improved. The needs of 'near-megabar research' can perhaps be matched by a similar system equipped with a 2D CCD detector; such systems have become available recently. In general, a drawback of compact spectrometers in R-line measurements is that, depending on coupling optics, the throughput may be limited because the desired spectral resolution is squeezed out of entrance slit settings.

Appendix 3. Ruby luminescence method in the published literature

This Appendix is coauthored by Marx (MPI/FKF Stuttgart). The intention here is to generate an overall picture of the impact of the ruby luminescence method by following the time evolution of the citations of six key publications that appeared before 1990 (Figure A4). In brief, the procedure is as follows.

- We pick four pioneering reports (group I) by scientists at the former National Bureau of Standards (NBS, now NIST) on the ruby luminescence method, its application in probing stress conditions inside a DAC, and its original calibration [9–12]. Two papers (group II) from the Geophysical Laboratory (GL) on the calibration at higher pressures [14,15] are added to the seed of the search.
- It is assumed that at least one or several of these six publications is cited in the follow-up publications addressing or using the ruby luminescence method, *if* that method is referred to by a *formal citation*.
- What escapes from a citation-based search are 'non-citing' publications that refer to the ruby luminescence method but do not include a citation. Scattered observations of preprints indicate that by now the number of non-citing publications is quite sizeable in comparison to that of the citing ones. The 'non-citers' are expected to increase with time because the method acquires the status of a standard procedure.
- The citation search was performed in the Web of Science. The date of search is March 2008.
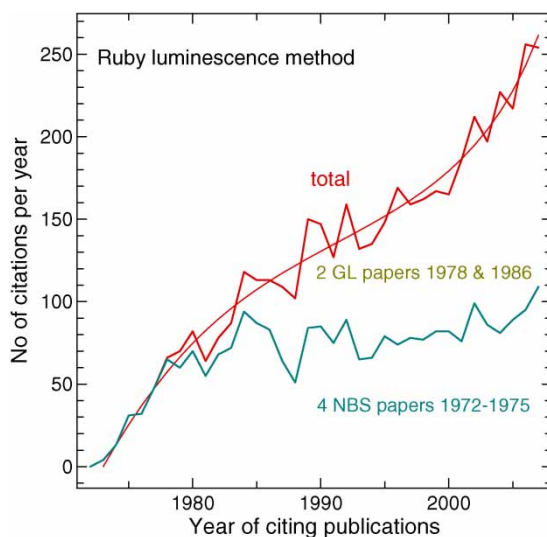
Figure A4.   Citation history of the four pioneering NBS reports on the ruby luminescence method, its application in probing stress conditions inside a DAC, and its calibration [9–12] and two papers from the Geophysical Laboratory (GL) on the calibration at higher pressures [14,15]. Shown is the number of citing papers per year as a function of their publication year. The numbers include formal citations only.

The main observations are as follows.

- Altogether, the six papers have attracted about 4500 citations, $340 + 703 + 464 + 982 = 2489$ for group I and $1165 + 900 = 2065$ for group II.
- Since about 1980, the original work performed at the NBS (group-I) keeps a constant citation level. So, appropriate credit still goes to those who invented the method and demonstrated its practical usefulness.
- By now, the group II papers collected almost as many citations as group I. This can in part be attributed to the increasing number of DAC experiments performed at pressures higher than 50 GPa where the calibrations reported in the group II papers become relevant.
- The number of co-citations of a paper from group I (the method as such and initial calibration) and a paper from group II (extended calibration range) is only about 320.
- Summing over all citations per year, the trend is positive and perhaps even accelerating after the year 2000. An expanded analysis of the published literature shows that the positive trend applies to high-pressure research in general. Also, it is stronger compared with the growth rate of scientific publications in general.